

December 1<sup>st</sup>, 2015

This page intentionally left blank

# 1 Table of Contents

<b>EXECUTIVE SUMMARY .....</b>	<b>1</b>
<b>2 PHYSICS MOTIVATION FOR THE ITPC UPGRADE.....</b>	<b>3</b>
2.1 KEY MEASUREMENTS I: KURTOSIS .....	4
2.2 KEY MEASUREMENTS II: DI-ELECTRON INVARIANT MASS SPECTRA .....	9
2.3 KEY MEASUREMENTS III: STUDY OF THE QCD PHASE DIAGRAM.....	19
2.3.1 <i>iTPC-based improvements in measurement of baryon directed flow .....</i>	<i>20</i>
2.3.2 <i>iTPC-based study of the softening of the Equation of State .....</i>	<i>23</i>
2.3.3 <i>iTPC-based improvements in establishing the onset of the QGP .....</i>	<i>24</i>
2.3.4 <i>iTPC improvements in determining spectra and freeze-out parameters (<math>T</math> and <math>\mu_B</math>) .....</i>	<i>28</i>
2.3.5 <i>Improvements in the physics reach of the internal fixed-target program .....</i>	<i>29</i>
2.4 PHYSICS SUMMARY .....	33
2.5 REFERENCES.....	34
<b>3 INTRODUCTION TO THE STAR TPC - HARDWARE.....</b>	<b>36</b>
3.1 THE PROPOSED UPGRADE.....	36
3.2 TPC DESIGN AND CONFIGURATION .....	37
3.3 ADDITIONAL PERFORMANCE ISSUES .....	40
3.3.1 <i>Distortions .....</i>	<i>40</i>
3.3.2 <i>Aging: an issue for the TPC in the high luminosity era at RHIC.....</i>	<i>42</i>
3.4 REFERENCES.....	42
<b>4 SIMULATIONS WITH A NEW PAD PLANE &amp; MWPCS .....</b>	<b>43</b>
4.1 PADPLANE DESIGN STUDY.....	43
4.2 CONCLUSIONS .....	48
4.3 REFERENCES.....	48
<b>5 PADPLANE AND MWPC DESIGN .....</b>	<b>49</b>
5.1 INTRODUCTION.....	49
5.2 PADPLANE AND MWPC DESIGN FEATURES.....	51
5.2.1 <i>Pad Size and Wire Spacing.....</i>	<i>51</i>
5.2.2 <i>Reduced Voltage on the Inner Anode Wires .....</i>	<i>56</i>
5.2.3 <i>Pad Plane Geometry &amp; Wires: Old compared to New .....</i>	<i>57</i>
5.2.4 <i>Modifications to the Gated Grid .....</i>	<i>58</i>
5.3 REFERENCES.....	61
<b>6 PADPLANE DESIGN AND PROTOTYPE CONSTRUCTION.....</b>	<b>62</b>
<b>7 STRONGBACK ENGINEERING AND CONSTRUCTION .....</b>	<b>66</b>
7.1 OVERVIEW .....	66
7.2 STRONGBACK .....	67
7.3 CHANGES TO THE STRONGBACK .....	68
7.4 QUALITY CONTROL .....	70
7.5 THE RADIATION LENGTH BUDGET FOR THE ITPC STRONGBACK .....	74
<b>8 MWPC ENGINEERING AND CONSTRUCTION .....</b>	<b>76</b>
8.1 GRANITE TABLES & COMBS TO ALIGN THE WIRES .....	76
8.2 A SMALL FACTORY WILL BE REQUIRED .....	78
<b>9 FACILITIES AT SHANDONG UNIVERSITY .....</b>	<b>80</b>
9.1 PROTOTYPING CAPABILITIES.....	81

9.1.1	Test system .....	82
9.2	MWPC PRODUCTION CAPABILITIES .....	85
9.2.1	Progress on a full size prototype at SDU (since late 2014): .....	87
9.3	QA PLAN AND TRAVELERS.....	93
9.4	REFERENCES.....	93
<b>10</b>	<b>ELECTRONICS AND DATA ACQUISITION FOR THE ITPC .....</b>	<b>94</b>
10.1	PREAMPLIFIER AND DIGITIZER ASIC -- “SAMPA” .....	94
10.2	FRONT-END ELECTRONICS CARDS (“IFEE”) .....	96
10.3	READOUT BOARDS (“IRDO”) .....	97
10.3.1	Ancillary Connections & Components .....	98
10.4	POWER DISTRIBUTION AND POWER SUPPLIES .....	99
10.5	DAQ BACKEND.....	99
<b>11</b>	<b>SECTOR INSERTION TOOL .....</b>	<b>101</b>
<b>12</b>	<b>PARTICIPATING INSTITUTIONS .....</b>	<b>107</b>



## FIGURES

- FIGURE 1: RAPIDITY WIDTH DEPENDENCE OF THE NET-PROTON VARIANCE  $\sigma^2$ . THE DATA ARE FOR CENTRAL (5%) Au+Au COLLISIONS AT 7.7 GeV (CIRCLES) AND 19.6 GeV (TRIANGLES). ..... 4
- FIGURE 2: THE OBSERVED NET-PROTON KURTOSIS ( $\kappa\sigma^2$ ) AS A FUNCTION OF RAPIDITY WINDOW FROM BES I (YELLOW TRIANGLES). THESE PRELIMINARY DATA ARE FOR CENTRAL (5%) Au+Au COLLISIONS AT 7.7 GeV (LEFT PANEL) AND 19.6 GeV (RIGHT PANEL). THE GREEN BARS ARE THE ESTIMATED STATISTICAL UNCERTAINTIES WITH THE ITPC FOR BES-II, FOR 7.7 GeV AND 19.6 GeV. IN THE EXTENDED REGION COVERED BY THE ITPC UPGRADE ( $1.0 < |\Delta y| < 1.6$ ), THE ERROR BARS WERE ESTIMATED ASSUMING THAT THE VARIANCES INCREASE LINEARLY WITH RAPIDITY WIDTH. THE LOCATIONS OF THE PROJECTED ERROR BARS ILLUSTRATE ONE POSSIBLE RAPIDITY-WINDOW DEPENDENCE OF THE NET-PROTON KURTOSIS SIGNAL. ALSO SHOWN ARE AMPT SIMULATIONS WITH STRING MELTING AND WITHOUT A CRITICAL POINT (DASHED LINES). ..... 6
- FIGURE 3: STAR RESULTS FOR BEAM ENERGY DEPENDENCE OF  $\kappa\sigma^2$  (TOP PANELS) AND  $S\sigma/S_{\text{KELLAM}}$  (LOWER PANELS) FOR NET PROTONS [18] IN Au+Au COLLISIONS. THE LEFT PANELS ILLUSTRATE THE EFFECT OF  $P_T$  SELECTIONS WHILE THE RIGHT PANELS INDICATE THE EFFECTS OF RAPIDITY SELECTIONS. DOTTED HORIZONTAL LINES ARE EXPECTATIONS FROM POISSON DISTRIBUTIONS. .... 7
- FIGURE 4: THE PLOT SHOWS THE EFFECTS OF  $P_T$  SELECTIONS ON THE  $\kappa\sigma^2$  SIGNAL AND THE PROJECTED ERRORS FOR BESII. .... 8
- FIGURE 5: DIELECTRON INVARIANT MASS SPECTRUM IN THE STAR ACCEPTANCE ( $|\eta_{ee}| < 1$ ,  $0.2 < p_T < 3$  GeV/c,  $|\eta| < 1$ ) AFTER EFFICIENCY CORRECTIONS, COMPARED WITH THE HADRONIC COCKTAIL CONSISTING OF THE DECAYS OF LIGHT HADRONS AND CORRELATED DECAYS OF CHARM IN Au+Au COLLISIONS AT  $\sqrt{s_{NN}} = 19.6$  GeV. THEORETICAL CALCULATIONS OF A BROADENED  $\rho$  SPECTRAL FUNCTION ARE SHOWN UP TO  $1.5$  GeV/ $c^2$  FOR COMPARISON. SYSTEMATIC UNCERTAINTIES FOR THE DATA POINTS ARE SHOWN AS GREEN BOXES, AND THE GREY BAND REPRESENTS THE UNCERTAINTIES FOR THE COCKTAIL SIMULATION. .... 11
- FIGURE 6: THE EXPECTED DIELECTRON EXCESS INVARIANT MASS SPECTRA IN Au+Au COLLISIONS AT  $\sqrt{s_{NN}} = 19.6$  GeV IN BES-II WITH AND WITHOUT ITPC. COMPARISONS TO PHSD AND RAPP'S MODEL CALCULATIONS ARE ALSO SHOWN. THE BARS AND BOXES REPRESENT THE STATISTICAL AND SYSTEMATIC UNCERTAINTIES, RESPECTIVELY. .... 11
- FIGURE 7: THE BEAM ENERGY DEPENDENCE FOR THE LOW-MASS DIELECTRON EXCESS FROM PUBLISHED DATA AT 19.6 AND 200 GeV, MODEL EXPECTATION FROM PHSD FOR ENERGY BELOW 20 GeV AND RAPP'S MODEL ABOVE 20 GeV. ALSO SHOWN ARE PROJECTED SYS. AND STAT. ERRORS FROM PRELIMINARY RESULTS AT 27, 39 AND 62.4 GeV, AND PROJECTIONS FOR BES-II WITH THE ITPC. PROJECTIONS WITHOUT THE ITPC FOR THESE ENERGIES WOULD HAVE  $\times 2$  ( $\sqrt{2}$ ) BIGGER SYS. (STAT.) ERRORS. .... 12
- FIGURE 8: PRELIMINARY STAR MEASUREMENTS OF DIELECTRON INVARIANT MASS DISTRIBUTIONS BELOW  $1.1$  GeV/ $c^2$  FOR  $\sqrt{s_{NN}} = 19.6, 27, 39$  AND  $62.4$  GeV. THE GREY COCKTAIL CURVE INCLUDES ALL KNOWN HADRONIC SOURCES APART FROM THE  $\rho$  (WHICH IS INCLUDED IN THE MODEL). THE ORANGE BAND INCLUDES A MODEL CALCULATION [29] WITH CONTRIBUTIONS FROM BOTH HADRON GAS AND QGP PHASES. .... 13
- FIGURE 9: TOTAL BARYON DENSITY, REPRESENTED BY  $(P+\text{ANTI-}P)/(\pi^++\pi^-)$ , VS. BEAM ENERGY AT RHIC. .... 14
- FIGURE 10: INTEGRATED YIELDS OF THE NORMALIZED DILEPTON EXCESSES FOR  $0.4 < M_{\ell\ell} < 0.75$  GeV/ $c^2$  AS A FUNCTION OF  $dN_{ch}/dY$ . THE SOLID CIRCLE AND DIAMOND REPRESENT THE RESULTS IN 0-80% Au+Au COLLISIONS AT  $\sqrt{s_{NN}} = 19.6$  AND 200 GeV, RESPECTIVELY. THE SQUARES ARE THE RESULTS FOR 40-80%, 10-40%, AND 0-10% Au+Au AT  $\sqrt{s_{NN}} = 200$  GeV. THE OPEN CIRCLE REPRESENTS THE DIMUON RESULT FROM THE NA60 MEASUREMENT WITH  $dN_{ch}/dY > 30$ . BARS ARE STATISTICAL UNCERTAINTIES, AND SYSTEMATIC UNCERTAINTIES ARE SHOWN AS GREY BOXES. THE THEORETICAL LIFETIMES FOR  $\sqrt{s_{NN}} = 200$  GeV Au+Au AS A FUNCTION OF  $dN_{ch}/dY$  IN THE MODEL CALCULATIONS [37] ARE SHOWN AS A DASHED CURVE. THE LIFETIMES FOR  $\sqrt{s_{NN}} = 17.3$  GeV In+In AND  $\sqrt{s_{NN}} = 19.6$  GeV Au+Au IN THE SAME MODEL CALCULATIONS [37] ARE SHOWN AS THE TWO HORIZONTAL BARS. THE  $dN_{ch}/dY$  VALUES FOR THE HORIZONTAL BARS ARE SHIFTED FOR CLARITY. .... 14
- FIGURE 11:  $dE/dx$  OF ELECTRONS AND HADRON BACKGROUND, AS A FUNCTION OF  $N_{\Sigma_e}$ , FOR  $0.4 < p_T < 0.5$  GeV/c. THE BLUE GAUSSIAN CURVE IS THE ELECTRON  $dE/dx$  WHILE THE RED DASHED LINE IS A FIT TO THE MEASURED HADRON  $dE/dx$  TAIL. THE SOLID RED LINE IS THE EXPECTED HADRON CONTAMINATION WITH THE IMPROVED TRACKING OF THE ITPC. .... 16
- FIGURE 12: THESE PANELS DEMONSTRATE THE ITPC IMPROVEMENT FOR 12 DIFFERENT  $P_T$  INTERVALS, FOLLOWING THE SAME SCHEME AS PLOTTED IN THE PREVIOUS FIGURE. .... 16

FIGURE 13: THE EXPECTED PURITY FOR ELECTRONS AS A FUNCTION OF TRANSVERSE MOMENTUM. THE BLACK SYMBOLS SHOW THE PURITY USING THE CURRENT TPC. THE IMPROVED PURITY WITH THE ITPC IS SHOWN IN RED SYMBOLS. ....	17
FIGURE 14: THE ELECTRON ACCEPTANCE USING THE CURRENT TPC (DASHED RED LINE) AND THE EXPECTED IMPROVEMENT USING THE ITPC UNDER TWO DIFFERENT ASSUMPTIONS (RED AND BLUE LINES). ....	17
FIGURE 15: THE ACCEPTANCE DIFFERENCE FACTOR, THE RATIO OF THE MIXED-EVENT UNLIKE-SIGN TO THE MIXED-EVENT LIKE-SIGN ELECTRON PAIR INVARIANT MASS DISTRIBUTIONS WITH THE ITPC UPGRADE. ....	18
FIGURE 16: A SCHEMATIC VERSION OF THE QCD PHASE DIAGRAM. OVERLAID ARE CONCEPTUAL ILLUSTRATIONS OF REACTION TRAJECTORIES FOR CENTRAL COLLISIONS. ....	19
FIGURE 17: <b>LEFT:</b> DIRECTED FLOW PREDICTION IN UNITS OF $\text{GeV}/c$ AS A FUNCTION OF BEAM ENERGY, BASED ON A THREE-FLUID HYDRODYNAMIC MODEL [3] WHOSE EOS INCORPORATES A FIRST-ORDER PHASE TRANSITION. <b>RIGHT:</b> PANEL A) SHOWS THE SLOPE OF DIRECTED FLOW VS. BEAM ENERGY FOR PROTONS FROM Au+Au COLLISIONS AT INTERMEDIATE CENTRALITY. PANEL B) PRESENTS THE SAME FOR NET PROTONS. THE PREDICTION OF THE UrQMD TRANSPORT MODEL [6] IS ALSO PLOTTED IN PANELS A) AND B). ....	20
FIGURE 18: <b>LEFT:</b> PLOTTED POINTS SHOW MEASURED DIRECTED FLOW $v_1(\eta)$ FOR PROTONS IN THREE CENTRALITY BINS FOR Au+Au COLLISIONS AT $\sqrt{s_{NN}} = 7.7 \text{ GeV}$ . THE SOLID CURVES ARE A CUBIC FIT TO THE MEASURED DATA POINTS FOR INTERMEDIATE AND PERIPHERAL CENTRALITIES WHILE THE DASHED LINES ARE LINEAR FITS. THESE FITS ARE EXTRAPOLATED INTO THE RAPIDITY REGION THAT WILL BECOME ACCESSIBLE AFTER THE ITPC UPGRADE. FOR SIMPLICITY, ONLY POSITIVE RAPIDITIES ARE PLOTTED HERE. <b>RIGHT:</b> THE IMPROVEMENT IN STATISTICAL ERRORS THAT WOULD BE ACHIEVED WITH THE ITPC UPGRADE, FOR DIRECTED FLOW MEASUREMENTS AT LOW RHIC ENERGIES AS A FUNCTION OF RAPIDITY, FOR ANY FIXED NUMBER OF EVENTS, BASED ON SIMULATIONS USING THE UrQMD MODEL. POSITIVE AND NEGATIVE RAPIDITIES GIVE THE SAME RESULT, AND ARE AVERAGED IN THIS PLOT. THE TWO HIGH RAPIDITY POINTS WHERE A ZERO RATIO IS PLOTTED CORRESPOND TO ACCEPTANCE REGIONS WHERE THE PRESENT TPC PROVIDES NO DATA WHATSOEVER. ....	22
FIGURE 19: THE FORWARD $v_1$ MEASUREMENT AS A FUNCTION OF CENTRALITY EXPLICITLY SHOWING THE IMPROVEMENTS DUE TO THE COVERAGE OF THE ITPC. ....	23
FIGURE 20: THE WIDTH OF PION RAPIDITY DISTRIBUTIONS [11], NORMALIZED TO CALCULATIONS BASED ON LANDAU'S HYDRODYNAMIC MODEL [9] AS A FUNCTION OF BEAM ENERGY. THE MINIMUM MAY BE AN INDICATION OF THE SOFTENING OF THE EOS [10,11]. THE ONLY AVAILABLE RHIC MEASUREMENT TO DATE IS AT $\sqrt{s_{NN}} = 200 \text{ GeV}$ , FROM BRAHMS [12]. ....	24
FIGURE 21: THE DIFFERENCE IN $v_2$ BETWEEN PARTICLES AND THEIR ANTIPARTICLES (SEE LEGEND) AS A FUNCTION OF $\sqrt{s_{NN}}$ FOR 0-80% CENTRAL Au+Au COLLISIONS. THE DASHED LINES ARE FITS WITH A POWER-LAW FUNCTION. THE ERROR BARS DEPICT THE COMBINED STATISTICAL AND SYSTEMATIC ERRORS. ....	25
FIGURE 22: THE UPPER PANELS DEPICT THE ELLIPTIC FLOW, $v_2$ , AS A FUNCTION OF REDUCED TRANSVERSE MASS, $M_T - M_0$ , FOR PARTICLES (PANELS A AND B), AND FOR ANTIPARTICLES (PANELS C AND D), IN 0-80% CENTRAL Au+Au COLLISIONS AT $\sqrt{s_{NN}} = 11.5$ AND $62.4 \text{ GeV}$ . SIMULTANEOUS FITS TO MESONS OTHER THAN PIONS ARE SHOWN AS DASHED LINES. THE DIFFERENCE BETWEEN THE BARYON $v_2$ AND THE MESON FITS ARE SHOWN IN THE LOWER PANELS. ....	26
FIGURE 23: SIMULATED EVENT PLANE RESOLUTIONS AS A FUNCTION OF CENTRALITY FOR Au+Au COLLISIONS AT $19.6 \text{ GeV}$ ( $\eta$ -SUB METHOD). A FACTOR OF $\sim 2$ IMPROVEMENT IS OBSERVED IN $1 <  \eta  < 2$ BY USING THE ITPC. ....	27
FIGURE 24: SCALED $v_2$ OF THE PHI MESON SHOWING THE PROJECTED ERROR BARS FOR BESII WITH THE CURRENT TPC (BLUE BAND) AND WITH THE ITPC (RED BAND). ....	27
FIGURE 25: THE TOP PANEL SHOWS A SCHEMATIC DRAWING OF STAR SHOWING THE LOCATION OF THE FIXED TARGET AND ITS $\eta$ COVERAGE. THE BOTTOM PANEL SHOWS A DISTRIBUTION OF RECONSTRUCTED VERTICES WITH $V_z \sim 211 \text{ cm}$ (BOTTOM LEFT) AND A SCHEMATIC OF TARGET AS INSTALLED IN THE VACCUUM PIPE (BOTTOM RIGHT). THE SHAPE OF THE GOLD TARGET IS CLEARLY EVIDENT IN THE DISTRIBUTION OF RECONSTRUCTED VERTICES. ....	31
FIGURE 26: THE ACCEPTANCE FOR PIONS (TOP) AND PROTONS (BOTTOM) IN FIXED-TARGET MODE. THE HISTOGRAM IS FILLED WITH DATA FROM Au+Al BACKGROUND EVENTS TAKEN DURING BES-I. THE ALTERNATING RED AND CYAN VERTICAL BARS INDICATE THE CENTER-OF-MASS RAPIDITY FOR VARIOUS ENERGIES TO BE STUDIED. THE CYAN AND RED CURVES INDICATE THE LOWER ACCEPTANCE CUT-INS FOR THE CURRENT TPC AND ITPC CONFIGURATIONS, RESPECTIVELY. ....	32
FIGURE 27: A SCHEMATIC VIEW OF THE STAR TPC. SECONDARY ELECTRONS DRIFT AWAY FROM THE HIGH VOLTAGE MEMBRANE, AT THE CENTER, TOWARDS READOUT PLANES AT EITHER END OF THE TPC. ....	38
FIGURE 28: CONFIGURATION OF THE EXISTING PAD ROWS IN A STAR TPC PADPLANE SUPER-SECTOR (ONE INNER SECTOR AND ONE OUTER SECTOR). NOTE THAT THE OUTER SECTOR PADPLANE COVERAGE IS COMPLETE BUT THE INNER SECTOR PAD ROWS DO NOT COVER THE FULL AREA OF THE INNER SECTOR. ....	39

FIGURE 29: DISTORTIONS AT THE JUNCTION BETWEEN THE INNER AND OUTER GATED GRIDS. THE VERTICAL AXIS (CM) SHOWS THE POSITION OF A PAD ROW (INDICATED BY DOTS) IN THE RADIAL DIRECTION. THE HORIZONTAL AXIS IS IN MILLIMETERS. THE BLACK DOTS SHOW THE EXPECTED HIT PATTERN FOR AN INFINITE MOMENTUM TRACK. THE RED DOTS SHOW THE OBSERVED HIT PATTERN DUE TO CHARGE LEAKING OUT OF THE GAP BETWEEN THE INNER AND OUTER GATED GRIDS. ....	41
FIGURE 30: SCHEMATIC VIEW OF THE TPC RESPONSE SIMULATOR FLOW CHART. ....	43
FIGURE 31: CHARACTERISTICS OF THE RECONSTRUCTED EVENTS SIMULATED WITH THE NEW iTPC GEOMETRY. ....	45
FIGURE 32: MOMENTUM RESOLUTION AS A FUNCTION OF THE TRANSVERSE MOMENTUM TO EXTRACT THE $p_T$ VALUE. ....	46
FIGURE 33: TRACK RESOLUTION (LINEAR COMPONENT) FOR DIFFERENT GEOMETRIES OF THE INNER PART OF THE TIME PROJECTION CHAMBER. ....	46
FIGURE 34: EFFICIENCY OF PION, KAON, AND PROTON MEASUREMENTS AS A FUNCTION OF PSEUDORAPIDITY AND TRANSVERSE MOMENTUM (IN GeV/c) FOR THE CURRENT TPC DESIGN (BLUE) AND FOR THE devTC DESIGN (RED). THE THEORETICAL CURVE FOR THE EFFICIENCY FOR TRACKS LONGER THAN 30 CM IS SHOWN AS A GREEN DASHED LINE. ....	47
FIGURE 35: $dE/dx$ RESOLUTION COMPARISON FOR THE EXISTING AND UPGRADED iTPC FOR TWO PSEUDORAPIDITY REGIONS. ....	48
FIGURE 36: THE STAR TPC DURING CONSTRUCTION AT LBL. THE TRACKING VOLUME OF THE TPC IS 4 METERS IN DIAMETER AND 4.2 METERS LONG. THE PHOTO SHOWS HOW EACH END OF THE TPC IS DIVIDED INTO 12 SUPER-SECTORS AND EACH SUPER-SECTOR IS DIVIDED INTO AN INNER AND AN OUTER READOUT SECTOR. ....	49
FIGURE 37: A PHOTO OF AN OUTER SECTOR PADPLANE SHOWING THE MWPC, THE PADPLANE, AND THE ALUMINUM STRONGBACK THAT SUPPORTS THE PADPLANE AND WIRE GRIDS. THE MWPCS ARE REALLY THREE GRIDS OF WIRES; THE GATED GRID (TOP), THE GROUND GRID (MIDDLE, ALSO KNOWN AS THE CATHODE GRID), AND THE ANODE WIRES (BOTTOM). ....	51
FIGURE 38: SIDE VIEW OF AN INNER SECTOR ADPLANE, STRONGBACK AND WIRE GRIDS. DIMENSIONS ARE IN MM. ....	52
FIGURE 39: THE PAD RESPONSE FUNCTION FOR THE OUTER SECTOR IS SHOWN BY THE BLACK LINE, THE EXISTING INNER SECTOR BY THE BLUE LINE, AND THE PROPOSED INNER SECTOR BY THE RED LINE. THE PAD SPACING IS 6.7 MM, 3.35 MM, AND 5 MM RESPECTIVELY. THE PADPLANE TO ANODE WIRE PLANE DISTANCE IS 4 MM IN THE OUTER SECTOR AND 2 MM IN THE INNER SECTOR. THE GREEN LINE SHOWS THE PRF FOR A VERY WIDE PAD, 20 MM, AND IT SUGGESTS THAT 50% OF THE SIGNAL GOES TO THE PADPLANE IN THE ASYMPTOTIC LIMIT. THE DIFFUSION WIDTH FOR AN ELECTRON THAT DRIFTS THE FULL LENGTH OF THE TPC WOULD BE A CURVE THAT LIES VERY CLOSE TO THE BLACK LINE. ....	53
FIGURE 40: SIMULATIONS OF THE EFFECTIVE PAD RESPONSE FUNCTION FOR PADS ON THE INNER AND OUTER TPC PADPLANES. THE INNER PADS WERE ASSUMED TO BE 3.35 MM WIDE AND THE OUTER PADS 6.7 MM WIDE. THE CIRCLES SHOW THE 3-SIGMA LIMIT FOR THE PAD RESPONSE FUNCTION CONVOLUTED WITH THE DIFFUSION LIMIT FOR PARTICLES THAT DRIFT THE FULL DISTANCE FROM THE CM TO THE PADPLANE. P10 GAS IS ASSUMED. THE DIFFERENT CIRCLES SHOW THE DIFFERENT RESPONSE THAT IS RECORDED WHEN THE B FIELD IS SET TO 0.0, 0.25 T, OR 0.5 T. [4] ....	54
FIGURE 41: THE ORIGINAL STAR PAD PLANE GEOMETRY (SIDE VIEW). THE OUTER SECTOR PAD ROWS COVERED THE ENTIRE PAD PLANE BUT THE INNER SECTOR PAD ROWS WERE WIDELY SPACED ( $> 5$ CM). ....	57
FIGURE 42: THE NEW STAR PAD PLANE GEOMETRY. THE OUTER SECTOR CONFIGURATION REMAINS THE SAME, BUT THE INNER SECTOR HAS MORE PAD ROWS AND THERE AREN'T ANY GAPS BETWEEN THE PAD ROWS. ....	57
FIGURE 43: A DETAILED VIEW OF THE GAP BETWEEN THE INNER AND OUTER SECTORS. NOTE THAT THERE IS A 12 MM GAP BETWEEN THE END OF THE GATED GRID IN THE INNER SECTOR AND THE START OF THE GATED GRID IN THE OUTER SECTOR AND A 16 MM BETWEEN INNER AND OUTER ANODE GRIDS. ALSO, NOTE THAT THE LAST ANODE WIRE IS LARGER IN DIAMETER (125 $\mu$ m) THAN THE REST OF THE ANODE WIRES (20 $\mu$ m). ....	58
FIGURE 44: THREE LOW GAIN WIRES (125 $\mu$ m DIAMETER) WILL BE PLACED ON BOTH ENDS OF THE ANODE WIRE GRID. THE LOW GAIN WIRES WILL REDUCE THE PRODUCTION OF IONS IN THE REGION WHERE THEY CAN LEAK INTO THE DRIFT-VOLUME OF THE TPC. ANOTHER OPTION IS TO GROUND THE LAST WIRE SO THAT THE GAIN IS ZERO ON THAT WIRE. ....	59
FIGURE 45: A TOP VIEW AND A SIDE VIEW OF AN ALICE INNER READOUT CHAMBER (iROC). THE FIGURES SHOW A POTENTIAL SOLUTION TO THE "GRID LEAK" PROBLEM WHICH IS TO TERMINATE THE PLANE OF WIRES WITH A WALL OF G10. THE WALL HAS CU TRACES THAT ARE BIASED APPROPRIATELY TO TERMINATE THE FIELD LINES COMING FROM THE ANODE WIRES AND GATED GRID. ....	59
FIGURE 46: A SIDE VIEW SHOWING HOW A BIASED WALL MIGHT BE IMPLEMENTED AT STAR. THE WALL IS DESIGNED SO IT CAN BE BIASED TO $\sim 500$ VOLTS AND WILL ATTRACT FIELD LINES COMING FROM THE ANODE WIRES. THUS, POSITIVE IONS PRODUCED NEAR THE ANODE WIRES TERMINATE ON THE WALL AND DO NOT LEAK OUT INTO THE GAP BETWEEN THE INNER AND OUTER SECTORS. ....	60

FIGURE 47: GARFIELD SIMULATIONS OF IONS FLOWING AWAY FROM THE STAR TPC ANODE WIRES WHEN THE GATED GRID IS CLOSED. THERE IS A 1.2 CM GAP BETWEEN THE INNER AND OUTER SECTORS THAT IS NOT COVERED BY THE GATED GRIDS. THIS GAP ALLOWS IONS TO FLOW OUT OF THE MWPC REGION AND INTO THE TRACKING VOLUME OF THE TPC. PUTTING A -690 VOLT BIAS (LEFT PANELS) ON THE WALL REDUCES THE FLOW OF IONS, WHILE THE “L” SHAPED WALL (RIGHT PANELS) COMPLETELY STOPS THE FLOW OF IONS. THE “L” SHAPED WALL WAS HELD AT 0 VOLTS IN THIS SIMULATION...	60
FIGURE 48: THE FIRST PADPLANE PROTOTYPE. LEFT, CONNECTOR SIDE. RIGHT, PAD SIDE. ....	62
FIGURE 49: ELECTRONIC NOISE AS FUNCTION OF TRACE LENGTH. THE NOISE IS MEASURED IN ADC COUNTS AND TRACE LENGTH IS IN MM. THE RED LINE REPRESENTS THE MAXIMUM ALLOWABLE NOISE BASED ON THE CURRENT TPC’S ELECTRONICS.	63
FIGURE 50: THE NEW PADPLANE DESIGN FOR THE ITPC. THE BLACK BARS ARE THE LOCATIONS FOR THE IFEE CONNECTORS AND THE COLORED ZONES MAP OUT THE PADS THAT COMMUNICATE WHICH EACH IFEE CARD. THE GREY TRAPEZOID OUTLINES THE DIMENSIONS OF THE ALUMINUM STRONGBACK THAT LIES UNDER THE PADPLANE, WHILE THE RED TRAPEZOID SHOWS THE ORIGINAL PC BOARD DIMENSIONS PRIOR TO TRIMMING TO SIZE AND SHAPE. ....	64
FIGURE 51: THE LOCATION OF FIRST AND LAST PAD ROWS ON THE ITPC PADPLANE. OTHER SIGNIFICANT LANDMARKS ARE INCLUDED IN THE TABLE. ....	64
FIGURE 52: SAMTEC MEC1-80 SERIES CONNECTOR FOR THE PAD-TO-IFEE CONNECTION .....	65
FIGURE 53: THE STAR INNER SECTOR STRONGBACK (24A368D) RENDERED IN CREO ELEMENTS DIRECT (CIRCA 2015) .....	67
FIGURE 54: A PROTOTYPE INNER SECTOR STRONGBACK IS SHOWN DURING FABRICATION AT THE UNIVERSITY OF TEXAS (CIRCA 2013). THE SECTOR WAS MACHINED OUT OF A SINGLE PIECE OF ALUMINUM. DIMENSIONS ARE: ~27 INCHES TALL, ~25 INCHES WIDE AND WEIGHT ~70 LBS. THE SECTOR IS VIEWED FROM THE BACKSIDE. ....	68
FIGURE 55: EXPERTS EXAMINING A SPARE INNER SECTOR FOR THE TPC. NOTE THE OLD STYLE PADPLANE WITH ELECTRONICS CARDS (ABDB BOARDS) MOUNTED ALONG THE EDGE OF THE SECTOR. NORMALLY THE SPARE SECTORS (STAR HAS TWO SPARE SECTORS) ARE SEALED IN A STORAGE BOX AND KEPT UNDER DRY NITROGEN. ....	69
FIGURE 56: THE INNER SECTOR STRONGBACK WILL BE MODIFIED TO INCLUDE A 0.070” DEEP NOTCH ON THE TOP AND BOTTOM ENDS OF THE SECTOR. THE NOTCH WILL BE USED TO MOUNT A WALL BETWEEN THE INNER AND OUTER SECTORS. ....	69
FIGURE 57: LEFT: ORIGINAL QA FLOW CHART TPC MWPC ASSEMBLY.....	71
FIGURE 58: A SAMPLE PAGE FOR ONE OF THE TRANSLATED TRAVELER DOCUMENTS. ....	73
FIGURE 59: RADIATION LENGTH VS. PSEUDORAPIDITY FOR THE ORIGINAL STRONGBACK. ELECTRONICS, CABLES AND COOLING MANIFOLDS ARE NOT INCLUDED IN THESE CALCULATIONS. THE LOWEST POINTS ARE THE CUTOUTS FOR THE ELECTRONICS AND SO THESE NUMBERS ARE NOT REPRESENTATIVE OF THE FINAL ASSEMBLY BECAUSE THIS IS WHERE THE FEE CARDS WILL SIT AND THEIR AVERAGE THICKNESS IS GREATER THAN 7%. ....	74
FIGURE 60: A TYPICAL GRADE A INSPECTION PLATE (OTHERWISE KNOWN AS A GRANITE TABLE). TYPICAL DIMENSIONS ARE 6 FEET BY 4 FEET BY 8 INCHES, ALTHOUGH THE TABLES ARE AVAILABLE IN MANY DIFFERENT SIZES. ....	76
FIGURE 61: TOP VIEW OF A GRANITE TABLE WITH ONE OF THE WIRE ALIGNMENT COMBS EXPOSED. THE SECOND COMB LIES UNDER THE ALUMINUM SHIELD ON THE RIGHT. SCALE: THE YELLOW PORTION OF THE TAPE IS 1 METER LONG. ....	77
FIGURE 62: A WIRE COMB MOUNTED ON THE GRANITE TABLE IN SHOWN IN THE LEFT HAND FIGURE. THE “COMB” IS ACTUALLY COMPOSED OF TWO PIECES; THE COMB AND A STRAIGHT EDGE. THE FIGURE ON THE RIGHT SHOWS A CLOSE-UP PHOTO OF THE COMB. THE STRAIGHT EDGE LIES BEHIND THE COMB AND IS LOCATED ABOUT HALF WAY UP THE TEETH. THE WIRES ARE ALIGNED BY BEING PUSHED INTO THE CORNER DEFINED BY THE INTERSECTION OF THE STRAIGHTEDGE WITH THE VERTICAL SIDES OF THE COMB. ....	78
FIGURE 63: OUTER SECTOR MWPCs UNDER CONSTRUCTION IN BERKELEY (CIRCA 1995). ....	79
FIGURE 64: EXPERIMENTAL HALL WITH TWO GRANITE TABLES (LEFT) AND CLEAN ROOM WITH CRANE AND GRANITE TABLE (RIGHT) FOR MWPC PRODUCTION AT SDU. ....	80
FIGURE 65: THE WIRE WINDING MACHINE AT SDU (LEFT) AND THE OPTICAL SYSTEM FOR MAKING WIRE TENSION MEASUREMENTS (RIGHT). ....	81
FIGURE 66: EXPLODED VIEW AND SETUP FOR THE SMALL SCALE MWPC PROTOTYPE. ....	81
FIGURE 67: THE COSMIC RAY TEST STAND AT SDU AND ASSOCIATED TEST EQUIPMENT. ....	82
FIGURE 68: PAD NUMBERING SCHEME FOR THE SMALL MWPC PROTOTYPE. ....	83
FIGURE 69: THE PEDESTAL MEASURED ON ONE PAD AT 1350 V (LEFT) AND THE SUMMED SIGNAL FROM ALL PADS AFTER PEDESTAL SUBTRACTION (RIGHT). ....	83
FIGURE 70: LAYOUT OF THE MWPC PROTOTYPE TEST SYSTEM. ....	84
FIGURE 71: THE SPE SPECTRUM OF HAMAMATSU R11102-A52468(LEFT) AND R11102-A52723(RIGHT) .....	84
FIGURE 72: THE ANODE OUTPUT CHARGE VERSUS HIGH VOLTAGE SUPPLY OF HAMAMATSU R11102-A52468 (LEFT) AND R11102-A52723 (RIGHT). ....	85

FIGURE 73: (LEFT): THE CONNECTION BETWEEN SMALL PROTOTYPE, FEES AND RDO BOARD. (RIGHT): THE ADC VALUE VERSUS THE TIME BIN NUMBER .....	85
FIGURE 74: A SKETCH OF THE TEMPORARY WIRE TRANSFER FRAME. THE INNER SIZE FOR THE BOX IS 76.2 X 90.0 CM AND THE SIZE OF THE MATERIAL IS 3.0 X 6.0 X 0.3 CM.....	86
FIGURE 75: WIRE WINDING ON THE FIRST TWO WIRE PLANES WITH 20UM W-WIRE. ....	86
FIGURE 76: GLUING ROBOT FOR DISPENSING EPOXY ON THIN EDGES.....	86
FIGURE 77: PADPLANE ON GRANITE TABLE HELD FLAT BY THE SUCTION OF A VACUUM SYSTEM. ....	88
FIGURE 78: THE STRONGBACK WITH THE PAD PLANE GLUED IN PLACE. ....	88
FIGURE 79: GLUING STAND FOR ANODE WIRE MOUNT AND GRANITE TABLE.....	89
FIGURE 80: THE ANODE WIRE MOUNTS WERE GLUED TO THE STRONGBACK WITH EPOXY.....	89
FIGURE 81: ATTACHING SHIELD & GATED WIRE MOUNTS TO STRONGBACK.....	90
FIGURE 82: STRONGBACK WITH ALL THREE SIDE WIRE MOUNTS ATTACHED BEFORE DRILLING/PINNING. ....	90
FIGURE 83: THE DRILL/PINNING FIXTURE DESIGNED AT SDU .....	91
FIGURE 84: DRILLING & PINNING THE SIDE WIRE MOUNTS.....	91
FIGURE 85: ONE SIDE THE WIRE COMBS INSTALLED INCLUDING ANGLE PLATES, STRAIGHT EDGE AND COMBS (LEFT), AND A ZOOMED VIEW FOR THE COMBS AND STRAIGHT EDGE.. ....	92
FIGURE 86: PUTTING THE WIRE FRAME ON THE WIRE COMBS .....	92
FIGURE 87: EPOXYING THE ANODE WIRES ON THE WIRE MOUNTS WITH PROTECTING COVERS IN PLACE. ....	93
FIGURE 88: SAMPA MWP1 "CHIP 1" .....	95
FIGURE 89: SAMPA MWP1 "CHIP 3" .....	95
FIGURE 90: OUTPUT SIGNAL OF THE SAMPA PREAMPLIFIER/SHAPER. THESE ARE PRELIMINARY RESULTS FROM THE MWP1 "CHIP 1" EVALUATION.....	96
FIGURE 91: PRE-PROTOTYPE IFEE (PPFEE) ELECTRONIC CARD SHOWN PLUGGED INTO THE PADPLANE .....	97
FIGURE 92: IRDO PROTOTYPE. ....	98
FIGURE 93: THE ORIGINAL SECTOR-MOUNTING TOOL. THE SECTOR MUST FIT THROUGH THE OPENING IN THE END-WHEEL, ROTATE, AND FINALLY PULL BACK INTO PLACE OVER A PAIR OF ALIGNMENT PINS (TOOLING BALLS) THAT ARE LOCATED INSIDE THE TPC. ....	101
FIGURE 94: SCHEMATIC DIAGRAM OF THE PROPOSED NEW SECTOR-MOUNTING TOOL. THE GREEN WALLS ARE FIXED TO THE MAGNET FACE AND DEFINE THE LIMITS OF MOTION IN THE PLANE PARALLEL TO THE TPC END-WHEEL. THE RED SUPPORT COLUMNS MOVE HORIZONTALLY WITHIN THE GREEN WALLS AND THE LIFT THAT SUPPORTS THE SECTOR MANIPULATION TOOL MOVES VERTICALLY ON RED COLUMNS. ....	102
FIGURE 95: PHOTOGRAPH OF AN EXISTING PLATFORM FROM BASTIAN SOLUTIONS. THE LIFT IN OUR PARTICULAR APPLICATION WILL NOT NEED THE SCISSOR EXTENSION IN THE HORIZONTAL DIRECTION. ....	103
FIGURE 96: CROSS SECTIONAL SCHEMATIC VIEW OF THE PLATFORM TO SHOW HOW THE SECTOR MANIPULATION TOOL SITS ON THE LIFT. ....	104
FIGURE 97: SCHEMATIC VIEWS OF THE SECTOR MANIPULATION TOOL PLACING AN INNER SECTOR ASSEMBLY THROUGH THE OPENING AT THE 12 O'CLOCK POSITION OF THE TPC END-WHEEL. ....	105
FIGURE 98: PHOTOGRAPHS OF THE TPC SECTOR MANIPULATION TOOL USED IN ASSEMBLY OF THE ALICE TPC AT LHC. ....	106

This page intentionally left blank

# Technical Design Report for the iTPC Upgrade

The STAR Collaboration

## Executive Summary

We propose to upgrade the inner sectors of the STAR TPC to increase the segmentation on the inner padplane and to renew the inner sector wire chambers. These two improvements will extend the capabilities of the TPC in many ways. Most significantly, the enhanced tracking at small angles relative to the beamline will expand the TPC's acceptance out to pseudo-rapidity  $|\eta| \leq 1.5$ , compared to the current limitation of  $|\eta| \leq 1$ . Furthermore, the detector will have better acceptance for tracks with low momentum, as well as better resolution in both momentum and  $dE/dx$  for tracks of all momenta. These changes will enable the collection of data that is critical to the physics mission for Phase-II of the Beam Energy Scan (BES-II). In addition, the improved  $dE/dx$  and momentum resolution, as well as tracking at higher pseudorapidity, provide the foundation for another proposed upgrade - the endcap time of flight project (endcap-TOF) by the STAR/CBM collaboration.

The enhanced performance resulting from the iTPC project will be critical for making the measurements needed to fully address the physics questions which form the basis for the BES-II program. We will discuss two topics, here, and leave the full presentation of the physics program to the succeeding chapters: (i) We will use net-proton kurtosis measurements in a search for a critical point in the QCD phase diagram, and (ii) we will use low mass dielectron pairs to explore the modification of vector mesons in connection with the approach to chiral symmetry restoration in a dense medium.

The critical point, if it exists, will provide a landmark in the phase diagram of nuclear matter and guide further experimental and theoretical studies of QCD over a wide range of conditions. The discovery of a QCD critical point would constitute a significant scientific achievement in heavy ion physics. In addition, characterization of how the system approaches chiral symmetry restoration in dense systems will greatly enhance our understanding of QCD in these environments. As detailed in the STAR BES-II White Paper, the QCD Town Meeting Summary Report, and the Hot QCD White Paper, results from Phase-I of the beam energy scan show provocative results calling for further investigation with greater statistics and increased rapidity coverage.

While the increased data sample provided by BES-II will improve upon the quality of current measurements, only the enhanced capabilities provided by the iTPC upgrade will allow a full study of observables which are sensitive to changes in correlation length near the critical point. For example, in the vicinity of a critical point, the net-proton kurtosis is expected to rise as the fourth power of the size of the rapidity window but then saturate as the window becomes comparable to, or larger than, the correlation length in the

system. Existing BES-I data exhibit intriguing energy trends but the measurements suffer from limited statistics and the signal only appears near the edge of the current STAR rapidity acceptance ( $\Delta y$ ). The iTPC improvements will allow the fullest possible coverage of the collision region to establish the existence of a rapid rise in the kurtosis signal and, if found, to more fully map out its properties.

In the area of low mass dielectron measurements, the iTPC upgrade improves the acceptance of the detector but also reduces the hadron contamination which is responsible for and is the dominant source of systematic uncertainties in previous measurements. The reduction in uncertainty made possible by the iTPC project will allow the full exploitation of the increased statistics to be collected during BES-II. Full characterization of any meson broadening, and distinguishing between competing theoretical interpretations for a quantitative assessment of how the system approaches chiral symmetry restoration, will only be possible with these improvements.

The costs for the upgrade project will be shared by the US DOE and the Chinese NSF. The DOE project costs are mainly for the design and fabrication of the new sectors, for the design and fabrication of compatible electronics, and for the design and fabrication of the installation tooling. The in-kind contributions from China will focus on the construction of the MWPCs which will be mated to the sector strongbacks in China. The iTPC project proposes to do conceptual design studies in FY2015, sector and MWPC production in FY2016-FY2018, with final installation in FY2018. Following this schedule, the iTPC would be ready to take data during RHIC Run-19. Current RHIC long-range planning calls for the STAR BES II program to take measurements during Run 19 and Run 20.



## 2 Physics Motivation for the iTPC Upgrade

The goal of the iTPC project is enable a detailed study of the phase diagram of nuclear matter over a wide range of beam energies. The STAR Beam Energy Scan Phase-II (BES-II) Whitepaper [1] presents a summary of the results from the first round of measurements taken between 7.7 and 200 GeV at RHIC. It also presents the rationale for a much more in-depth study of BES physics.

In order to understand the physics in more detail, the community has launched major initiatives in both experiment and theory. In addition to the proposed BES-II experimental program, a topical theory collaboration is being formed, named BEST (Beam Energy Scan Theory), modeled after the successful *Topical Collaboration on Jet and Electromagnetic Tomography (JET) of Extreme Phases of Matter*. It is envisaged that a collaboration of comparable size will engage in a coordinated effort to resolve current challenges in BES-related theory.

The BES Phase-II program is scheduled to run in 2019 and 2020. The BES-II proposal requests high statistics (typically 20 times higher than BES-I), as set out in for the BES-II beam energies currently envisaged. Electron cooling, presently under development at RHIC, along with longer ion bunches, is expected to increase luminosity by a factor of about 3 near 7.7 GeV, increasing to a factor of about 8 at 11.5 GeV and above. It is planned to install e-cooling during a year-long shutdown in 2018, and therefore BES Phase-II will likely begin taking data in 2019.

Beam energy	$\mu_B$ (MeV)	Events (M)
19.6	205	400
14.5	260	300
11.5	315	230
9.1	370	160
7.7	420	100

Table 1: The beam energies and number of events envisaged in the BES-II proposal.

The iTPC upgrade is expected to be ready for physics in 2019, at the same time as the electron cooling.

In this section of the iTPC Technical Design Report (TDR), we present key BES-II physics measurements with emphasis on aspects where the added capabilities of the iTPC are essential for a deeper understanding of the QCD phase diagram. An overview of the technical aspects of the iTPC's enhancements to acceptance, efficiency and particle identification follow in Sections 3, 4 and 5.

## 2.1 Key Measurements I: Kurtosis

Discovery of the QCD critical point would be the most anticipated outcome of the RHIC Beam Energy Scan program. Effective field theories suggest that at large baryon chemical potential ( $\mu_B$ ), QCD matter should exhibit a first-order phase transition [16]. Since the transition at small  $\mu_B$  is known from lattice calculations to be a smooth crossover, if there is a first order phase transition, it must end at a critical point. Theory suggest that the critical point might be signaled by large fluctuations in event-by-event multiplicities of conserved quantities such as net-baryon number, net charge, and net strangeness. These quantities have variances  $\langle(\delta N)^2\rangle$  that are proportional to the correlation length ( $\xi$ ) squared. Higher moments like skewness,  $S \propto \langle(\delta N)^3\rangle$  and kurtosis  $\kappa \propto \langle(\delta N)^4\rangle$  vary more strongly with  $\xi$  and are argued to offer higher sensitivity to critical fluctuations [17].

The STAR Beam Energy Scan I (BES-I) results on particle ratios ( $K/\pi$ ,  $p/\pi$ ,  $K/p$ ) and multiplicity (net-charge and net-proton) fluctuations show constant or monotonic trends versus energy. Net proton variance versus rapidity width is also observed to be linear, as shown in Figure 1.

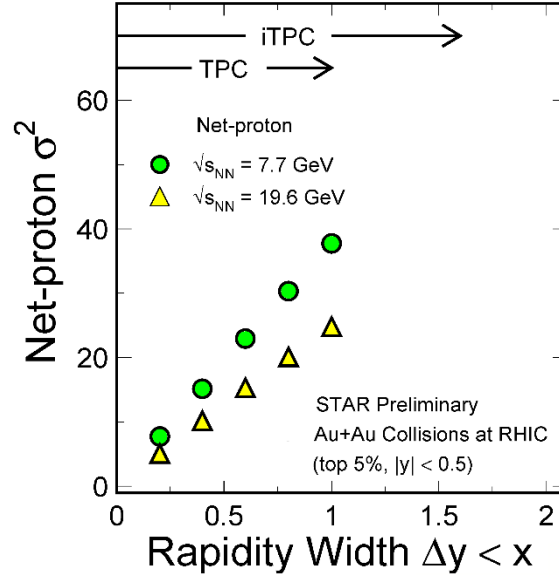


Figure 1: Rapidity width dependence of the net-proton variance  $\sigma^2$ . The data are for central (5%) Au+Au collisions at 7.7 GeV (circles) and 19.6 GeV (triangles).

On the other hand, skewness and kurtosis are argued to be more sensitive to the correlation length than the variance. Skewness and kurtosis are higher moments of fluctuation measurements that are measured as volume-independent production parameters  $S\sigma$  and  $\kappa\sigma^2$  respectively. It is vital that these moments be measured accurately, as well.

In the study of critical phenomena, we are interested in the overall size of the system and the dynamical correlation length related to genuine fluctuations near the critical point.

The range of the correlations  $y_{\text{corr}}$  is the crucial issue for the dependence of a fluctuation signal on the rapidity acceptance window ( $\Delta y$ ). If  $\Delta y$  is smaller than the correlation length ( $y_{\text{corr}}$ ), then the critical point contribution to the  $n$ -th order cumulant of the fluctuations grows as  $(\Delta y)^n$ . When  $\Delta y$  is much larger than  $y_{\text{corr}}$ , all cumulants grow linearly with  $\Delta y$  since uncorrelated contributions are additive in a cumulant.

It is possible to estimate  $y_{\text{corr}}$  in a boost-invariant scenario with a finite correlation length. Consider a comoving coordinate system near freezeout with correlation length  $\xi$ . This translates into a Bjorken rapidity correlation length  $\Delta\eta_{\text{corr}} \approx \xi/\tau$ . Thus,  $\Delta\eta_{\text{corr}}$  is approximately 0.1-0.3 units wide if we assume  $\xi$  ranges from 1 fm to 3 fm near the critical point and a Bjorken freeze-out time  $\tau$  of about 10 fm. However, detectors do not measure the spatial (Bjorken) rapidity  $\eta$  but rather the kinematic rapidity ( $y$ ) of the particles. Within the spatial correlation volume  $\Delta\eta_{\text{corr}}$ , the rapidity of the thermal particle distribution in the comoving frame ranges roughly from -1 to 1 and the observed rapidity of the particles from the correlated volume  $y = \eta + y_p$  spreads over an interval  $\Delta y_{\text{corr}} \approx 2$  units in rapidity due to the freeze-out smearing. Thus,  $\Delta y_{\text{corr}}$  is much larger than  $\Delta\eta_{\text{corr}}$  and the value of  $\Delta y_{\text{corr}}$  is not sensitive to the value of  $\xi$ . (But it is worth noting that larger values of  $\xi$  mean more correlated particles in the observed  $\Delta y_{\text{corr}}$  interval.) This means that the proposed iTPC rapidity window lies in the range of quartic growth for the magnitude of the kurtosis signal, transitioning to linear growth at the widest rapidity interval [38]. (The previous argument is based upon a generalization of the discussion about quartic moments in Ref. [39].)

At present, we have very limited theoretical guidance for the exact amplitude of the net-proton kurtosis in the presence of a critical point. This is an area being actively pursued by the theory community. But we do have guidance that emphasizes the importance of the widest possible rapidity window and actual measurements from BES I. The measured growth of the net-proton kurtosis signal is shown in Figure 2 as a function of the rapidity window ( $\Delta y$ ). The figure also shows BES-II projections following an extrapolation from the central values of the BES-I data points.

The experimental studies are limited by practical considerations such as acceptance, efficiency and kinematic cuts. Figure 2 shows that there is a rapidity width dependence for the measured net-proton kurtosis signal scaled by the variance ( $\kappa\sigma^2$ ) at 7.7 and 19.6 GeV. The magnitude of the net-proton correlation function is expected to increase rapidly with rapidity as discussed in the previous paragraphs. The BES-I data indicate that STAR's current TPC acceptance is at the lower bound of the sensitivity that is useful for theoretical analysis. Clearly we need wider rapidity acceptance; for example, see the extrapolated results shown in Figure 2. This is a crucial step in the search for the QCD critical point in the BES-II program. The iTPC expansion in pseudorapidity from  $|\eta| < 1.0$  to  $|\eta| < 1.5$  extends the size of the available window in proton "real" rapidity difference from  $|\Delta y| < 1.0$  out to  $|\Delta y| < 1.6$ , thereby greatly enhancing our ability to explore finite volume scaling effects.

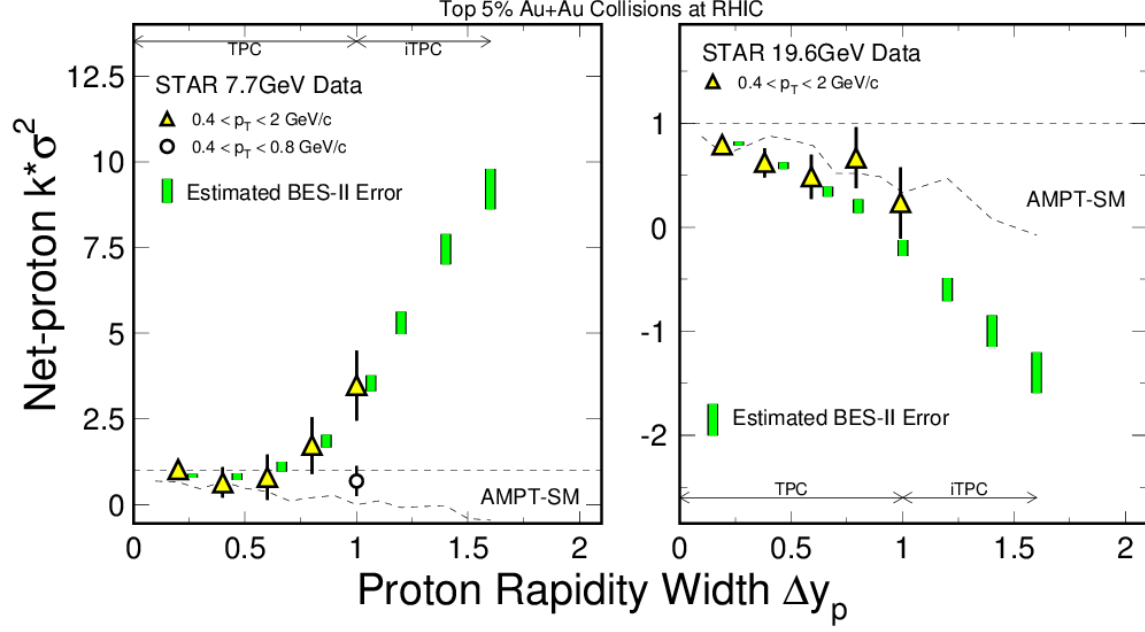


Figure 2: The observed net-proton kurtosis ( $\kappa\sigma^2$ ) as a function of rapidity window from BES I (yellow triangles). These preliminary data are for central (5%) Au+Au collisions at 7.7 GeV (left panel) and 19.6 GeV (right panel). The green bars are the estimated statistical uncertainties with the iTPC for BES-II, for 7.7 GeV and 19.6 GeV. In the extended region covered by the iTPC upgrade ( $1.0 < |\Delta y| < 1.6$ ), the error bars were estimated assuming that the variances increase linearly with rapidity width. The locations of the projected error bars illustrate one possible rapidity-window dependence of the net-proton kurtosis signal. Also shown are AMPT simulations with string melting and without a critical point (dashed lines).

The amplitude of the projection shown in Figure 2 is driven by the central values of the BES-I data points. Results from the AMPT model with string melting (SM) are also shown in the figure to illustrate the cases without a critical point but with finite baryon number conservation. Without the iTPC upgrade, one could imagine that the measured value from BES-II at large rapidity (maximum  $\Delta y = 1$ ) might be close to unity and still lie within the allowed BES-I uncertainty ( $2\sigma$ ) producing an inconclusive result. With the iTPC extension as illustrated in Figure 2, the multiple data points from BES-II covering the crucial rapidity range between 1 and 1.6 will provide a convincing assessment of the sensitivity of the net-proton kurtosis measurement to the QCD criticality.

BES-II will also have larger datasets which will reduce statistical errors. The longer measured track length of the particle trajectories will improve  $dE/dx$ -based particle identification at low momenta -- the region of largest cross section. Most important, however, is the fact that sensitivity to the critical component of the fluctuations via the skewness and kurtosis moments goes approximately as the  $3^{\text{rd}}$  power of the measurement efficiency. At present, these efficiencies are of order 10-20% at large  $\eta$ . The improvement of nearly a factor of two in the measurement efficiencies with the iTPC at large  $\eta$ , and the better low-momentum particle identification capabilities, will combine to significantly enhance the sensitivity of the multiplicity and net-proton moments analyses.

Figure 3 presents the energy dependence of efficiency corrected  $\kappa\sigma^2$  and  $S\sigma/\text{Skellam}$  of net-proton distributions with various  $p_T$  ranges for 0-5 % most central Au+Au collisions

[18]. The Skellam baseline assumes that protons and anti-protons distribute as independent Poisson distributions and it is expected to represent the thermal statistical fluctuations of the net-proton number [19]. Both  $\kappa\sigma^2$  and  $S\sigma/\text{Skellam}$  are expected to equal 1.0 at all energies in a thermal statistical model or a Hadron Resonance Gas model. The gradual enlargement in rapidity and  $p_T$  acceptance (shown in two upper panels) causes only small changes close to unity in the values of  $\kappa\sigma^2$  at energies above 39 GeV, while below 39 GeV a more pronounced structure is observed for a larger  $p_T$  and rapidity acceptance. The two lower panels show strong suppression of  $S\sigma/\text{Skellam}$  with enlarged  $p_T$  and  $y$  acceptance with respect to unity. This suppression monotonically decreases with energy. The results published earlier for  $p_T$  range from 0.4-0.8 GeV and are shown as solid red triangles in Figure 3 [18]. These studies demonstrate that the larger the acceptance is, then the larger the deviations from unity will be.

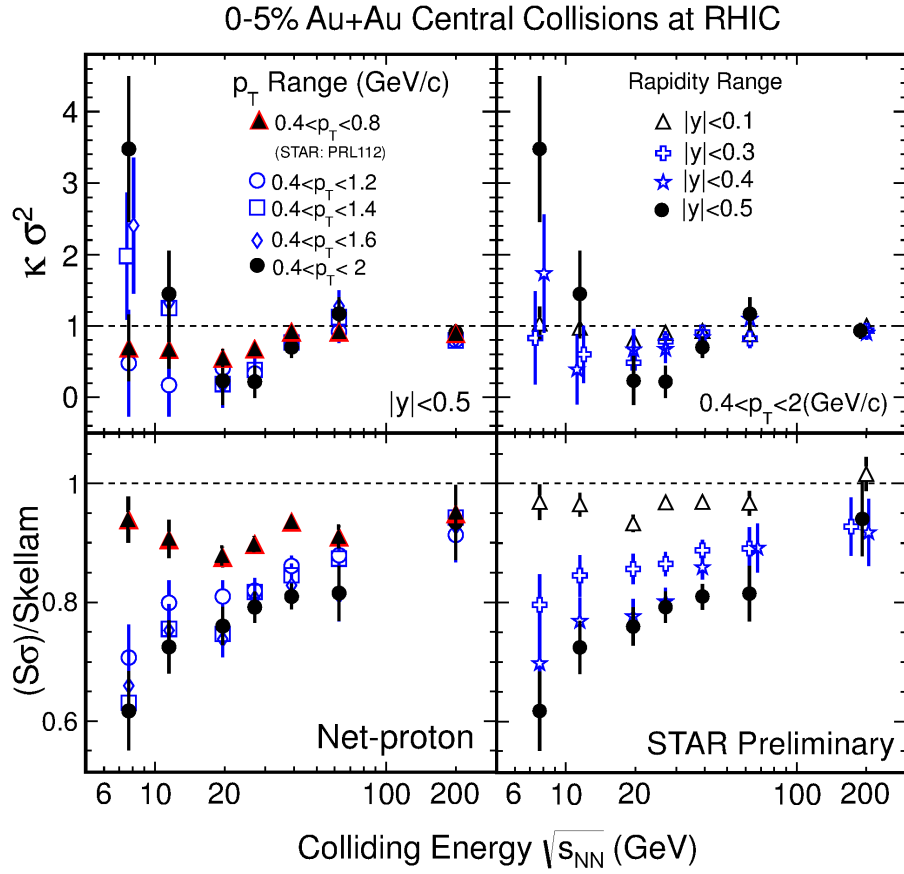


Figure 3: STAR results for beam energy dependence of  $\kappa\sigma^2$  (top panels) and  $S\sigma/\text{Skellam}$  (lower panels) for net protons [18] in Au+Au collisions. The left panels illustrate the effect of  $p_T$  selections while the right panels indicate the effects of rapidity selections. Dotted horizontal lines are expectations from Poisson distributions.

Figure 4 summarizes these studies;  $\kappa\sigma^2$  values, with their statistical errors, are shown as a function of energy (blue – extended  $p_T$  range ( $0.4 < p_T < 2$  GeV), black – original analysis ( $0.4 < p_T < 0.8$  GeV)). The red bars represent estimates of statistical errors for energies in the BES II program with the impact of the iTPC taken into account.

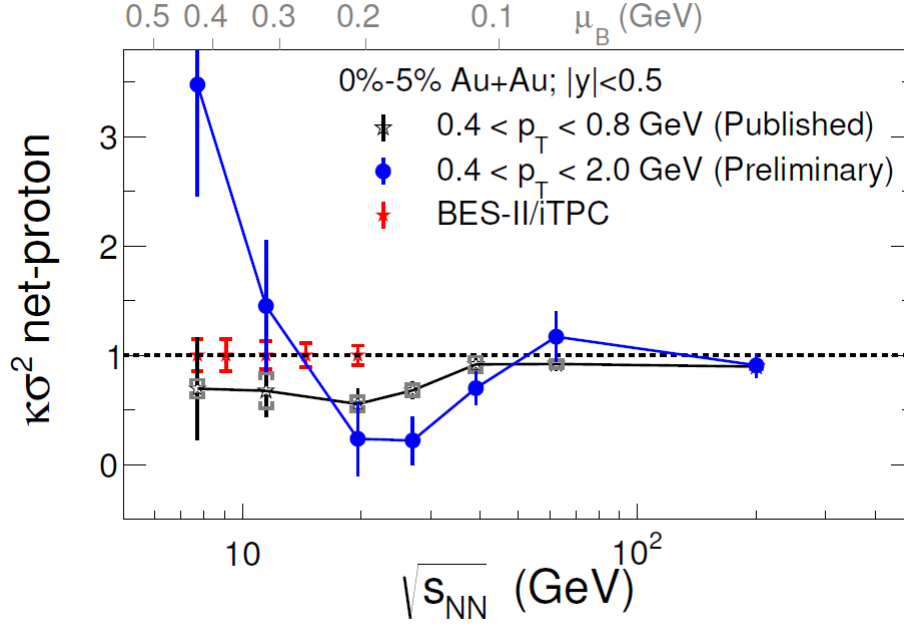


Figure 4: The plot shows the effects of  $p_T$  selections on the  $\kappa\sigma^2$  signal and the projected errors for BESII.

The estimated improved errors on measured moments due to the extended acceptance of the STAR iTPC were obtained by applying the iTPC and standard STAR TPC acceptance to model-generated events. The model uses the kinematic distributions from the HIJING event generator and then treats the production numbers as uncorrelated (Poisson for  $N_p$ , Skellam for  $N_p - N_{\text{anti-}p}$ ), so that sufficiently large event samples can be generated while being generally representative of HIJING. The analysis was then applied to these generated events using either the present acceptance or that of the iTPC.

It is clear that the larger the acceptance of the detector, the more accurate is the extracted information on moments. Our inability to measure all final-state baryons is expected to have a similar impact on our measurements as would a more limited acceptance. In this case, the net-charge cumulants have a better chance to yield sensitive results than the net-proton cumulants [20]. STAR acceptance in net-proton cumulants (which are a proxy for net-baryon) is about 0.3 times the full phase space available for the final-state protons, while in the case of net-charge, it is about 0.5 times full phase space. The iTPC would have a significant impact on both of these analyses, since it extends the available acceptance and yields by about 50%.

In conclusion, we note that the iTPC upgrade will enable analyses in a much larger  $\eta$  range ( $-1.5 < \eta < 1.5$ ). Therefore, we get improvements not only on the magnitude of statistical errors but also on the magnitude of the signal itself, which will provide much smaller relative errors. The Forward TOF (eTOF) upgrade, presently under study in STAR, will extend STAR PID capabilities into this new range of rapidity. The present TOF covers range of  $|\eta| < 1$ , but with a forward upgrade it will cover  $|\eta| < 1.7$ ; which is a good match to the iTPC.

## 2.2 Key Measurements II: Di-electron Invariant Mass Spectra

Di-leptons are a crucial probe of the strongly interacting matter created in ultra-relativistic heavy ion collisions. Leptons are produced during the whole evolution of the created matter and can traverse the medium with minimal interactions. Different kinematics of di-lepton pairs (mass and transverse momentum ranges) can selectively probe the properties of the formed matter throughout its entire evolution. In the low invariant mass range of produced lepton pairs ( $M_{\ell\ell} < 1.1 \text{ GeV}/c^2$ ), vector meson in-

medium properties (mass and width of the  $\rho(770)$ ,  $\omega(782)$ , and  $\phi(1020)$  spectral functions) may be studied via di-lepton decays and may exhibit modifications related to possible chiral symmetry restoration. Also, in the higher  $p_T$  range, direct photon yields were derived through di-electron measurements at RHIC, allowing an assessment of thermal radiation. Additional precision experiments with large acceptance and a broad range of beam energies can provide invaluable insights in this subject.

The di-lepton spectra in the intermediate mass range ( $1.1 < M_{\ell\ell} < 3.0 \text{ GeV}/c^2$ ) are expected to be directly related to the thermal radiation of the Quark-Gluon Plasma. However, significant background contributions from other sources have to be measured experimentally. Such contributions include background pairs from correlated open heavy-flavor decays, which produce a pair of electrons or muons from the semi-leptonic decay of a pair of open charm or bottom hadrons:  $\bar{c}c \rightarrow l^+l^-$  or  $\bar{b}b \rightarrow l^+l^-$ . In the high-mass region ( $M_{\ell\ell} > 3.0 \text{ GeV}/c^2$ ),  $J/\psi$ ,  $\Upsilon$  and their excited states are used to study the color screening features of the QGP.

It has been generally accepted that the properties of the vector mesons change dramatically from vacuum to the hot and dense medium created in relativistic heavy ion collisions, which creates an enhancement in the di-lepton yields at low  $p_T$  and low invariant mass between the pion and  $\rho$  mass as recently observed at SPS and RHIC. The key question is how to connect this modification to the possible chiral symmetry restoration expected at the high temperature achieved at RHIC and the LHC. Dynamic models [29] show that the width broadening of the  $\rho$  can be attributed to the interactions with the surrounding nuclear medium, i.e. to the coupling of the  $\rho$  to the baryons, anti-baryons, and their resonances. These interactions affect the properties of the  $\rho$  even in the cold nuclear matter. In hot nuclear matter, where temperature and/or total baryon (the sum of baryon and anti-baryon) density is high, they are expected to cause the width to broaden to the extent that it becomes indistinguishable from the continuum radiation. This continuum radiation coincides with the di-lepton thermal radiation from QGP at the phase transition temperature. A key observable would then be a temperature and total baryon density dependence of the di-lepton excess yields at low mass.

BES-II and the iTPC upgrade will enable STAR to measure dielectron invariant mass spectra from 7.7 to 19.6 GeV and improve our fundamental understanding of hot QCD matter. High-statistics datasets from the SPS fixed target program have established that in-medium broadening of vector mesons is a possible indication of Chiral Symmetry

Restoration (CSR). To date, the results from RHIC top energy and BES-I programs show that models incorporating temperature dependence of hadron structure and thermal radiation are consistent with our data. However, with limited statistics and large systematic uncertainties, we are neither able to test the baryon-density dependence nor able to constrain different model implementations. In BES-II, we will be able to quantitatively assess the evolution of hadron structure toward CSR at high baryon density (low beam energies) using high statistics data sets enabled by the collider cooling upgrade and by the improved uncertainties for particle identification and acceptance at low momentum due to the iTPC detector upgrade.

The iTPC upgrade will reduce the systematic uncertainties due to hadron contamination, efficiency corrections, acceptance differences between unlike-sign and like-sign pairs, and cocktail subtraction. These improvements will result in a factor of 2 improvement in the systematic uncertainties for the di-electron excess yield. In addition, the iTPC will extend the acceptance of low-momentum electrons from  $p_T > 0.2$  to  $p_T > 0.1$  GeV/c. This improves the acceptance of the dielectron measurement by more than a factor of 2 in the low mass region ( $0.4 < \text{mass} < 0.7$  GeV). Only with these improvements will we be able to distinguish models with different  $\rho$ -meson broadening mechanisms; for example, the Parton-Hadron String Dynamic (PHSD) transport model versus Rapp's microscopic many-body model with macroscopic medium evolution. Knowing the mechanism that causes in-medium  $\rho$  broadening and its temperature and baryon-density dependence is fundamental to our understanding and assessment of chiral symmetry restoration in hot QCD matter.

Figure 5 shows the measured di-electron invariant mass spectrum in Au+Au collisions at  $\sqrt{s_{NN}} = 19.6$  GeV. The data are compared to a hadronic cocktail resulting from the decay of light hadrons, correlated charm decays, and Drell-Yan contributions. An enhancement of the dielectron yield is observed in the mass region  $< 1$  GeV/c<sup>2</sup>. A model calculation with a broadened  $\rho$  spectral function is added to the hadronic cocktail and compared with the data up to 1.5 GeV/c<sup>2</sup>. The comparison of the model with data shows that a broadened  $\rho$ -spectra scenario is consistent with STAR data within uncertainties [30].

To quantify the yield, the known hadronic cocktail, correlated charm decays, and Drell-Yan contributions can be subtracted from the dielectron mass spectrum. Figure 6 shows the expected dielectron excess invariant mass spectra in Au+Au collisions at  $\sqrt{s_{NN}} = 19.6$  GeV in BES-II with and without the iTPC. Comparisons to PHSD and Rapp's model calculations are also shown in the figure [31-36]. Only with the iTPC upgrade, we will be able to distinguish models with different  $\rho$ -meson broadening mechanisms.



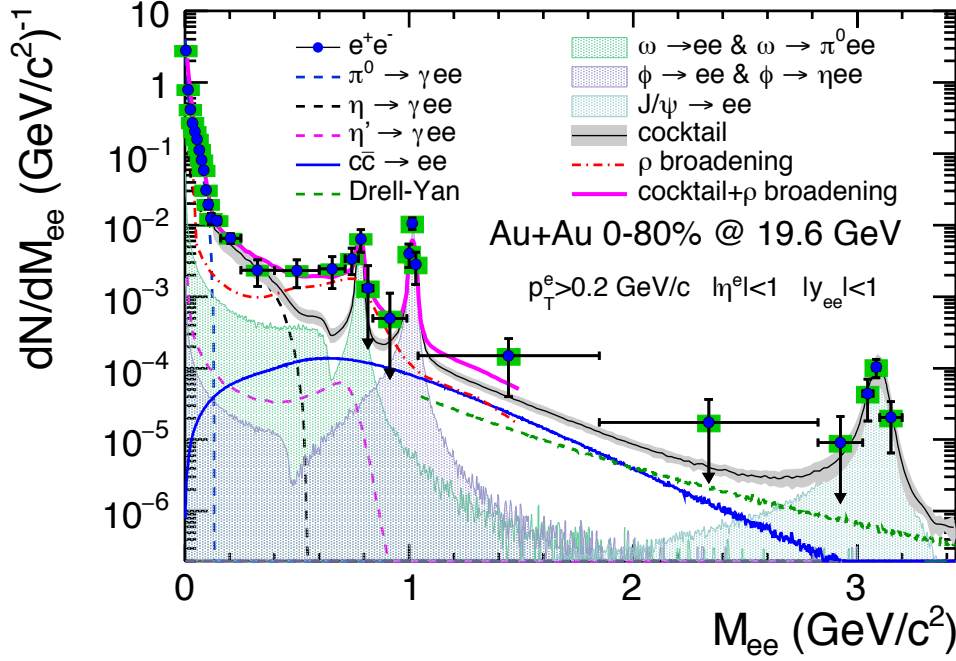


Figure 5: Dielectron invariant mass spectrum in the STAR acceptance ( $|y_{ee}| < 1$ ,  $0.2 < p_T < 3$  GeV/c,  $|\eta| < 1$ ) after efficiency corrections, compared with the hadronic cocktail consisting of the decays of light hadrons and correlated decays of charm in Au+Au collisions at  $\sqrt{s_{NN}} = 19.6$  GeV. Theoretical calculations of a broadened  $\rho$  spectral function are shown up to  $1.5$  GeV/c<sup>2</sup> for comparison. Systematic uncertainties for the data points are shown as green boxes, and the grey band represents the uncertainties for the cocktail simulation.

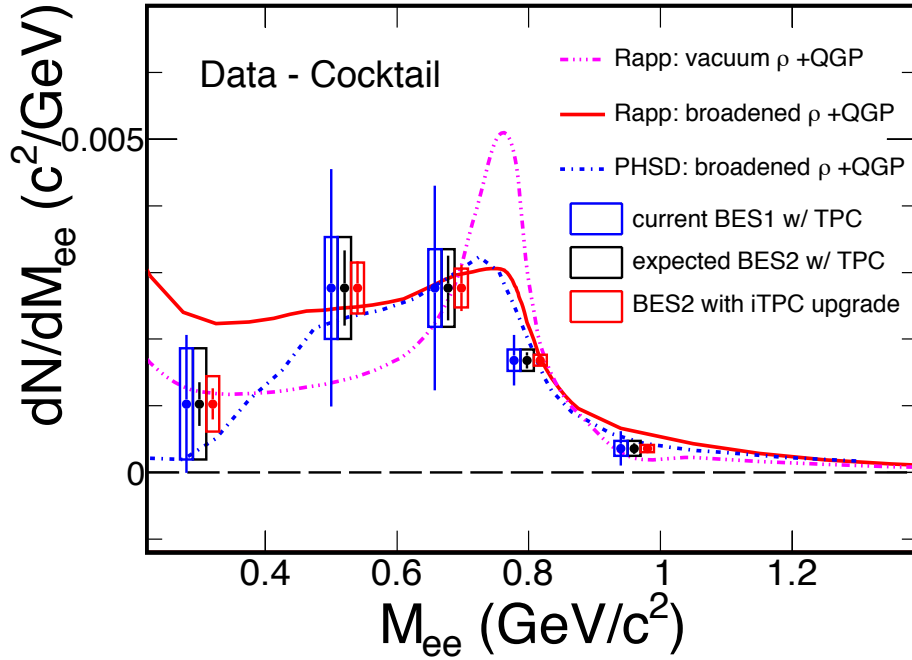


Figure 6: The expected dielectron excess invariant mass spectra in Au+Au collisions at  $\sqrt{s_{NN}} = 19.6$  GeV in BES-II with and without iTPC. Comparisons to PHSD and Rapp's model calculations are also shown. The bars and boxes represent the statistical and systematic uncertainties, respectively.

Figure 7 shows the projected BES II measurements from STAR, with the iTPC, together with data already taken at higher beam energies and compared to recent model calculations. STAR detectors in the BES-II era will cover a unique energy range because the excitation function above 20 GeV for the low mass region (LMR) depends strongly on initial temperature, while the LMR excess below 20 GeV depends more strongly on baryon density.

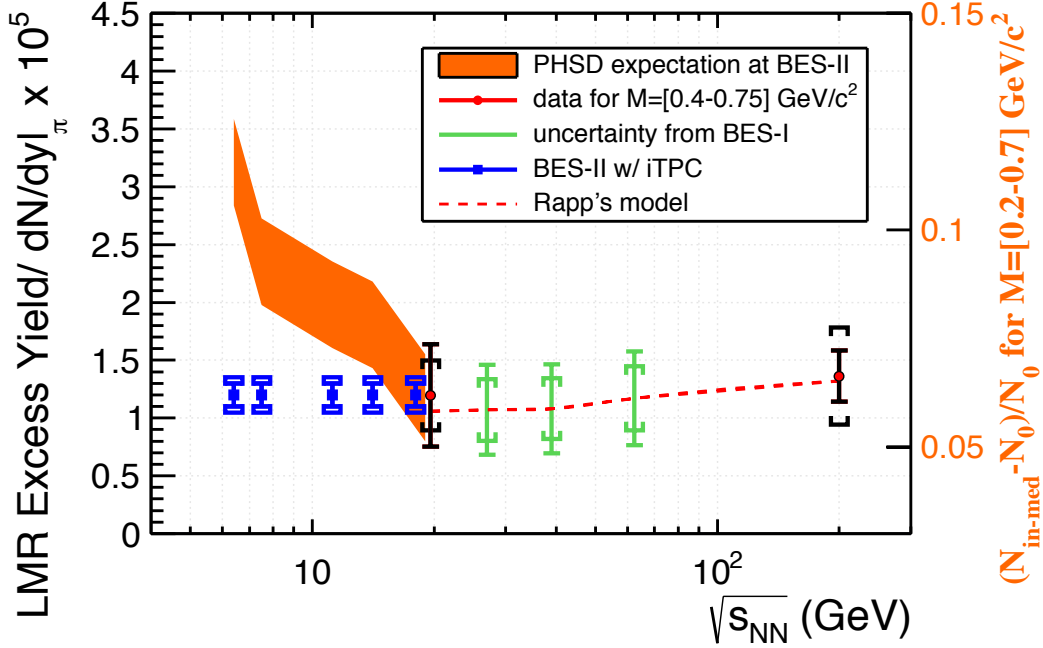


Figure 7: The Beam Energy dependence for the Low-Mass dielectron excess from published data at 19.6 and 200 GeV, model expectation from PHSD for energy below 20 GeV and Rapp's model above 20 GeV. Also shown are projected sys. and stat. errors from preliminary results at 27, 39 and 62.4 GeV, and projections for BES-II with the iTPC. Projections without the iTPC for these energies would have  $\times 2$  ( $\sqrt{2}$ ) bigger sys. (stat.) errors.

Due to the nature of relativistic heavy ion collisions, the observed inclusive di-lepton yields at low mass have contributions from many sources integrated over the entire evolution of a collision. During BES-I running, STAR collected dielectron data for minimum-bias Au+Au collisions at  $\sqrt{s_{NN}} = 39, 27$  and 19.6 GeV. Figure 8 shows preliminary efficiency-corrected inclusive dielectron invariant mass spectra for these three beam energies, as well as for 62.4 GeV. The data are compared to a cocktail simulation including contributions from all the known hadronic decays of light mesons and correlated charm pairs. A low-mass dielectron excess is observed across all the collision energies, indicating hot, dense medium contribution. A broadened  $\rho$  spectral function [29], which describes SPS dilepton data, consistently accounts for the STAR low mass excess in Au+Au collisions at 19.6, 27, 39, 62.4, and 200 GeV (see Figure 8).

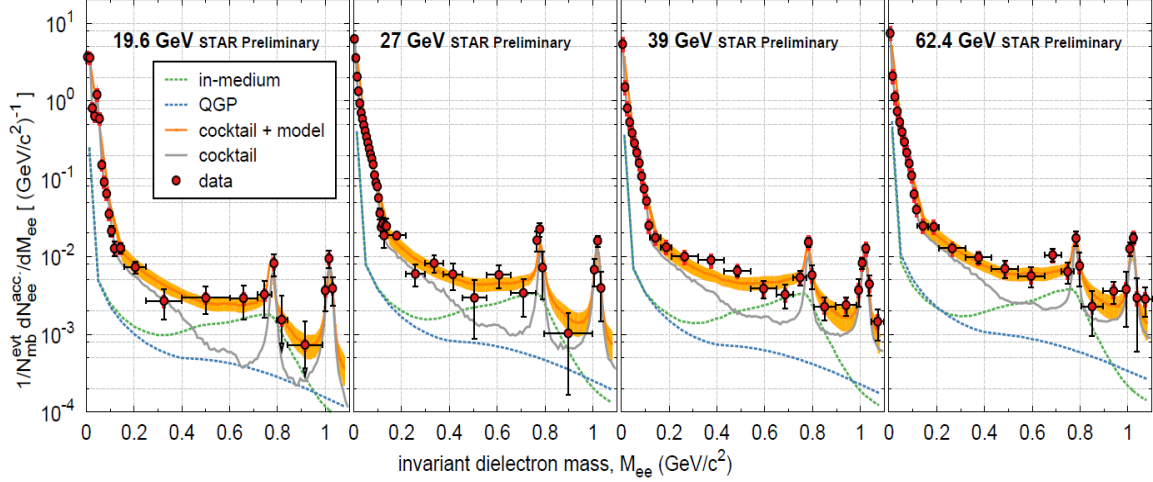


Figure 8: Preliminary STAR measurements of dielectron invariant mass distributions below 1.1  $\text{GeV}/c^2$  for  $\sqrt{s_{\text{NN}}} = 19.6, 27, 39$  and  $62.4$  GeV. The grey cocktail curve includes all known hadronic sources apart from the  $\rho$  (which is included in the model). The orange band includes a model calculation [29] with contributions from both hadron gas and QGP phases.

In the model calculation [29], coupling to baryons plays an essential role in the modification of the  $\rho$  spectral function in the hot, dense medium. Figure 9 shows the sum yield of protons and antiprotons over that of  $\pi^+$  and  $\pi^-$  as a function of collision beam energy. This ratio represents the total baryon density at freeze-out. The figure shows that from 19.6 to 200 GeV CM energy, the ratio is almost independent of beam energy. Consequently, our measurements from 19.6 to 200 GeV probe the temperature and system evolution dependence. With the total baryon density nearly a constant and the dilepton emission rate dominant in the critical temperature region at  $\sqrt{s_{\text{NN}}} = 19.6\text{-}200$  GeV, the normalized excess dilepton yields in the low mass region from the measurements are proportional to the calculated lifetimes of the medium [37], as reported in a recent STAR publication [30] and shown in Figure 10.

In order to be sensitive to the total baryon density effect, one needs to have measurements at lower energies. At  $\sqrt{s_{\text{NN}}} = 7.7$  GeV, it is found that the total baryon density increases by a factor of two, as indicated in Figure 9. Current data at 7.7 and 11.5 GeV at RHIC are not sufficient for dilepton analysis. The future measurements from the Beam Energy Scan Phase II, at RHIC, will map out the dependence of the modified  $\rho$  spectral function on the total baryon density from 7.7 to 19.6 GeV Au+Au collisions. In addition, the centrality and energy dependent low-mass dielectron excess yields will probe the interplay of the lifetime and the total baryon density effects. In a broadened  $\rho$  spectral scenario [37], it was pointed out that the excess dielectron yield at low mass is proportional to the total lifetime of the hot, dense medium at  $\sqrt{s_{\text{NN}}} = 6\text{-}200$  GeV. A significant enhancement in the low-mass dielectron excess yields, which deviates from the systematic energy-dependent trend might indicate a critical slow-down behavior at a certain energy point.

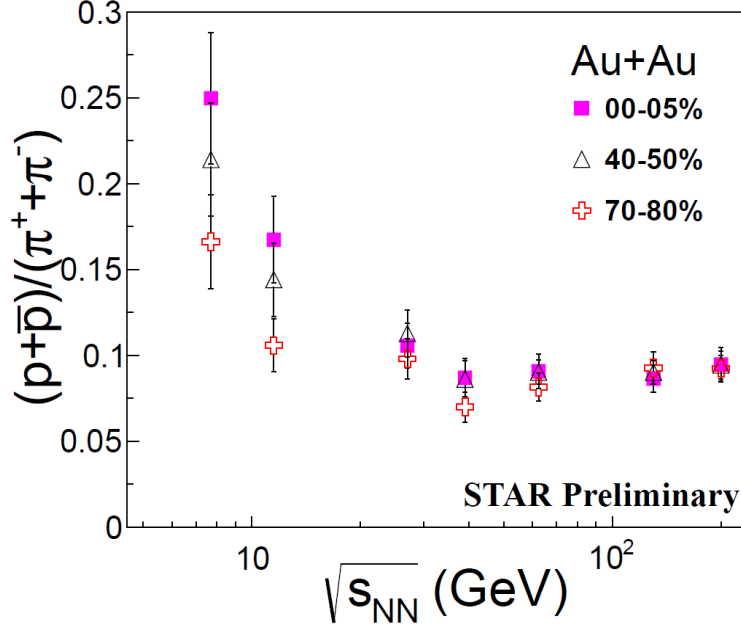


Figure 9: Total baryon density, represented by  $(p+\bar{p})/(\pi^++\pi^-)$ , vs. beam energy at RHIC.

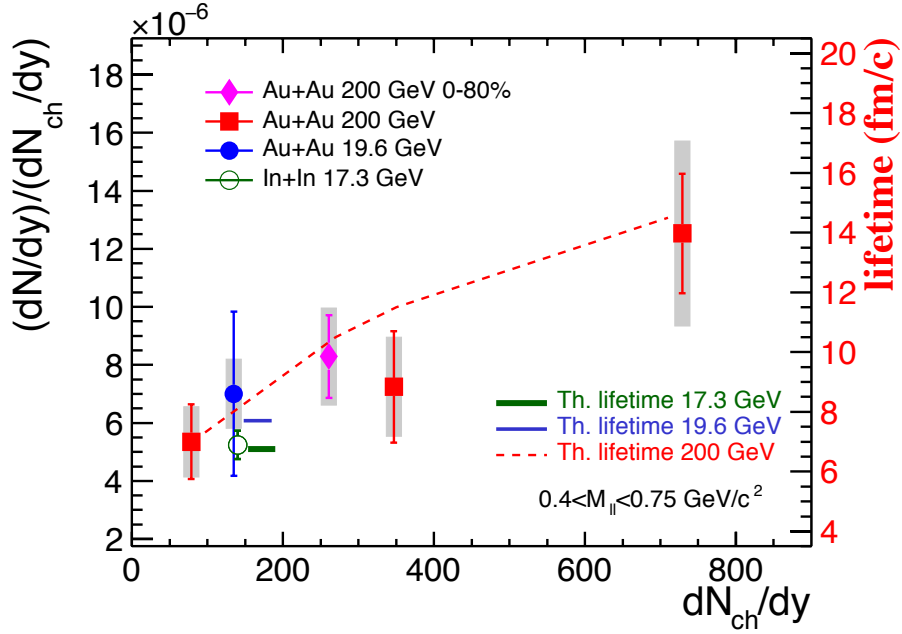


Figure 10: Integrated yields of the normalized dilepton excesses for  $0.4 < M_{l\bar{l}} < 0.75 \text{ GeV}/c^2$  as a function

of  $dN_{ch}/dy$ . The solid circle and diamond represent the results in 0-80% Au+Au collisions at  $\sqrt{s_{NN}} = 19.6$  and 200 GeV, respectively. The squares are the results for 40-80%, 10-40%, and 0-10% Au+Au at  $\sqrt{s_{NN}} = 200$  GeV. The open circle represents the dimuon result from the NA60 measurement with  $dN_{ch}/d\eta > 30$ . Bars are statistical uncertainties, and systematic uncertainties are shown as grey boxes. The theoretical lifetimes for  $\sqrt{s_{NN}} = 200$  GeV Au+Au as a function of  $dN_{ch}/dy$  in the model calculations [37] are shown as a dashed curve. The lifetimes for  $\sqrt{s_{NN}} = 17.3$  GeV In+In and  $\sqrt{s_{NN}} = 19.6$  GeV Au+Au in the same model calculations [37] are shown as the two horizontal bars. The  $dN_{ch}/dy$  values for the horizontal bars are shifted for clarity.

On the other hand, dilepton excess spectra in the intermediate mass range are directly related to the thermal radiation of the QGP. The charm cross section at 7.7-19.6 GeV is small, thus the charm pair correlated contribution can be subtracted reliably with reasonable assumptions. From its intermediate mass region of the dielectron excess spectrum, one can obtain the temperature of the emitting source.

The beam energy scan phase II will enable STAR to have measurements of dielectron excess invariant mass spectra from 7.7 to 19.6 GeV. The energy-dependent measurements will enable us to study the dielectron emission utilizing a completely new degree of freedom, namely, the total baryon density effect, in the critical temperature region. The goal is to systematically map out the lifetime and temperature of the medium created in heavy-ion collisions using low- and intermediate-mass dielectrons and to observe a possible signature of chiral symmetry restoration across different collision energies.

We propose to collect high-statistics datasets in BES-II to systematically study the dilepton spectrum as a function of beam energy. The iTPC upgrade is crucial for this important and challenging measurement. The iTPC provides significant improvement in  $dE/dx$  resolution for electron identification and acceptance. Figure 11 shows the current  $dE/dx$  distribution from data. In this  $p_T$  window, a significant pion contamination (red dashed) of the  $dE/dx$  distribution of electrons (blue dashed) can be observed. The improved resolution from the iTPC reduces the individual contributions of the pions (red solid), resulting in significantly reduced contamination in the electron sample. Figure 12 illustrates the fact that the iTPC will deliver a comparable improvement over a wide range of  $p_T$  windows. STAR has performed a detailed study of dielectron measurements in Au+Au collisions at  $\sqrt{s_{NN}}=19.6$  GeV [30]. The dominant systematic uncertainty is hadron contamination due to misidentification of hadrons as electrons in the  $dE/dx$  distribution. The uncertainty is up to 20% in the mass range of interest. With only one week of data-taking at 19.6 GeV in 2010, the dominant uncertainty is from statistics as presented in the paper. In BES II, with the proposed beam time, a statistical uncertainty of 10% is achievable and required. The iTPC upgrade reduces the hadron tail contamination by more than an order of magnitude and makes this source of contamination a negligible contribution to the errors in the measurement in comparison to the statistical uncertainty.

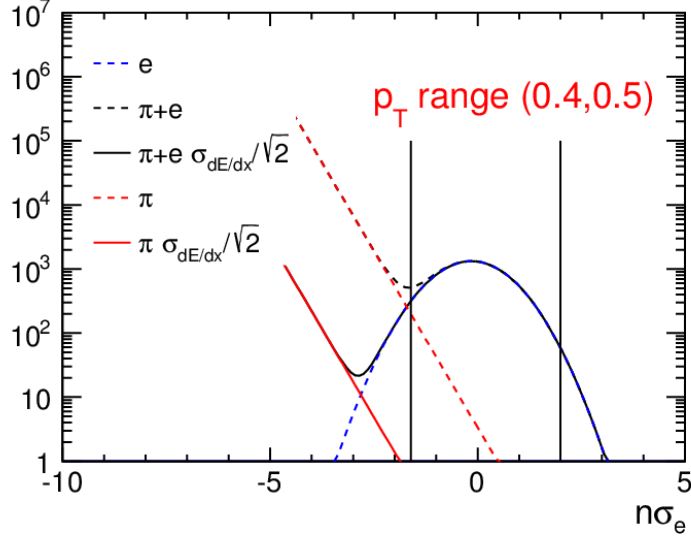


Figure 11:  $dE/dx$  of electrons and hadron background, as a function of  $n\sigma_e$ , for  $0.4 < p_T < 0.5$  GeV/c. The blue Gaussian curve is the electron  $dE/dx$  while the red dashed line is a fit to the measured hadron  $dE/dx$ . The solid red line is the expected hadron contamination with the improved tracking of the iTPC.

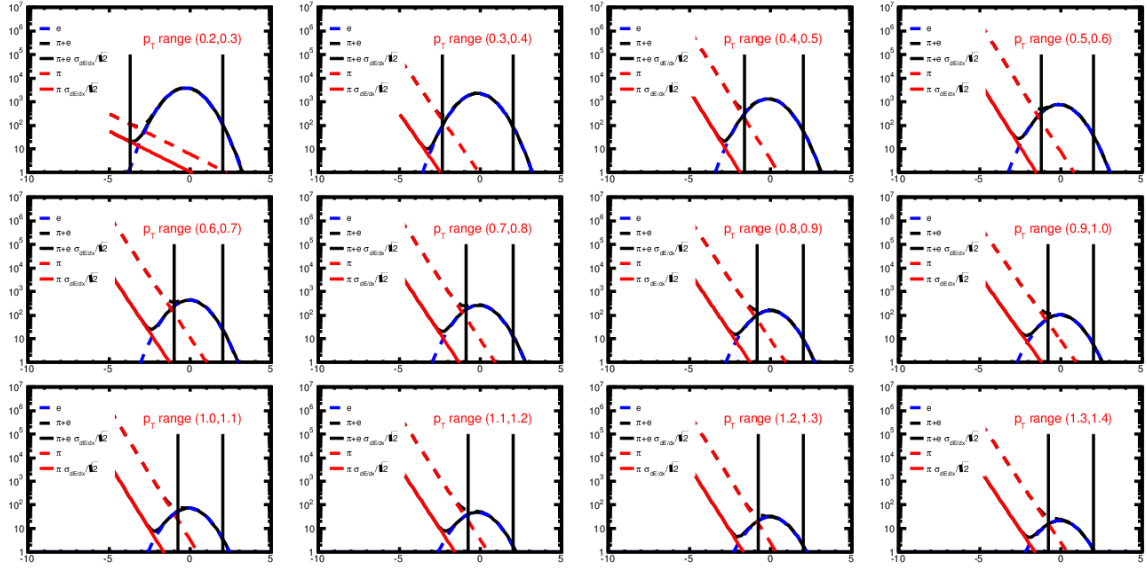


Figure 12: These panels demonstrate the iTPC improvement for 12 different  $p_T$  intervals, following the same scheme as plotted in the previous figure.

Figure 13 shows the electron purity as a function of momentum. One can see that in the hadron cross-over region, the electron purity with the iTPC upgrade will be similar to that with the current TPC. However, the hadron tail contamination will become negligible as indicated by the data points above 1.5 GeV/c. This will reduce the systematic uncertainties on the dielectron mass spectrum caused by hadron contamination from 2% to 0% at  $M_{ee}=0.2$  GeV/c<sup>2</sup> and enable dielectron mass spectrum measurements in the transverse momentum region greater than 3 GeV/c.

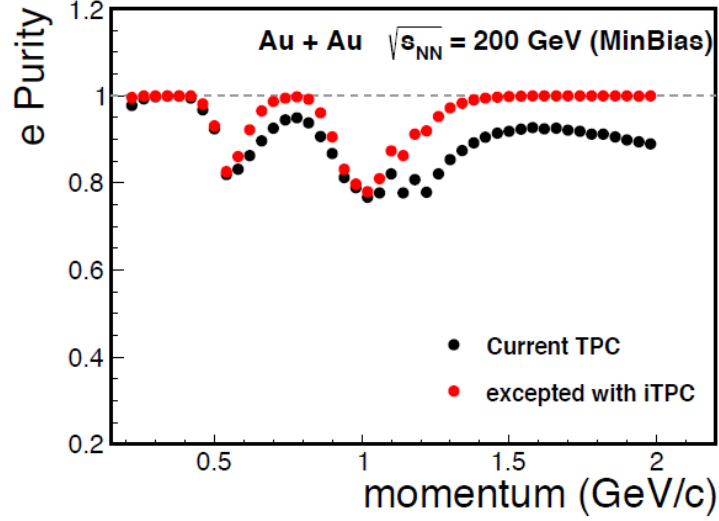


Figure 13: The expected purity for electrons as a function of transverse momentum. The black symbols show the purity using the current TPC. The improved purity with the iTPC is shown in red symbols.

The iTPC will significantly enlarge the acceptance for charged hadrons. For the dielectron analysis, electrons and positrons will be identified down to transverse momentum 0.1 GeV/c with the iTPC upgrade. Figure 14 shows dielectron acceptance with the iTPC upgrade compared to that with the current TPC. The acceptance correction is estimated by a Monte Carlo simulation with inputs of virtual photon yield spectra, phase space distributions and decay kinematics. The acceptance difference between two input spectra, the cocktail mass spectrum versus the flat mass case, will contribute to systematic uncertainties for the acceptance-corrected dielectron excess mass spectra. With the iTPC upgrade, the acceptance will be increased by more than a factor of 2 in the dielectron mass region  $M_{ee} < 0.4 \text{ GeV}/c^2$ .

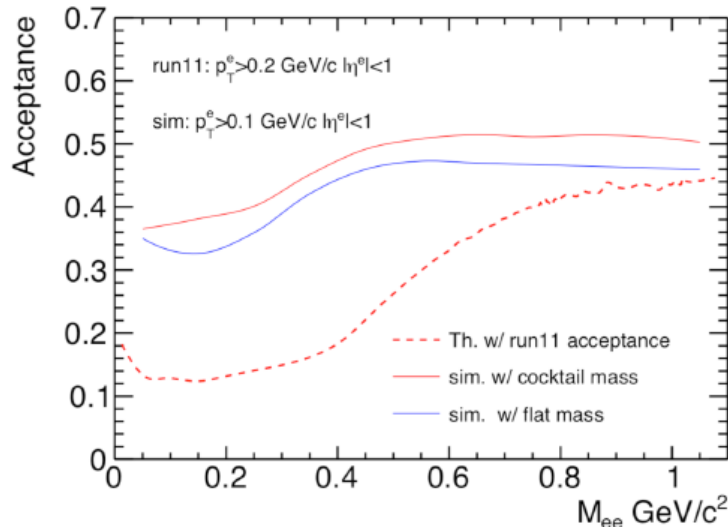


Figure 14: The electron acceptance using the current TPC (dashed red line) and the expected improvement using the iTPC under two different assumptions (red and blue lines).

Due to the sector structure of the TPC, and the different bending directions of positively and negatively charged particle tracks in the transverse plane, like-sign and unlike-sign

pairs have different acceptances. The correction for this acceptance difference is applied to the same-event like-sign pair distribution before background subtraction. The acceptance difference between same-event unlike-sign and same-event like-sign pairs is obtained using the mixed-event technique. Figure 15 shows the acceptance difference factor, the ratio of the mixed-event unlike-sign to the mixed-event like-sign electron pair invariant mass distributions, with the iTPC upgrade. With the iTPC upgrade, the acceptance difference factor is negligible and the uncertainties on the dielectron mass spectrum from this factor should be significantly reduced.

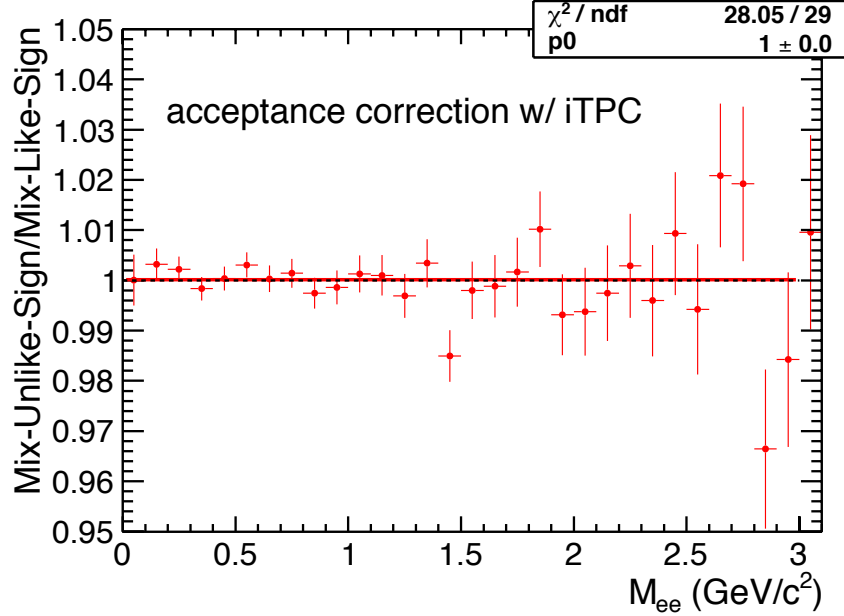


Figure 15: The acceptance difference factor, the ratio of the mixed-event unlike-sign to the mixed-event like-sign electron pair invariant mass distributions with the iTPC upgrade.

The iTPC will significantly improve the tracking efficiency for charged hadrons. In addition, it will reduce the efficiency uncertainties from 5% to 1-2%. We estimate with this improvement, the cocktail uncertainties for  $\pi^0$ ,  $\omega$ , and  $\psi$  decays will be significantly reduced (a factor of two). In addition, the single electron efficiency uncertainties will also be reduced. The expected systematic uncertainties on  $\pi$ ,  $\omega$ ,  $\psi$ ,  $\eta$ ,  $\eta'$ , and charm cocktail contributions, acceptance correction factor, and single electron efficiency with the iTPC upgrade will be reduced. With the improvement, the systematic uncertainties of dielectron excess mass spectrum will be reduced by a factor of 2, as shown previously in Figure 6.

To conclude this section on low mass dielectron measurements, it is worth noting that the iTPC upgrade improves the acceptance of the detector but also reduces the hadron contamination which is the dominant source of systematic uncertainties in previous measurements. The reduction in uncertainty made possible by the iTPC project will allow the full exploitation of the increased statistics to be collected during BES-II.



### 2.3 Key Measurements III: Study of the QCD phase diagram

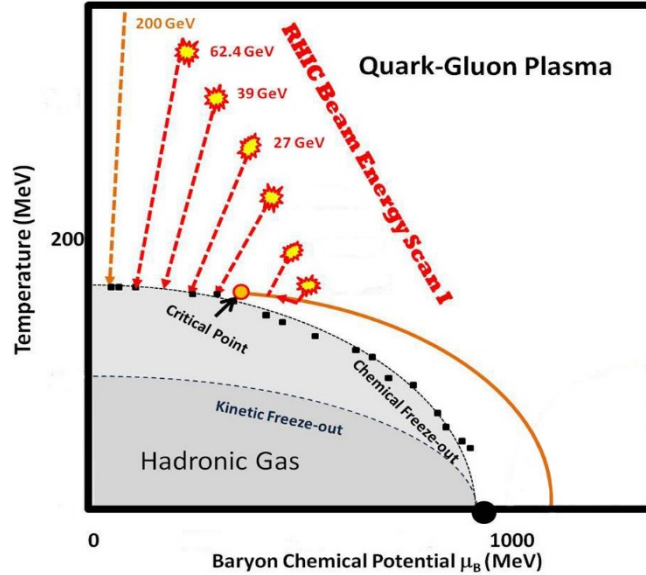


Figure 16: A schematic version of the QCD phase diagram. Overlaid are conceptual illustrations of reaction trajectories for central collisions.

Much progress has been made in understanding the phase diagram of QCD matter. Both theory and experiment [1] support the interpretation that a crossover transition occurs at beam energies of several tens of GeV and above. At lower energies, there is likely to be a first-order phase transition, with a critical point located where the boundary changes from a first-order phase transition to a smooth crossover. Mapping the features of the QCD matter phase diagram is a key objective. In 2009, the RHIC PAC approved a Beam Energy Scan (BES) Program with a set of six new energies to search for 1) the turn-off of QGP signatures observed at top RHIC energies, 2) evidence of a first-order phase transition, and 3) evidence of a critical point. The RHIC facility has successfully completed Phase-I of the BES program (BES-I). A disappearance of QGP signatures was indeed seen in the breakdown of constituent quark scaling of elliptic flow at beam energies below 19.6 GeV, in the disappearance of high  $p_T$  suppression for energies near 27 GeV, and in the collapse of charge separation that may be due to collapse of the Chiral Magnetic Effect below 11.5 GeV. There still remains some uncertainty in interpreting these observations, *i.e.*, it can be a challenge to unambiguously distinguish between a scenario where QGP production itself disappears, and the alternative picture in which our sensitivity to a QGP signature fades away. Hints of a first-order phase transition are seen in directed flow for protons and net-protons. The measured directed flow signature at intermediate centralities has good statistical significance, but as amplified in the section that follows, the best available models show poor agreement with data and a clear physics interpretation requires further study.

### 2.3.1 iTPC-based improvements in measurement of baryon directed flow

Directed flow excitation functions have been proposed by Frankfurt theorists as promising observables for uncovering evidence of crossing a first-order phase transition, based on hydrodynamic calculations [2, 3, 4]. Figure 17 (left panel), based on a 3-fluid hydrodynamic model [3], presents directed flow for net baryons as a function of beam energy. Note that the older  $\langle p_x \rangle$  directed flow observable used here is proportional to  $v_1$ . A first-order phase transition leads to a softening of the Equation Of State (EOS), and this in turn causes the predicted proton directed flow to change sign from positive to negative near  $\sqrt{s_{NN}} = 4$  GeV. The directed flow prediction crosses back to positive again as the beam energy increases further. This phenomenon is referred to in the theory literature as the “softest point collapse” of flow [3].

Directed flow measured by STAR for protons (upper panel) and net protons (lower panel) is presented on the right side of Figure 17, for Au+Au collisions at intermediate centrality [5]. The plotted quantity is the slope of  $v_1(y)$  near mid-rapidity. The net-proton slope shown in panel b) is a proxy for the directed flow slope of protons associated with baryon number transported from the initial state to the vicinity of mid-rapidity, based on the assumption that produced baryon-antibaryon pairs have similar directed flow and baryon-antibaryon annihilation does not alter the directed flow[5].

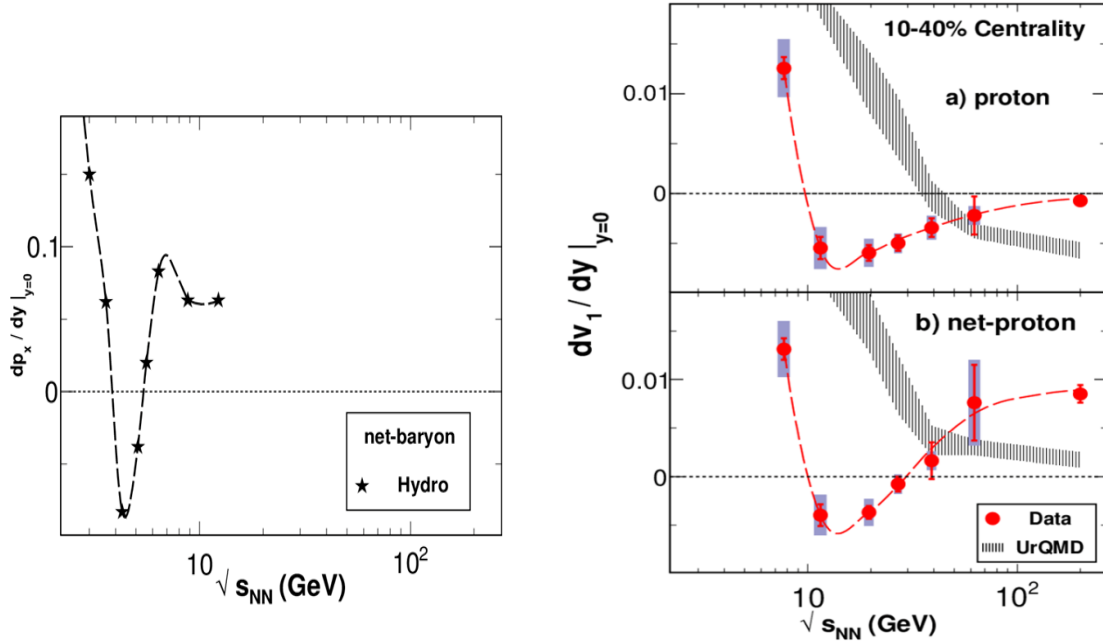


Figure 17: **Left:** Directed flow prediction in units of GeV/c as a function of beam energy, based on a three-fluid hydrodynamic model [3] whose EOS incorporates a first-order phase transition. **Right:** panel a) shows the slope of directed flow vs. beam energy for protons from Au+Au collisions at intermediate centrality. Panel b) presents the same for net protons. The prediction of the UrQMD transport model [6] is also plotted in panels a) and b).

The proton slope changes sign from positive to negative between 7.7 and 11.5 GeV, shows a minimum between 11.5 and 19.6 GeV, and remains small but negative up to 200 GeV, while the net-proton slope shows a similar minimum, but changes sign back to

positive near the measured energy of 27 GeV. In contrast, there is no hint of this non-monotonic behavior in the UrQMD hadronic transport model [6] that has a good record of reproducing observed trends at least at a qualitative level. The observed beam energy of the minimum is about a factor 4 higher than the hydro prediction shown on the left in Figure 17. Theory comparisons that followed the publication of STAR’s measurements of directed flow have overall not strengthened either the hadronic or the phase transition interpretations. Specifically, recent hydrodynamic calculations [7] confirm the prediction on the left of Figure 17 but with a much larger magnitude of  $v_1$  slope than the data, while hydro with a more realistic prescription for particle freeze-out has a much reduced minimum and no sign change [7]. A recent hybrid calculation by the same authors, featuring Boltzmann transport with an intermediate hydrodynamic stage, does not show a minimum or a sign change in  $v_1$  slope for any assumed EOS [7]. The Parton-Hadron String Dynamics transport model does not show a minimum in  $v_1$  slope for any assumed EOS [8].

There is an important connection between the search for a first-order phase transition and the search for a critical point. A confirmed observation of a first-order phase transition would imply that a critical point must exist, by ruling out a hypothesized scenario where the boundary between hadronic matter and QGP is a smooth crossover throughout the phase diagram. Such an observation would also have implications for the allowed and excluded locations in  $\mu_B$  of the critical point. While model comparisons to date have underlined the importance of further theoretical work in order to reach a confident interpretation, new experimental data are also essential for a definitive conclusion.

Because of the strong non-monotonic behavior observed for protons and net protons, other baryon species like  $\Lambda$ s are of special interest and will have excellent statistics in BES-II with the iTPC upgrade. To better understand the possible role and relevance of stopping in the interpretation of directed flow, new higher-statistics measurements as a function of centrality will be especially valuable. Although BES-I statistics are insufficient for a systematic study of the centrality dependence of directed flow, it is noteworthy that at low BES energies,  $v_1(y)$  magnitudes appear to increase roughly a factor of 5 when going from intermediate centralities to more peripheral centralities. Normally, anisotropic flow coefficients exhibit far less centrality dependence over this range, and so this unusual pattern is highly deserving of targeted investigation in BES-II.

After the greatly improved BES-II measurements, any possible future explanation of  $v_1$  data in terms of purely hadronic physics would have to predict the detailed phenomenology of the centrality, rapidity, and transverse momentum dependence of directed flow for various particle species as a function of beam energy. Owing to the steeply declining RHIC luminosity as the beam energy was lowered during BES-I, our current statistics are inadequate for detailed directed flow measurements as a function of centrality, rapidity and transverse momentum. However, simulations described below indicate that the improved statistics and extended rapidity acceptance of the iTPC, in combination with improved RHIC luminosity in the future, will be sufficient to meet this challenge. The restriction of measurements to the region near mid-rapidity is a serious limitation that must be overcome in order to reach a full understanding of the physics.

Figure 18 illustrates the improved rapidity coverage of the iTPC via the extrapolated cubic and linear fits to  $v_1(y)$  for protons at 7.7 GeV measured in BES Phase-I. Clearly the extrapolation to higher rapidity is a major source of systematic error in this analysis and it will be significantly reduced by the extended rapidity coverage made available by the iTPC. Of course, statistical errors are liable to be quite large at the rightmost end of the extrapolated fit curves as well; see the discussion below for some quantitative information about expected improvement in statistical errors with the iTPC. The most significant point of the left-side panel of Figure 18 is that with the present rapidity coverage of the STAR TPC,  $v_1(y)$  carries insufficient information to go much, if at all, beyond a study of a single parameter like the slope  $dv_1/dy$  averaged over the current rapidity acceptance, especially when statistics are limited. In contrast, the much wider  $v_1(y)$  coverage of the iTPC opens the possibility to go well beyond a study of the single number yielded by the average slope just described. In light of the fact that proton and net-proton  $v_1$  near  $y = 0$  have proven to be a highly promising signature, it is clearly of great interest and importance to extend the same form of analysis to the adjacent regions away from  $y = 0$ .

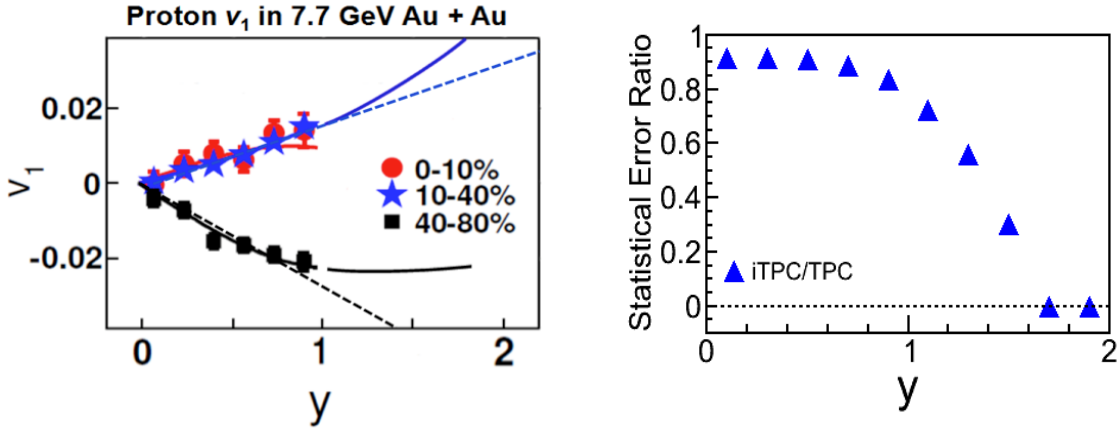


Figure 18: **Left:** Plotted points show measured directed flow  $v_1(y)$  for protons in three centrality bins for Au+Au collisions at  $\sqrt{s_{NN}} = 7.7$  GeV. The solid curves are a cubic fit to the measured data points for intermediate and peripheral centralities while the dashed lines are linear fits. These fits are extrapolated into the rapidity region that will become accessible after the iTPC upgrade. For simplicity, only positive rapidities are plotted here. **Right:** The improvement in statistical errors that would be achieved with the iTPC upgrade, for directed flow measurements at low RHIC energies as a function of rapidity, for any fixed number of events, based on simulations using the UrQMD model. Positive and negative rapidities give the same result, and are averaged in this plot. The two high rapidity points where a zero ratio is plotted correspond to acceptance regions where the present TPC provides no data whatsoever.

The right-hand panel of Figure 18 is based on directed flow calculations using a fixed sample of UrQMD [6] events filtered according to the acceptance and efficiency of the iTPC and the current TPC. Based on these data, we plot the expected ratio of statistical errors before and after the iTPC upgrade. These numbers are highly relevant, given that large statistical errors at the lower beam energies are the main limitation of the measurement already taken in Phase-I of the Beam Energy Scan. The simulations indicate that the plotted ratio is independent of particle species, and is essentially unchanged at the three explored beam energies of  $\sqrt{s_{NN}} = 5, 10$  and 20 GeV. Thus

rapidity is the only relevant observable where the simulations indicate a large variation. The preliminary measurements plotted here are based on the slope of  $v_1(y)$  fitted near mid-rapidity, which captures the overall size of the directed flow signal within the limited rapidity acceptance of the STAR TPC. The broader rapidity acceptance that will be available after the iTPC upgrade, as discussed previously, will allow a more detailed characterization beyond a single slope measurement, and will also provide better statistics even when integrating over rapidity, as is likely to be the case when centrality dependence is being studied at the lowest beam energies.

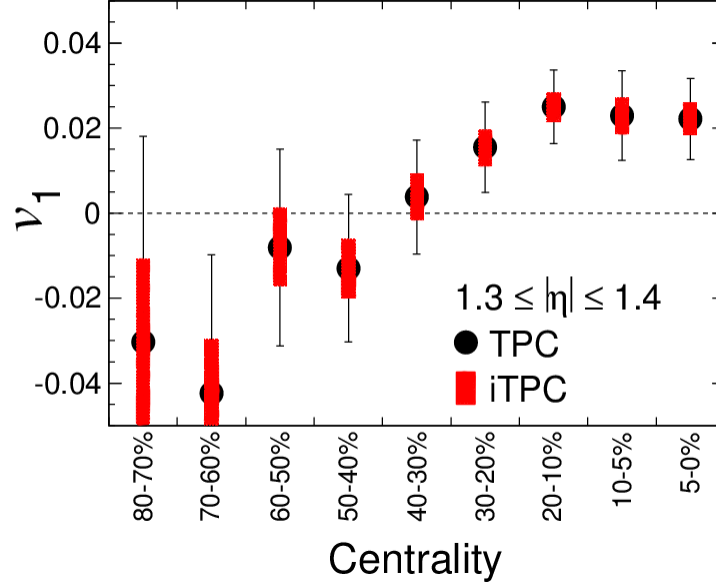


Figure 19: The Forward  $v_1$  measurement as a function of centrality explicitly showing the improvements due to the coverage of the iTPC.

The improved acceptance of the iTPC at low transverse momentum and the improved overall track efficiency will enhance our physics capability in the area of directed flow at BES-II energies. However, a more dramatic enhancement from the iTPC will be the new capability to study directed flow away from midrapidity ( $|y| > 1$ ). Figure 19, based on UrQMD charged particles from 19.6 GeV AuAu collisions, emitted with pseudorapidities from 1.3 to 1.4, shows directed flow as a function of centrality. In this pseudorapidity region, the TPC tracking performance is relatively poor and would drop precipitously if pseudorapidity were further increased, while TPC particle ID capability (based on  $dE/dx$  for a relatively small number of hits per track) is marginal. The red error bars illustrate the much improved statistics furnished by the iTPC for the same sample of events. If  $dE/dx$  were used to isolate a sample of identified tracks, the errors in both scenarios would be magnified, but the TPC errors would be magnified more than those of the iTPC.

### 2.3.2 iTPC-based study of the softening of the Equation of State

A prediction for the width of pion rapidity distributions can be obtained from Landau's hydrodynamic model [9]. In this scenario, the width of the pion rapidity density distributions,  $\sigma_y(\pi^-)$ , depends on the speed of sound,  $c_s$  [10]. A study of  $\sigma_y(\pi^-)/\sigma_y(\text{hydro})$  as a function of beam energy, shows a potentially important feature, namely a minimum

near  $\sqrt{s_{NN}} \sim 8$  GeV – see Figure 20. This feature has been given the name “dale” [11]. It has been argued that this dale structure is linked to a softening of the QCD equation of state [10,11]. With the extended rapidity coverage of the iTPC, STAR will for the first time be in a position to estimate the width (model dependent) of the pion rapidity distribution and thus will be positioned to investigate this proposed softening signature.

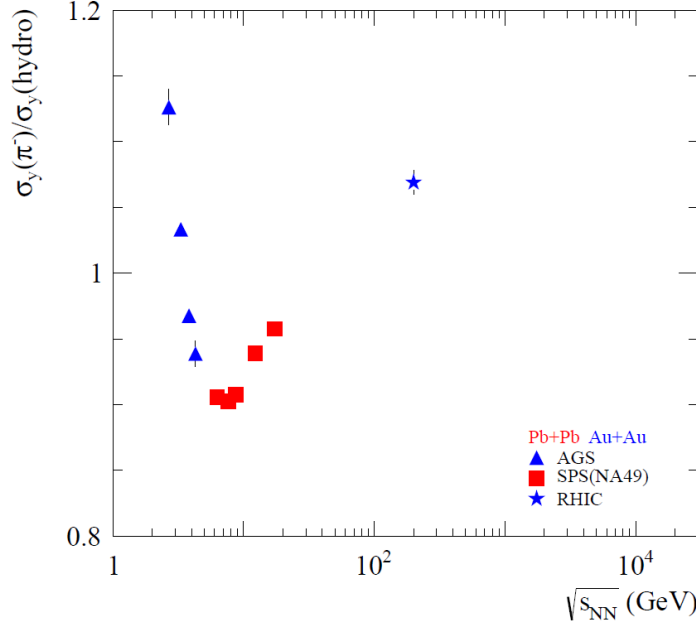


Figure 20: The width of pion rapidity distributions [11], normalized to calculations based on Landau’s hydrodynamic model [9] as a function of beam energy. The minimum may be an indication of the softening of the EoS [10,11]. The only available RHIC measurement to date is at  $\sqrt{s_{NN}} = 200$  GeV, from BRAHMS [12].

### 2.3.3 iTPC-based improvements in establishing the onset of the QGP

Every QGP signature will benefit from extended  $\eta$  coverage, improved  $dE/dx$  and lowered  $p_T$  cut-off. Here we discuss, as an example, the improvement to elliptic flow analysis. Elliptic flow was an intensively studied signature in the analysis of data from BES Phase-I.

There is evidence that a partonic phase is produced in the early stages of Au+Au collisions at top RHIC energies [13,14]. Charting the evolution of the established partonic signatures with  $\sqrt{s_{NN}}$  from 200 to 7.7 GeV should reveal the value of  $\sqrt{s_{NN}}$  where these signatures change or disappear completely. The observation that elliptic flow (expressed by the anisotropy parameter  $v_2$ ) scales with the number of constituent quarks in a given hadron species indicates that the flow is established early in the collision process, when quarks are the relevant degrees of freedom. In contrast, if the flow had been established during a hadronic phase, then the magnitude of  $v_2$  for each hadron species would scale with its mass. In Figure 21, the differences between particle and antiparticle  $v_2$  for the six energies 7.7, 11.5, 19.6, 27, 39, and 62.4 GeV are shown. The result suggests that the constituent quark scaling (NCQ scaling), first observed at  $\sqrt{s_{NN}} = 200$  GeV [15], may no longer hold at lower energies. As the energy is lowered, the violation of NCQ scaling

becomes stronger, and the splitting between mesons and baryons becomes stronger. These observations are consistent with the expectation that the system spends a smaller percentage of the collision duration in the partonic phase as the beam energy is lowered, and that at the lowest BES energies, the system might not reach the QGP phase at all.

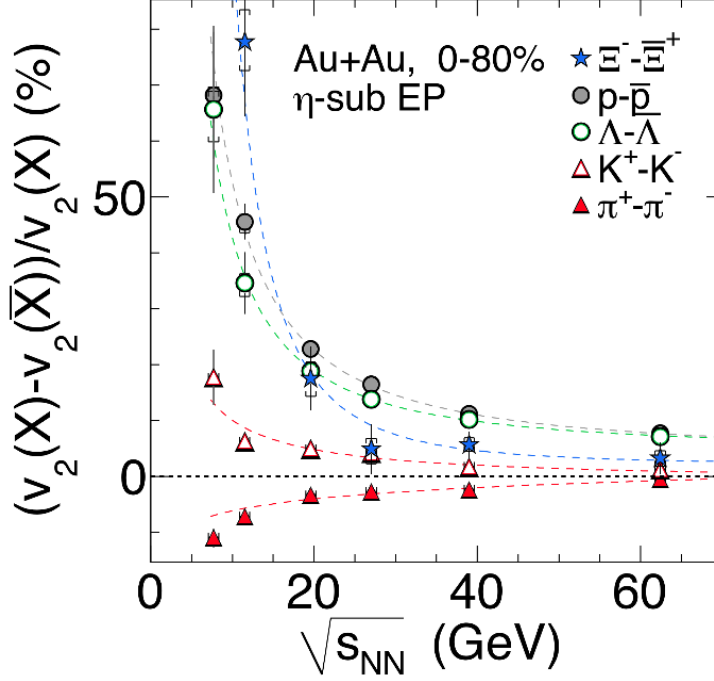


Figure 21: The difference in  $v_2$  between particles and their antiparticles (see legend) as a function of  $\sqrt{s_{NN}}$  for 0-80% central Au+Au collisions. The dashed lines are fits with a power-law function. The error bars depict the combined statistical and systematic errors.

Determination of the event plane (EP), an estimate of the reaction plane, is a crucial requirement in any anisotropic flow analysis. Two different event-plane reconstruction methods were investigated: first, the use of all reconstructed tracks in the TPC (“full TPC” method) and second, the use of only those tracks in the opposite pseudorapidity hemisphere to the track of interest (“ $\eta$ -sub” method). In the full TPC case, self-correlations were avoided by removing the particles of interest from the set of tracks used for the event plane reconstruction. Resonance decays and Hanbury-Brown-Twiss correlations (HBT) with a small  $\Delta\eta$  still contribute to, and bias, the reconstructed EP with this method. To reduce this non-flow effect, the  $\eta$ -sub method was applied with an additional pseudorapidity gap of  $\pm 0.05$ . In general, the  $\eta$ -sub method has a poorer EP resolution compared to the full TPC method, mainly due to having only half the number of tracks for the EP reconstruction. This poorer resolution implies larger corrections to obtain the final  $v_2$  value, and larger errors.



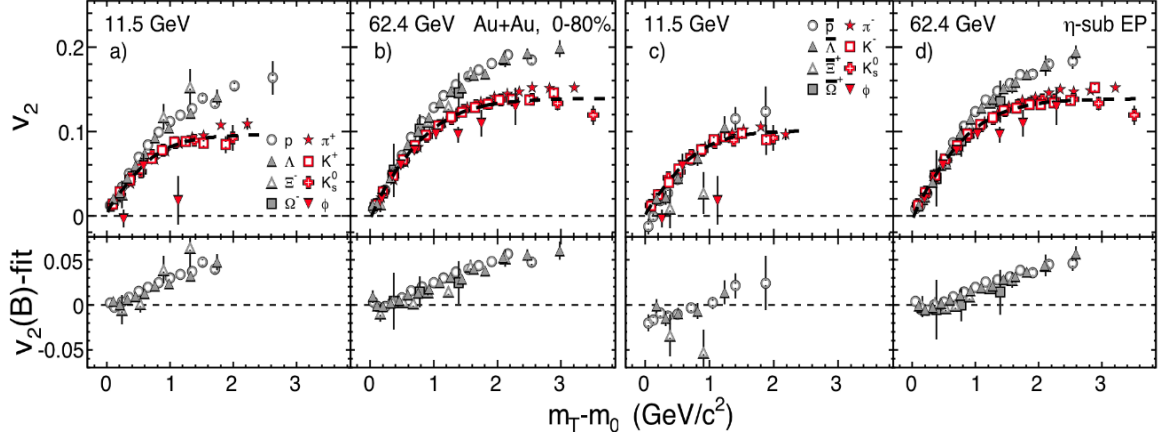


Figure 22: The upper panels depict the elliptic flow,  $v_2$ , as a function of reduced transverse mass,  $m_T - m_0$ , for particles (panels a and b), and for antiparticles (panels c and d), in 0-80% central Au+Au collisions at  $\sqrt{s_{NN}} = 11.5$  and 62.4 GeV. Simultaneous fits to mesons other than pions are shown as dashed lines. The difference between the baryon  $v_2$  and the meson fits are shown in the lower panels.

The large acceptance of the iTPC will have major implications for elliptic flow analysis. It will allow the use of a larger  $\eta$  gap to separate tracks used for EP reconstruction and tracks used in  $v_2$  analysis, and consequently, it will further reduce non-flow, a dominant systematic effect, and simulations indicate that it will improve the EP resolution in the  $\eta$  range  $1 < |\eta| < 2$  by a factor of 2 (see Figure 22). Note that in the convention of the  $v_2$  analysis, the EP resolution represents the fraction of the true signal that is measured; a higher EP resolution is a better measurement. The EP resolution for  $|\eta| < 1$  has the best resolution because it has the largest coverage slice. However, we need to determine the EP outside this window to avoid correlations with the particles of interest.

Figure 23 shows simulated event plane resolutions as a function of the collision centrality for Au+Au collisions at 19.6 GeV using the  $\eta$ -sub method. Within pseudorapidity  $|\eta| < 1$ , a maximum event plane resolution of 40% is reached. This value is reduced to about 14% by using only particles in the pseudorapidity range of  $1 < |\eta| < 2$ , which is necessary in order to suppress non-flow contributions. An improvement of the EP resolution of a factor  $\sim 2$  is observed within this pseudorapidity range by using the iTPC acceptance. This improvement is equivalent to a factor of 4 more statistics, which is important for testing NCQ scaling at high transverse momenta, particularly for rare particles like  $\phi$  and  $\Omega$ .



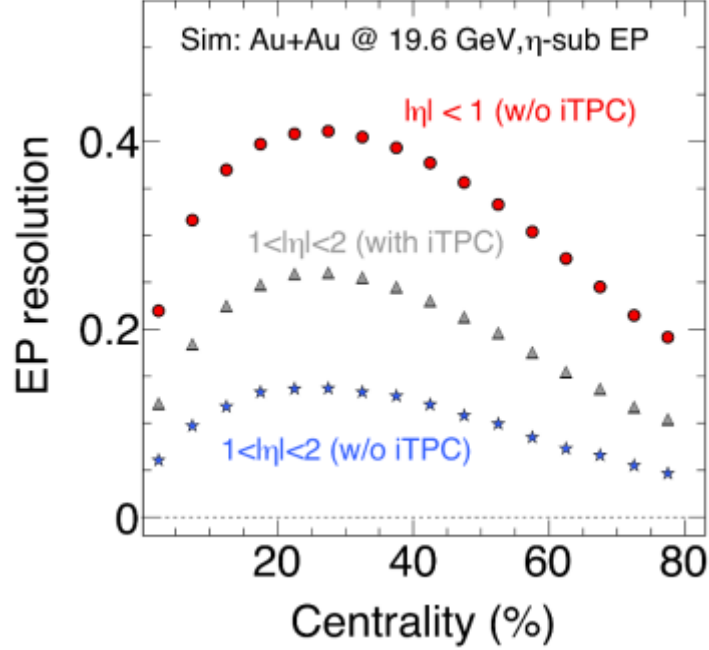


Figure 23: Simulated event plane resolutions as a function of centrality for Au+Au collisions at 19.6 GeV ( $\eta$ -sub method). A factor of  $\sim 2$  improvement is observed in  $1 < |\eta| < 2$  by using the iTPC.

Figure 24 presents  $v_2(p_T)$  at 7.7 and 11.5 GeV for several identified particle types, scaled on both axes by the number of constituent quarks. The phi-meson result is of particular interest in this case, and the solid red circles with error bars illustrate the fact that BES-I statistics for the phi are far less than what is needed to reach a useful physics conclusion at these two beam energies. The height of the red band in the lower part of each panel illustrates the expected error with BES-II statistics and with the enhanced midrapidity acceptance of the iTPC. If BES-II were to take data without the iTPC, the errors would increase by an amount represented by the blue band.

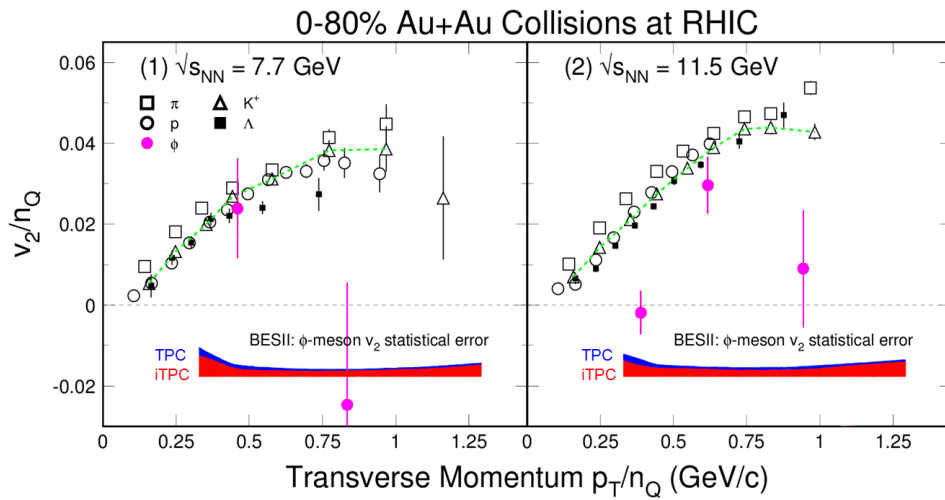


Figure 24: Scaled  $v_2$  of the phi meson showing the projected error bars for BESII with the current TPC (blue band) and with the iTPC (red band).

### 2.3.4 iTPC improvements in determining spectra and freeze-out parameters ( $T$ and $\mu_B$ )

Statistical-thermal models have proven to be very successful in describing particle multiplicities observed in relativistic collisions of heavy ions and elementary particles. These models permit the use of experimental particle yields as input and can generate corresponding thermodynamic parameters such as chemical freeze-out temperature  $T_{\text{ch}}$  and baryon chemical potential  $\mu_B$ . In general, freeze-out parameters are obtained from fits to the experimental measured ratios of produced particles, using the statistical model THERMUS [21,22]. Grand Canonical (GC) and Strangeness Canonical (SC) approaches are used to fit the ratios. In a GC ensemble, the baryon number, strangeness, and electric charge are conserved on average in the system. In the SC approach, strangeness is conserved event-by-event.

The critical region in  $\mu_B$  has been predicted to span on the order of 100 MeV [23], which suggests that the program of measurements in Phase-I of the Beam Energy Scan offers reasonable coverage along the  $\mu_B$  axis from a few tens of MeV up to at least 400 MeV. Furthermore, this interval is predicted to encompass the location of the critical point, if it exists [23]. On the other hand, the Phase-I measurements are subject to basic limitations that strongly motivate a new set of measurements with improved capabilities (*i.e.* lower  $p_T$  acceptance and broader rapidity acceptance), as explained below.

The iTPC upgrade is expected to offer coverage in  $p_T$  down to 60 MeV/ $c$ . This can lead to improvement in the following two ways:

- The extended acceptance at low  $p_T$  reduces the fraction of the yield which must be extrapolated and can allow selection of the correct functional form which best describes the spectrum of each given particle species. Table 2 shows that the added low  $p_T$  coverage will reduce the magnitude of the extrapolation by a factor of two.
- The error on final yields, and hence on freeze-out parameters, will be reduced. Table 2 shows that the uncertainties on the yields are also reduced by a factor of two.

	Low $p_T$ Yield w/o iTPC	Yield error w/o iTPC	Low $p_T$ Yield w/ iTPC	Yield error w/ iTPC
<b>Pion</b>	35%	9%	18%	5%
<b>Kaon</b>	17%	7%	8%	4%
<b>Proton</b>	13%	14%	5%	6%

Table 2: Listed above are the characteristics of the spectra fitting procedure and associated errors, based on current BES-I data at  $\sqrt{s_{\text{NN}}} = 7.7$  GeV. The current extrapolation provides estimates of mid-rapidity yields integrated over all values of  $p_T$ .

Improving the low  $p_T$  coverage also makes possible new physics analyses. A study that is made possible only with the lower  $p_T$  thresholds of the iTPC involves measurement of the effect of the Coulomb acceleration of the pions. The effect is seen as an enhancement of ratio of  $\pi^-/\pi^+$  for  $p_T$  below 100 MeV [24]. By studying the details of the low- $p_T$  pion

spectra, one can determine the Coulomb potential of the source, which is related to the stopping of the protons as these participating protons bring a net positive charge to the interaction region [25]. Also, one can make the best measurement of the primordial pion ratios [25]. Accurate measurements of the pion ratios are important inputs for the statistical models and for fully understanding the thermodynamics of the system. These pion ratios best define the charge (or isospin) chemical potential.

The extended rapidity acceptance coverage with the iTPC will open up the investigation of rapidity dependence of yields and freeze-out parameters. Using model-dependent extrapolations to obtain full phase-space yields, it will become feasible to employ statistical models in an environment where conservation laws can be applied in a less ambiguous way.

Current STAR measurements of freezeout parameters show some deviations from other published data [26], due in part to the fact that the current TPC only offers mid-rapidity coverage. It has been well established that protons have a broader distribution in rapidity than those of mesons or anti-baryons due to partial stopping [27]. As baryon stopping is the key feature in the increase in  $\mu_B$  at lower energies, it is essential to measure the full proton rapidity distributions [28]. Using the iTPC, the proton rapidity density measurements can be made to 1.6 units, which (ignoring spectator protons) accounts for 70% of the proton yield at  $\sqrt{s_{NN}} = 19.6$  GeV. Furthermore, if one also uses vertices displaced in  $z$  from the center of the TPC, one can extend this coverage to 2.3 units of rapidity which encompasses 90% of the protons from the interaction region (see the section on fixed-target measurements). The luminosity increases in BES Phase II will be made possible both with electron cooling and longer bunches. These longer bunches will allow us to trigger on Au+Au collisions offset by up to 200 cm from the center of the TPC. This extended range will allow for almost  $4\pi$  measurements of particle yields, improving constraints on the thermodynamics.

### 2.3.5 *Improvements in the physics reach of the internal fixed-target program*

STAR is developing a fixed-target program using collisions between gold nuclei in one of the circulating beams with an internal gold target. Investigations are underway to determine if it is possible to conduct this fixed-target program concurrently with the regular collider mode of operation by using collisions of off-axis gold nuclei from one beam on the internal gold target. In run-14, a gold foil was installed inside the beam pipe, 2.1 m to the west of the center of STAR, and the first test collisions near  $\sqrt{s_{NN}} = 4$  GeV were collected. Figure 25 (bottom panel) shows the distribution of reconstructed vertices for these events ( $V_Z = 2.1$  m). Data from those collisions are now under analysis. If the tests demonstrate the feasibility of fixed-target running, the result will be a significant expansion of STAR's physics capabilities.

This program complements the proposed BES-II by studying events in which gold ions from the yellow beam are incident upon an internal gold target, thus providing a set of even lower energies and correspondingly higher baryon chemical potentials. The center-of-mass energies available from fixed-target collisions are  $\sqrt{s_{NN}} = 3.0, 3.5, 4.0,$  and  $4.5$

GeV, corresponding to  $\mu_B$  covering the range from 720 – 585 MeV. It is expected that these energies scan a region of the phase diagram where we explore a state of compressed baryonic matter below the onset of deconfinement. The nuclear matter in this region may spend time in a mixed phase, and consequently the physics goals of the fixed-target program focus on evidence for a first-order phase transition through identification of the softest point. The analyses that are expected to have sensitivity in identifying a softening of the EOS are directed flow, integrated elliptic flow, and azimuthally-sensitive HBT.

The main technical challenge of this fixed-target program for STAR arises from the detector being optimized for a collider geometry, while for fixed-target collisions, the center-of-mass is boosted to lab rapidities from 1.05 to 1.52. The fixed target will be installed roughly two meters upstream as shown in the top panel of Figure 25; this means that using the current TPC, we have acceptance for  $0 < \eta < 1.7$ , while the iTPC upgrade will extend this coverage up to  $\eta \sim 2.3$ .

In order to further develop the plans for fixed-target running during BES phase II, an internal gold target was installed inside the vacuum pipe for the 2014 run. Parasitic fixed-target events were recorded during the 14.5 GeV Au+Au run using off-axis ions associated with the gold beams. The bottom panel of Figure 25 shows a schematic of the gold target and the distribution of reconstructed vertices in the vicinity of the target. The shape of the gold target is evident.

The extension of coverage to higher pseudorapidities not only expands the rapidity reach for various particle types, but it also results in a lower  $p_T$  cut-in value at all rapidities. In the case of pions, the width of the  $dN/dy$  distributions is about one unit at the fixed-target energies. The current TPC covers about 55% of the distribution at  $\sqrt{s_{NN}} = 4.5$  GeV, while with the iTPC, this coverage is extended to about 90%. The reduction of the low  $p_T$  cut-in is also important; the current 125 MeV/c cut-in accepts only 60% of pions at mid-rapidity, while the 60 MeV/c cut-in for the iTPC increases this to 85%. Combining these two effects, the current TPC in fixed-target mode has acceptance for only about 30% of all pions, while the iTPC configuration improves this to 75%.

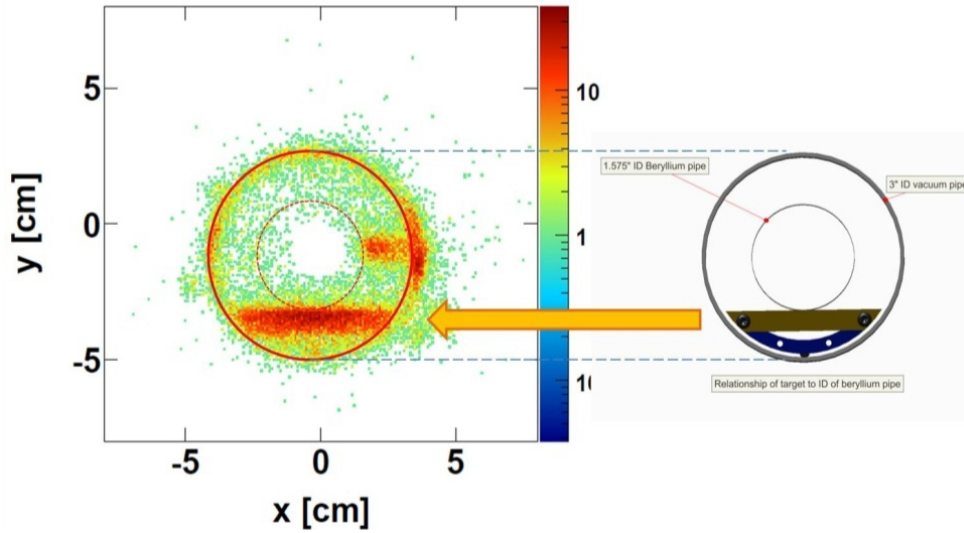
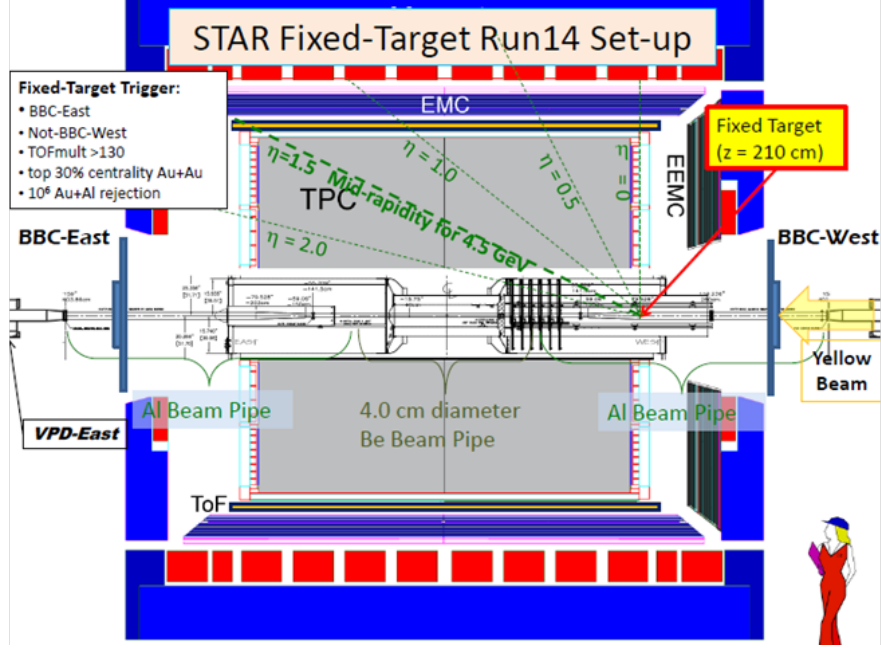


Figure 25: The top panel shows a schematic drawing of STAR showing the location of the fixed target and its  $\eta$  coverage. The bottom panel shows a distribution of reconstructed vertices with  $V_z \sim 211$  cm (bottom left) and a schematic of target as installed in the vacuum pipe (bottom right). The shape of the gold target is clearly evident in the distribution of reconstructed vertices.

In the case of protons, the correspondence between pseudorapidity and rapidity results in low  $p_T$  cut-in values that increase with rapidity. For mid-rapidity, this cut-in value ranges from 400 MeV/c to 800 MeV/c using the current TPC, and from 250 MeV/c to 400 MeV/c for the iTPC. These cut-in values are seen as the cyan and red curves in the lower panel of Figure 26. For the  $\sqrt{s_{NN}} = 4.5$  GeV system, the current TPC accepts only 20% of mid-rapidity protons, while the iTPC increases this to 65%. Overall, the current TPC accepts only about 10% of all protons in fixed-target mode, while the iTPC improves this to 55%.

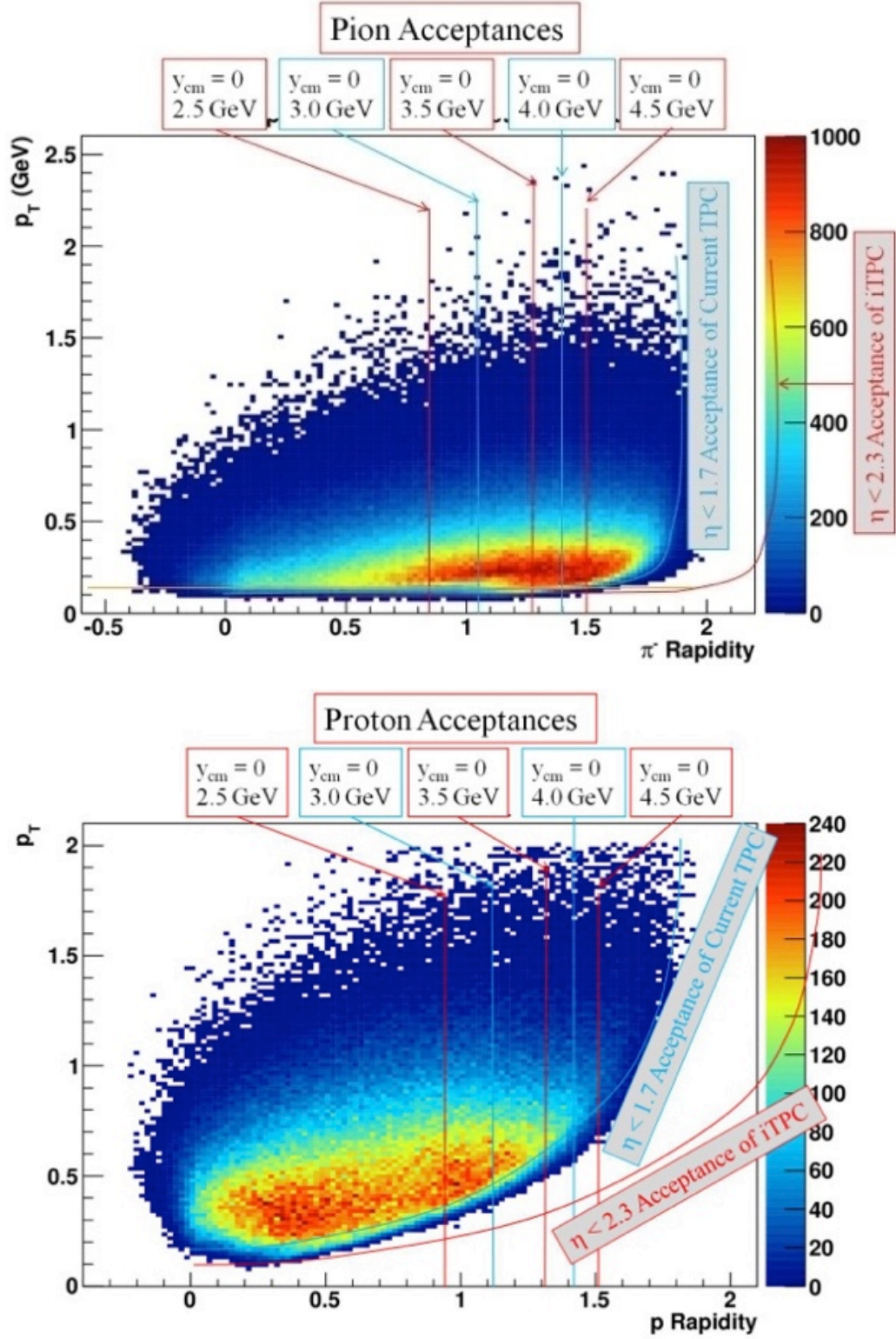


Figure 26: The acceptance for pions (top) and protons (bottom) in fixed-target mode. The histogram is filled with data from Au+Al background events taken during BES-I. The alternating red and cyan vertical bars indicate the center-of-mass rapidity for various energies to be studied. The cyan and red curves indicate the lower acceptance cut-ins for the current TPC and iTPC configurations, respectively.

All three classes of analyses that are a physics focus of the fixed-target program would benefit substantially from the iTPC:

- Azimuthal HBT studies will benefit from the overall 2.5 times increase in pion acceptance. This will reduce the number of events necessary to get a significant physics result by 60%.
- Directed flow studies will have reach in both the forward and backward regions, which allows a cross-check of the results. The detector acceptances and biases will change with rapidity, however if these are corrected properly, the results will be antisymmetric about mid-rapidity.
- Elliptic flow studies will benefit the most from the improved low- $p_T$  acceptance for protons at mid-rapidity. At fixed-target energies, protons make up a major part of the total charged particle yield and it is inferred from extrapolations that their flow pattern is different from that of pions. Having low- $p_T$  coverage and excellent particle identification at mid-rapidity will be essential in understanding the role of mesons and baryons in the development of elliptic flow.

## 2.4 Physics Summary

The iTPC upgrade offers three major benefits for physics analysis: the rapidity coverage is increased, the  $p_T$  thresholds are lowered, and the  $dE/dx$  resolution is improved. These capabilities touch all aspects of the BES program; in some cases, completely new measurements are possible for the first time in STAR, while in other cases, existing physics capabilities are greatly improved. The improved coverage in  $\eta$  and  $p_T$  allow us to better measure particle yields. For the first time in STAR, there will be sufficient  $\eta$  coverage to measure the proton rapidity distributions to the point where they start to fall off, which allows the most direct quantification of baryon stopping. The iTPC will provide sufficient low  $p_T$  coverage to measure the Coulomb effect on the pion distributions, thereby significantly reducing the systematic error in our determination of the thermodynamic properties of the systems. The improved  $\eta$  coverage will significantly improve  $v_1$  measurements, which already point to a possible softening of the equation of state, quantitatively changing what we can learn. Improved  $\eta$  coverage also will allow, and for the first time in STAR, a study of pion rapidity widths, which offers sensitivity to this same physics. The improved  $\eta$  coverage also will provide a two-fold improvement in TPC-based reaction plane resolution, in scenarios where an  $\eta$  gap is used to suppress unwanted correlations unrelated to the reaction plane. Both the improved  $\eta$  and  $p_T$  coverage increase the overall acceptance for the higher moments studies of critical behavior. Without the iTPC, we would have to run for 1.5 to 2.0 times longer to achieve the same sensitivity. The improved  $dE/dx$  resolution reduces hadron contamination of the dielectrons by an order of magnitude. Without the iTPC, this systematic error will be the dominant source of error for our di-lepton studies, which are the major statistics drivers for the BES II program.

## 2.5 References

- [1] STAR Collaboration, BES-II Whitepaper, STAR Note SN-0598 (June 2014).
- [2] D. H. Rischke *et al.*, Heavy Ion Phys. **1**, 309 (1995).
- [3] H. Stoecker, Nucl. Phys. A **750**, 121 (2005).
- [4] J. Brachmann *et al.*, Phys. Rev. C **61**, 024909 (2000).
- [5] L. Adamczyk *et al.* (STAR collaboration), Phys. Rev. Lett. **112**, 162301 (2014).
- [6] S. A. Bass *et al.*, Prog. Part. Nucl. Phys. **41**, 225 (1998),  
M. Bleicher *et al.*, J. Phys. G **25**, 1859 (1999).
- [7] J. Steinheimer *et al.*, Phys. Rev. C **89**, 054913 (2014).
- [8] V. P. Konchakovski *et al.*, Phys. Rev. C **90**, 014903 (2014).
- [9] L. D. Landau, Izv. Akad. Nauk **17**, 51 (1953),  
E. V. Shuryak, Yad. Fiz. **16**, 395 (1972).
- [10] H. Petersen and M. Bleicher, PoS CPOD 2006, 025 (2006) [nucl-th/0611001].
- [11] C. Alt *et al.* (NA49 collaboration), Phys. Rev. C **77**, 024903 (2008),  
A. Rustamov, Cent. Eur. J. Phys. **10**, 1267 (2012).
- [12] I. G. Bearden *et al.* (BRAHMS collaboration), Phys. Rev. Lett. **94**, 162301 (2005),
- [13] I. Arsene *et al.* (BRAHMS Collaboration), Nucl. Phys. A **757**, 1 (2005),  
B. B. Back *et al.* (PHOBOS Collaboration), Nucl. Phys. A **757**, 28 (2005),  
J. Adams *et al.* (STAR Collaboration), Nucl. Phys. A **757**, 102 (2005),  
K. Adcox *et al.* (PHENIX Collaboration), Nucl. Phys. A **757**, 184 (2005).
- [14] S. A. Bass *et al.*, Hot & Dense QCD Matter,  
White Paper submitted to the 2012 Nuclear Science Advisory Committee.
- [15] L. Adamczyk *et al.*, (STAR Collaboration), Phys. Rev. Lett. **110**, 142301 (2013),  
L. Adamczyk *et al.*, (STAR Collaboration), Phys. Rev. C **88**, 014902 (2013).
- [16] Y. Aoki, Z. Fodor, S. D. Katz and K. K. Szabo, Phys. Lett. B **643**, 46 (2006),  
Y. Aoki, G. Endrodi, Z. Fodor, S. D. Katz and K. K. Szabo, Nature **443**, 675 (2006).
- [17] M. A. Stephanov, Phys. Rev. Lett. **102**, 032301 (2009);  
M. Asakawa, S. Ejiri, M. Kitazawa, Phys. Rev. Lett. **103**, 262301 (2009);  
M. A. Stephanov, Phys. Rev. Lett. **107**, 052301 (2011).
- [18] L. Adamczyk *et al.* (STAR collaboration), Phys. Rev. Lett. **112**, 032302 (2014).
- [19] F. Karsch and K. Redlich, Phys. Lett. B **695**, 136 (2011)
- [20] A. Bzdak and V. Koch, Phys. Rev. C **86**, 044904 (2012).
- [21] S. Wheaton, J. Cleymans, and M. Hauer, Comp. Phys. Communications **180**, 84 (2009).
- [22] A. Andronic, P. Braun-Munzinger and J. Stachel, Nucl. Phys. A **834**, 237 (2010).
- [23] R. V. Gavai and S. Gupta, Phys. Rev. D **78**, 114503 (2008);  
R. V. Gavai and S. Gupta, Phys. Rev. D **71**, 114014 (2005);  
S. Gupta, arXiv:0909.4630;  
M. Asakawa *et al.*, Phys. Rev. Lett. **101**, 122302 (2008);  
P. Costa *et al.*, Europhys. Lett. **86**, 31001 (2009);  
P. Costa *et al.*, Phys. Lett. B **647**, 431 (2007).
- [24] B. I. Abelev *et al.* (STAR Collaboration), Phys. Rev. C **79**, 034909 (2009);  
L. Ahle *et al.* (E866 and E917 Collaborations), Phys. Lett. **B476**, 1 (2000);  
J. L. Klay *et al.* (E895 Collaboration) Phys. Rev. C **68**, 054905 (2003);  
A. Wagner *et al.* (KaoS Collaboration), Phys. Lett. **B420**, 20 (1998);  
C. Alt *et al.* (NA49 Collaboration), Phys. Rev. C **77**, 024903 (2008);  
D. Pelte *et al.* (FOPI Collaboration), Z. Phys. **A357**, 215 (1997);  
H. Boggild *et al.* (NA44 Collaboration), Phys. Lett. **B372**, 339 (1996);  
F. Retiere *et al.* (WA98 Collaboration), Nucl. Phys. **A681**, 149c (2001).
- [25] D. Cebra *et al.*, submitted to Phys. Rev. C (2014) [arXiv:1408.1369]



- [26] L. Kumar (STAR Collaboration), Nucl. Phys. **A904-905**, 256c (2013).
- [27] T. Anticic et al. (NA49 Collaboration), Phys. Rev. C **83**, 014901 (2011).
- [28] J. Cleymans, J. Phys. G; Nucl. Part. Phys. **37**, 094015 (2010)
- [29] R. Rapp, Phys. Rev. C **63**, 054907 (2001).
- [30] L. Adamczyk et al., arXiv: 1501.05341.
- [31] O. Linnyk et al., Phys. Rev. C **84**, 054917 (2011).
- [32] O. Linnyk et al., Phys. Rev. C **85**, 024910 (2012).
- [33] R. Rapp, Phys. Rev. C **63**, 054907 (2001).
- [34] H. van Hees and R. Rapp, Phys. Rev. Lett. **97**, 102301 (2006).
- [35] H. van Hees and R. Rapp, Nucl. Phys. A **806**, 339 (2008).
- [36] R. Rapp, Adv. High Energy Phys. **2013** (2013) 148253.
- [37] R. Rapp and H. van Hees, arXiv: 1411.4612
- [38] M.A. Stephanov, private communication: [https://drupal.star.bnl.gov/STAR/starnotes/public/sn0619](https://drupal.star.bnl.gov/STAR/starnotes/public/sn0619/delta-y-rt.pdf)  
(delta-y-rt.pdf)
- [39] M.A. Stephanov M. A. Stephanov, Prog. Theor. Phys. Suppl. **153**, 139 (2004) [Int. J. Mod. Phys. A **20**, 4387 (2005)] [hep-ph/0402115]

### 3 Introduction to the STAR TPC - Hardware

#### 3.1 The Proposed Upgrade

The STAR TPC has played a central role in the RHIC physics program for over 15 years. It has enabled a wide range of new discoveries and explored a wealth of new physics topics. In fact, the event display for the STAR TPC, showing a Au+Au collision at RHIC (cover page), is one of the iconic pictures for the High Energy Nuclear Physics program.

The performance of the TPC remains close to the original design requirements in terms of tracking efficiency, momentum resolution, and energy loss measurements [1,2]. However, we propose to upgrade the STAR TPC so that the inner sectors will have complete hermetic coverage with improved  $dE/dx$  measurements and better tracking performance. The upgrade will require new readout electronics to match the increased number of channels in the inner sectors. The upgrade project will also replace the wire grids in the MWPCs so they can be run at lower gain and utilize larger pads.

We propose to keep the outer sectors as they are (i.e. no changes) since they are already fully instrumented and have less integrated charge deposition and less potential aging effects than the inner sectors.

Unlike the outer TPC sectors, the current inner TPC pad row geometry does not provide hermetic coverage at all radii. The inner pad rows are 11.5 mm tall yet the spacing between rows is variable but always greater than 50 mm, resulting in “missing rows”. Therefore, only 20% of the path length of a charged particles path traversing an inner sector of the TPC is sampled by the current padplane and electronics readout. The project presented in this technical design report will double the number of pads in the inner sectors and increase the sampled path length of tracks passing over the pads to 95%.

The new pad planes and wire grids will increase the acceptance of the TPC and this will allow STAR to pursue an enhanced physics program in the Beam Energy Scan II program and beyond.

In addition to the highlights mentioned in Chapter 2 for the physics impact of the iTPC, the upgrade will also improve the tracking efficiency of the TPC at low momentum. We estimate that the upgrade will increase the efficiency for strange hadron reconstruction (e.g.  $\Xi$ ,  $\Omega$  and  $\phi$ ) by an order of magnitude for  $p_T < 1$  GeV/ $c$ , which is a crucial momentum range for extraction of yields and for a detailed study of hydrodynamic flow. The improved  $dE/dx$  resolution and efficiency for low momentum tracks also allows better selection of electron candidates from thermal radiation and in-medium vector meson decays. Simulations show that hadron contamination can be greatly reduced with the upgrade, and a two-fold improvement in electron selection is possible with enhanced  $dE/dx$  resolution. This, together with the increased luminosity from the accelerator, is ideal for systematically mapping out the temperature dependence of the in-medium  $\rho$  mass spectral shape and its transition to thermal radiation from the partonic phase. The  $\rho$

mass spectral shape is an important indicator of the degree of chiral symmetry restoration in a heavy ion collision

The iTPC upgrade also enhances STAR's physics capability at top RHIC energies. The improved  $dE/dx$  resolution allows better separation of charged kaons and protons at high momentum. Measurements of identified particles related to the fragmentation function from jets at RHIC energies provide unique insights into the jet-medium interaction and into the different quark and gluon energy loss mechanisms in a strongly interacting QGP since the quark and gluon contributions to the leading hadrons in the accessible momentum range change rapidly at RHIC energies. The iTPC upgrade also provides much-needed rapidity coverage to study the impact on hydrodynamic evolution which is governed by the initial conditions of the incoming nuclear matter and associated fluctuations in geometry. Recently developed tools using higher harmonics of flow and rapidity correlations have improved our understanding of non-equilibrium evolution from highly saturated gluons. The increased coverage of the iTPC will significantly enhance the long-range ridge correlation measurements with large pseudorapidity gap. We also note that the iTPC upgrade will provide improved rapidity coverage and particle identification for studying hyperon ( $\Lambda$ ) polarization at higher rapidity and momentum, a possible unique tool to access strange quark spin structure in the proton. The enhanced reconstruction of multi-strange hyperons also improves the sensitivity to exotic multi-strange states ( $H$  di-baryon,  $\Xi$ - $\Xi$  states, and di- $\Omega$ ).

### 3.2 TPC design and configuration

The STAR detector uses a TPC as its primary tracking device [3]. The TPC records the tracks of particles, measures their momenta in a 0.5 T magnetic field, and identifies the particles by measuring their ionization energy loss ( $dE/dx$ ). Its acceptance covers 2.0 units of pseudorapidity over the full azimuth. Particles are identified over a momentum range from 100 MeV/c to greater than 1 GeV/c, and momenta are measured over a range of 100 MeV/c to 30 GeV/c.

The STAR TPC is shown schematically in Figure 27. It sits in a large solenoid magnet that can operate up to 0.5 T field. The TPC is 4.2 m long and 4 m in diameter. It is a cylindrical volume of gas with an enclosed electric field cage that provides a uniform electric field of 133 V/cm. The path of a primary ionizing particle passing through the gas volume is reconstructed from the secondary electrons which are created by the primary particle interacting with the gas. The secondary electrons drift to one end of the chamber and their position is recorded by Multi-Wire Proportional Chambers (MWPCs) with padplane readout. The uniform electric field which is required to drift the electrons inside the TPC is defined by a thin conductive Central Membrane (CM) at the center of the TPC and a concentric field cage leading to both ends of the TPC. Good electric field uniformity is critical since track reconstruction precision is sub-millimeter and electron drift paths are up to 2.1 meters.

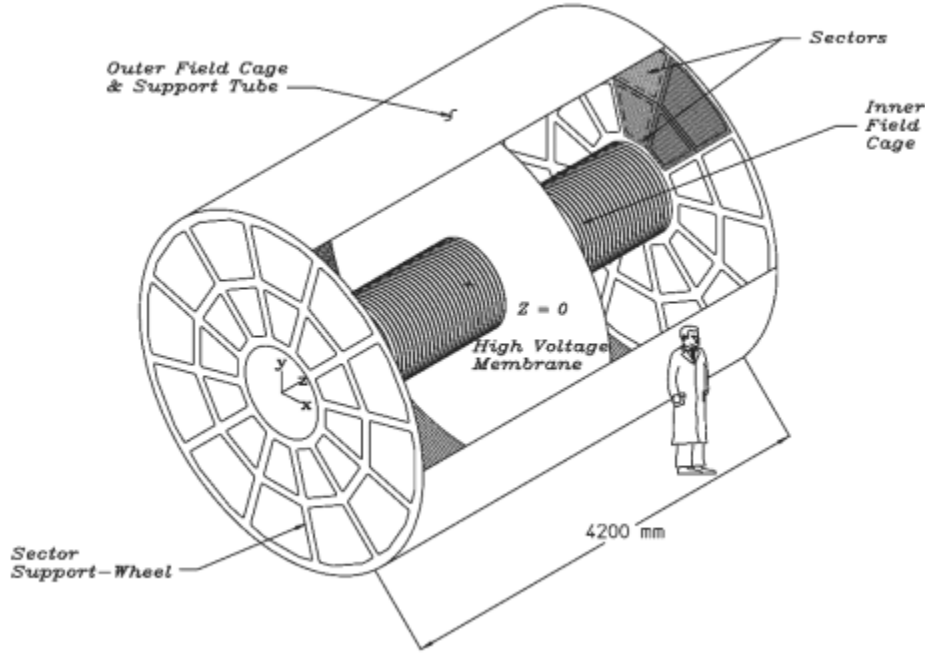


Figure 27: A schematic view of the STAR TPC. Secondary electrons drift away from the high voltage membrane, at the center, towards readout planes at either end of the TPC.

At the readout plane, the drifting electrons encounter a grid of  $20\ \mu\text{m}$  anode wires. The arriving electrons create an avalanche of charge in the high field region near the anode wires and the positive ions created in the avalanche induce a temporary image charge on the padplane which lie beneath the anode wires. The image charge is measured by a preamplifier/shaper/waveform digitizer system. The induced charge from an avalanche is shared over several adjacent pads, so the original track position can be reconstructed to a small fraction of a pad width. There are a total of 136,560 pads in the old readout system. There will be 175,440 pads in the new inner and outer sectors, combined.

The TPC is filled with P10 gas (10% methane, 90% argon) and regulated at 2 mbar above the ambient atmospheric pressure to allow for an efficient feedback loop for regulation of the pressure inside the TPC and to prevent oxygen from diffusing into the TPC through small leaks in the containment vessel. P10 is a good gas to use in a TPC because it has a relatively fast drift velocity which peaks at a low electric field strength. Operating at the peak of the drift velocity curve makes the drift velocity stable and insensitive to small variations in temperature and pressure and the low voltage greatly simplifies the field cage design.

The design requirements for the TPC are guided by the properties of the P10 gas and are constrained by cost-based limits on the size of pads and channel count. For example, diffusion of the drifting electrons and the statistics of their small numbers defines the position resolution of the TPC while ionization fluctuations and finite track length determine the  $dE/dx$  resolution for particle identification. The original design specifications were adjusted accordingly to limit cost and complexity without seriously compromising the potential for tracking precision and particle identification.

Note that the inner and outer sector padplanes are different as a result of the physical and cost-based constraints imposed on the original design project. For example, the outer sector readout pads are arranged on a rectangular grid with a pitch of 6.7 mm along the wires and 20.0 mm perpendicular to the wires. There is a 0.5 mm isolation gap between pads in both directions. See Figure 28. The grid of pads for the outer sectors is phase locked with the anode wires so that five wires cross over each pad row. The 6.7 mm pitch and the 4 mm distance between the anodes and the padplane creates a readout system that is consistent with the transverse diffusion width of the electron cloud. More explicitly, the width of the induced surface charge from an avalanche near an anode wire is nearly the same as the diffusion width for tracks that drift from the central membrane of the TPC (2 m). Thus a pad pitch of 6.7 mm, combined with an anode to padplane spacing of 4 mm, places most of the signal on 3 pads which gives good centroid determination at minimum gas gain. Overall, the outer sector configuration gives good signal to noise without seriously compromising two-track resolution.

The (old) inner sector pads have a pitch of 3.35 mm along the direction of the wires and 12 mm perpendicular to the wires. There is a 0.5 mm isolation gap between the pads in both directions. Three wires are phase locked with the pads and cross over each inner pad row; but the inner anode wires are closer to the padplane (2 mm) and so an avalanche near an anode wire places most of the signal on 4 or more pads.

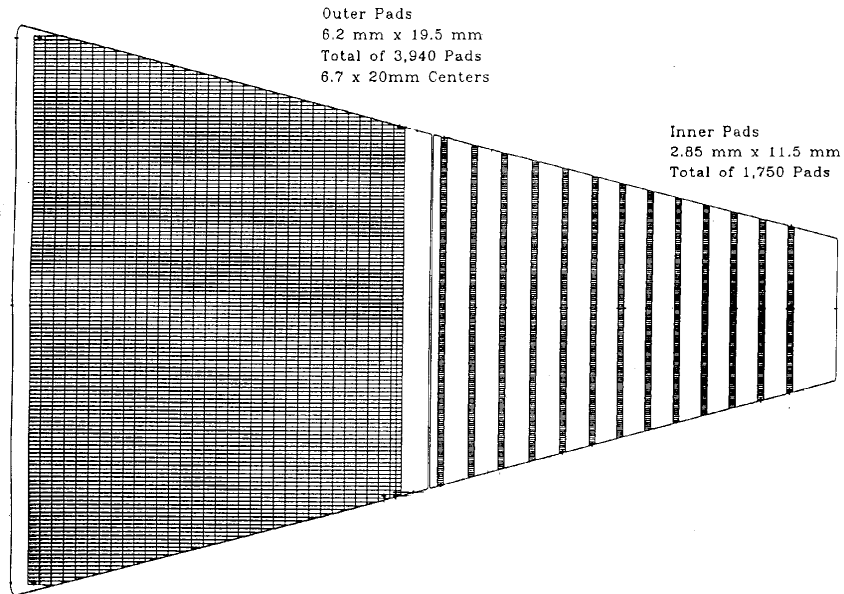


Figure 28: Configuration of the existing pad rows in a STAR TPC padplane super-sector (one inner sector and one outer sector). Note that the outer sector padplane coverage is complete but the inner sector pad rows do not cover the full area of the inner sector.

When the TPC was designed in 1993-1995, we did not know the multiplicity of particles emerging from a RHIC collision at 200 GeV. So, the inner sectors were designed with smaller pads to help relieve track merging at small radii in case of very high multiplicity events. Also, as an optional choice in order to take advantage of the smaller pad sizes,

the TPC was designed so it could be operated with He-Ethane gas due to the lower diffusion rate in He-Ethane. Experience has shown that this is not necessary.

Nonetheless, the inner sub-sectors are in the region of highest track density and thus were optimized for good two-hit resolution. The reduction of the induced surface charge width to less than the electron cloud diffusion width in P10 improves the two-track resolution for stiff tracks at  $\eta \approx 0$ . The main improvement in two-track resolution, however, is due to shorter pad length (12 mm instead of 20 mm). This is important for lower momentum tracks which cross the pad rows at angles far from perpendicular and for tracks with a large dip angle. The short pads give shorter projective widths in the  $r$ - $\phi$  direction (the direction along the pad row), and the  $z$  direction (the drift direction) for these angled tracks.

The compromise that is required, because we used smaller pads on the inner sector, is the use of separated pad rows instead of continuous pad coverage. This constraint was imposed by the cost and the available packing density of the front end electronics channels when the TPC was designed and built. The loss of pad rows means that the inner sectors serve to extend the position measurements along the tracks to small radii (thus improving the momentum resolution and the matching to the inner tracking detectors) but does not contribute significantly to improving the  $dE/dx$  resolution measurements for the tracks.

The purpose of the iTPC upgrade project is to maintain the excellent two-track resolution of the inner sectors but to improve the  $dE/dx$  resolution for all tracks while increasing the acceptance of the detector, most especially for tracks at high rapidity.

In summary, the segmentation on the inner sectors was determined by the economics of the 1990s. It is now possible to populate the entire inner sector with pads and electronics at a reasonable cost.

### 3.3 Additional Performance Issues

In the following subsections, we discuss two issues that profoundly affect TPC performance: distortion and aging.

#### 3.3.1 *Distortions*

The position of a secondary electron at the padplane can be distorted by non-uniformities and global misalignments in the electric and magnetic fields of the TPC. The non-uniformities in the fields lead to a non-uniform drift of the electrons from the point of origin to the padplane. In the STAR TPC, the electric and magnetic fields are parallel and nearly uniform in  $r$  and  $z$ . The deviations from these ideal conditions are small and a typical distortion along the pad row is  $\leq 1$  cm before applying corrections. The exception to this rule is the distortion due to space charge in the TPC and this can lead to distortions along the pad rows of several centimeters (up to 10 cm) at RHIC II luminosities.

Centimeter-scale distortions in the direction transverse to the path of a particle are important because they affect the transverse momentum determination for particles at high  $p_T$ . In order to understand these distortions, and correct for them, the magnetic field was carefully mapped with Hall probes and an NMR probe before the TPC was installed in the magnet. It was not possible to measure the electric fields and so we calculated them from the known geometry, and known imperfections, of the TPC. With the fields known, we correct the hit positions along the pad rows, using a set of distortion equations for nearly parallel electric and magnetic fields, in order to calculate the original track parameters. We are typically able to do these corrections to  $\sim 1$  or  $2\%$  precision and so the systematic error in these corrections is important when they become larger than the hit point resolution of the TPC ( $\sim 500\text{ }\mu\text{m}$ ).

A careful study of the residuals for TPC cluster positions with respect to the track position revealed that an unanticipated source of distortion is also present in the TPC data. A discontinuity in the residuals at the boundary between the inner and outer readout chambers of the TPC is consistent with incomplete blockage of ion backflow by the gated grid at the gap.

This is entirely possible because the gated grid does not cover the full area between the inner and outer sectors; there is a small gap ( $\sim 16\text{ mm}$  wide) between the end of one grid and the start of the other. This allows a sheet of ions created near the anode wires to flow out of the gap and to travel across the TPC gas volume towards the central membrane (cathode). The presence of this sheet of charge distorts the path of the secondary electrons which are drifting in the opposite direction. See Figure 29.

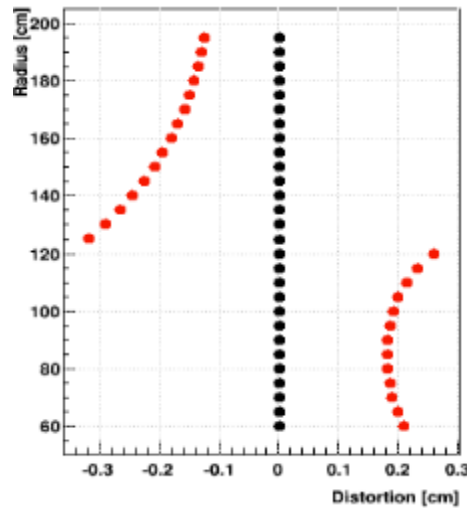


Figure 29: Distortions at the junction between the inner and outer gated grids. The vertical axis (cm) shows the position of a pad row (indicated by dots) in the radial direction. The horizontal axis is in millimeters. The black dots show the expected hit pattern for an infinite momentum track. The red dots show the observed hit pattern due to charge leaking out of the gap between the inner and outer gated grids.

One of the goals of the iTPC upgrade project is to eliminate the gap in the gated grid coverage so that positive ions cannot leak out. As will be discussed in a later section of this technical design report, we can eliminate a portion of the gap -- that which is due to the mechanical construction of the inner sectors. We will not remove or modify the outer

sectors and so the portion of the gap that is due to the outer sector construction cannot be eliminated.

### 3.3.2 *Aging: an issue for the TPC in the high luminosity era at RHIC*

In 2009, STAR conducted an external review to assess the ability of the TPC to meet the requirements of the experimental program during the high luminosity era at RHIC (RHIC-II). The review was chaired by Dr. Ron Settles (MPI Munich) and the full report is available on the web [4].

The review panel was asked to review the evidence for aging on the TPC anode wires and to recommend possible solutions if the anode wires are, in fact, reaching their end of life. The reason for concern was that high luminosity running of p-p 500 GeV beams was causing the anode wires on the inner sectors to break down and trip off due to excessive current drawn from the power supplies.

One possible explanation for the observed breakdown behavior is the well documented phenomenon called “aging”. It is believed that aging is due to hydrocarbon build up on the anode wires, over time, which creates irregular deposits on the wires. The rate of aging is proportional to the accumulated charge collected by the anode wires.

The Malter effect is another possible explanation for the observed high voltage breakdown that has been seen in the inner sectors when running high intensity beams. The Malter effect is caused by a buildup of insulating compounds on the cathode wires and is less well understood and less predictable than the aging of the anodes.

The review committee was not able to reach any firm conclusions regarding whether aging or the Malter effect is responsible for the breakdown in the inner sectors; but they did recommend that we lower the voltage on the anode wires to reduce the gain in the MWPCs. They also recommended replacing the MWPCs at some future date to ensure the long term viability of the STAR physics program.

So, since 2009, the STAR TPC has been operating with the inner sectors at 40% of their nominal gain settings. Several years of experience has shown that the tracking performance of the inner sectors is still good (hits and clusters are still recorded with reasonable efficiency) but the  $dE/dx$  resolution is worse. It is difficult to quantify the impact of the gain change on  $dE/dx$  because the original inner sectors were not optimized for  $dE/dx$  resolution but the  $dE/dx$  performance will certainly be better for the upgraded iTPC sectors. Our goal is to provide good  $dE/dx$  resolution and better tracking ... especially for high rapidity tracks which only cross over the inner pad rows.

## 3.4 References

- [1] STAR Conceptual Design Report, STAR Note SN0499.
- [2] STAR CDR Update, <http://www.star.bnl.gov/public/tpc/notebooks/CDRUpdate.pdf>
- [3] STAR TPC NIM, M. Anderson et al., Nucl. Instrum. Meth. A 499, 659 (2003).
- [4] [http://www.bnl.gov/npp/docs/RHICst09\\_notes/ReportoftheSTARTPCReviewCommittee2009.pdf](http://www.bnl.gov/npp/docs/RHICst09_notes/ReportoftheSTARTPCReviewCommittee2009.pdf)



## 4 Simulations with a new Pad Plane & MWPCs

### 4.1 Padplane Design Study

A detailed study of the new iTPC design has been carried out using the STAR simulation framework. The goal was to demonstrate the impact of the upgrade upon the physics measurements and to justify the proposed upgrade. The simulation studies are also important to help optimize the design of the new detector. Several key aspects of the simulation studies are discussed in this chapter.

For these simulation studies we used the HIJING Monte Carlo event generator [3] to simulate the Au+Au collisions at  $\sqrt{s_{NN}} = 200$  GeV energies. The simulated data was then passed on to the GEANT simulation package for detector simulations. At this point the hits in the active volume of the TPC were produced for several different pad geometry configurations and finally the outcome of the detector simulation was put through the STAR TPC response simulation (TpcRS) algorithms.

The most immediate consequence of increasing the number of inner padrows is the larger acceptance of the TPC. The current configuration has 13 widely spaced pad rows. Configurations with 32, 40 and 52 pad rows have been considered for the new design. The track quality requirement for the STAR experiment requires at least 15 hits in the TPC, therefore high pseudorapidity tracks that only traverse 13 rows of the current inner TPC are, by definition, disregarded. This quality cut has a profound effect on the measured yield of low transverse momentum  $p_T$  particles which are confined to small radii due to the high magnetic field. Therefore, increasing the number of pad rows in the inner section of the TPC is expected to increase the acceptance for low  $p_T$  particle tracks.

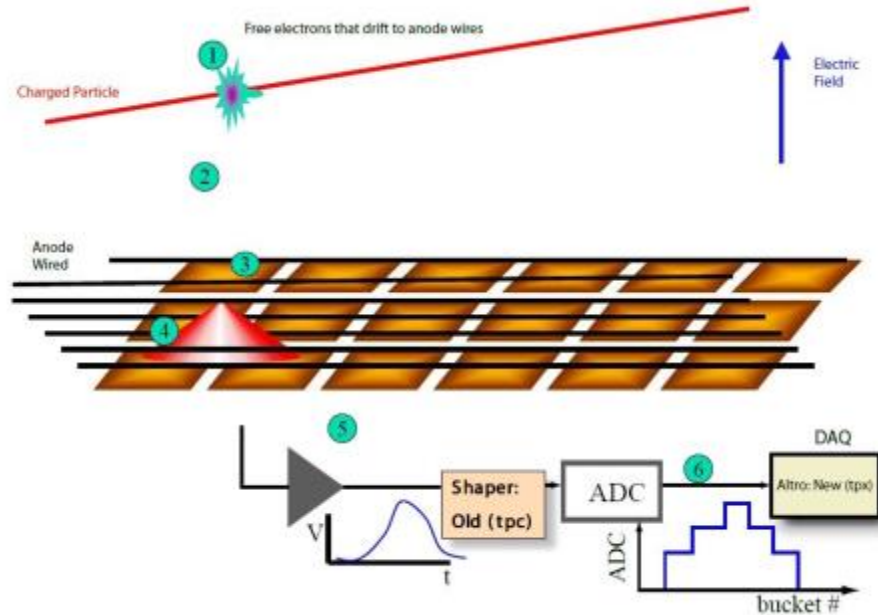


Figure 30: Schematic view of the TPC response simulator flow chart.

A detailed simulation is important to demonstrate the robustness and correctness of the procedure. TpcRS was used to perform the detailed simulations of the TPC performance and response. The workflow of the TpcRS flow is shown in Figure 30 and can be described in 6 basic steps (steps are labeled with numbered circles)

The first step is to generate the free electrons from the GEANT hits in the active volume of the TPC. It is based on the Bichsel's particle identification model for the time projection chambers [1]. The number of primary clusters is calculated as:

$$\frac{1}{\lambda} = \frac{dN}{dx}(\beta\gamma)$$

which for Ar gas results is about 28 free primary electrons per centimeter. The kinetic energy for each primary electron is derived from the  $dN/dE$  distribution. The average number of secondary electrons produced for each primary is given by:

$$n_0 = \frac{(E - I_0)(1 - F)}{W}$$

where  $I_0 = 13.1$  eV is the average minimum energy of ionization for the TPC gas,  $W = 28.5$  eV is the average ionization potential of the gas and  $F = 0.3$  is the Fano factor. The total number of electrons per primary electron is then expressed as:

$$N = 1 + \text{Binomial}(n_0, p = 1 - F)$$

The next step is to properly describe the drift of the free electrons to the padplane in the presence of electric and magnetic fields. Note that even in the ideal case of uniform and parallel electric and magnetic fields the electrons will still be deflected from straight line trajectories due to the diffusion. The transverse diffusion factor is given by:

$$\sigma_T = \sigma_{T0}(B)\sqrt{L_D}$$

where  $B = 5$  kG,  $L$  is the drift length,  $\sigma_{T0}(5 \text{ kG}) = 230 \text{ } \mu\text{m}/\sqrt{\text{cm}}$

In the third step of the simulation, the transport of electrons near the wire planes is performed. At this point the effect of imperfect electric and magnetic fields has to be taken into account. This introduces the Lorentz shift along the wires of about  $1 \text{ mm} \times \tan \Theta_L$ , where  $\tan \Theta_L = \omega\tau$  ( $\sim 2$ )

Once the electrons are transported all the way to the MWPCs, a careful simulation of the charge distribution in the wire chambers and the time development of the signal is necessary. The basic formulas and parameters for the calculations done in TpcRS are taken from [2]. Finally, the TpcRS does the signal digitization before the tail cancellation algorithms are applied.

The main descriptors of the reconstructed events, using the upgraded iTPC geometry and new TpcRS are shown in Figure 31 to demonstrate that the simulation is well understood and produces the expected results.

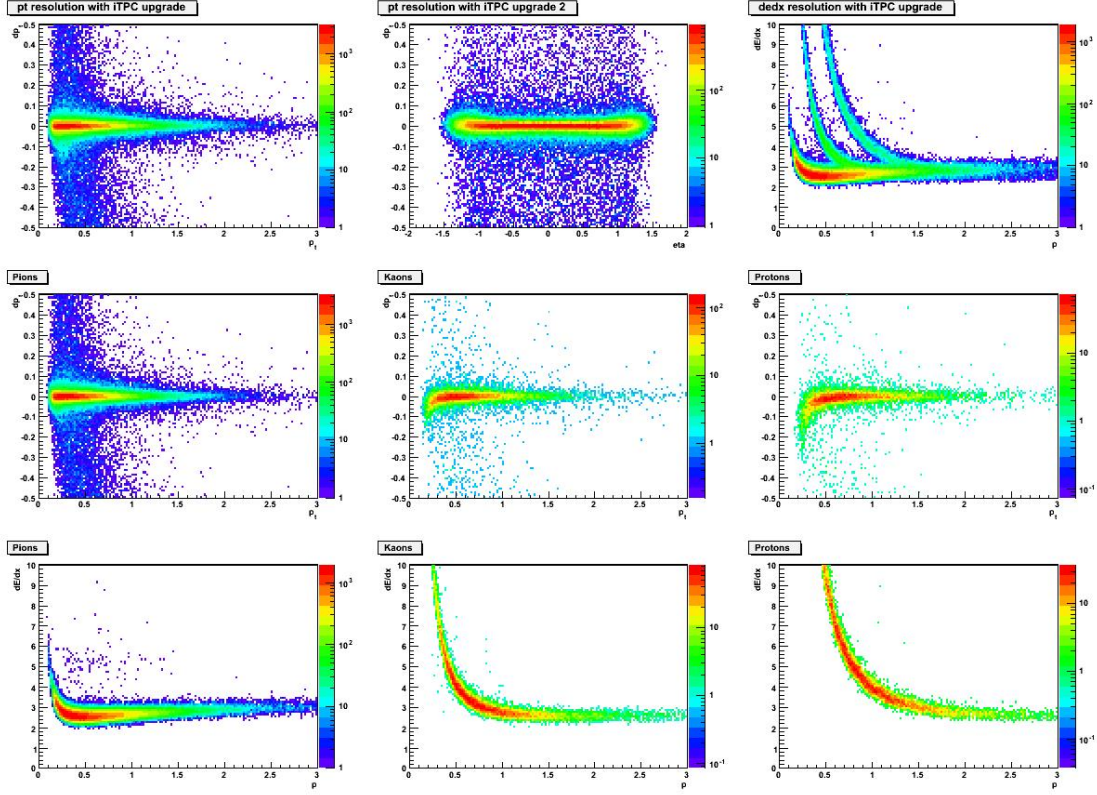


Figure 31: Characteristics of the reconstructed events simulated with the new iTPC geometry.

Detector simulations were performed for several different iTPC geometries and configurations. Table 3 shows the specifications for several different padplane geometries which were investigated.

Geometry	devTA	devTB	devTC	devTD	devTE	devTF	y2011
# of Padrows	32	40	40	32	50	32	13
Pad Size[cm×cm]	0.67×2.0	0.67×1.6	0.5×1.6	0.5×2.0	0.335×1.28	0.4×2.0	0.335×1.15
# of Channels	2162	2572	3496	2762	6494	3456	1750

Table 3: Description of different iTPC padplane geometries

Momentum resolution for each design has been studied. The resolution of the measurement is a function of momentum and could be given in the following form:

$$\left(\frac{\sigma_{p_T}}{p_T}\right)^2 = (\sigma_{res})^2 + (\sigma_{ms})^2; \sigma_{res} = p_0; \sigma_{res} = p_1 \times p_T,$$

where  $\sigma_{ms}$  is the error due to a multiple scattering and  $\sigma_{res}$  is the error of our measurement. Figure 32 shows the resolution as a function of the momentum with a linear fit.

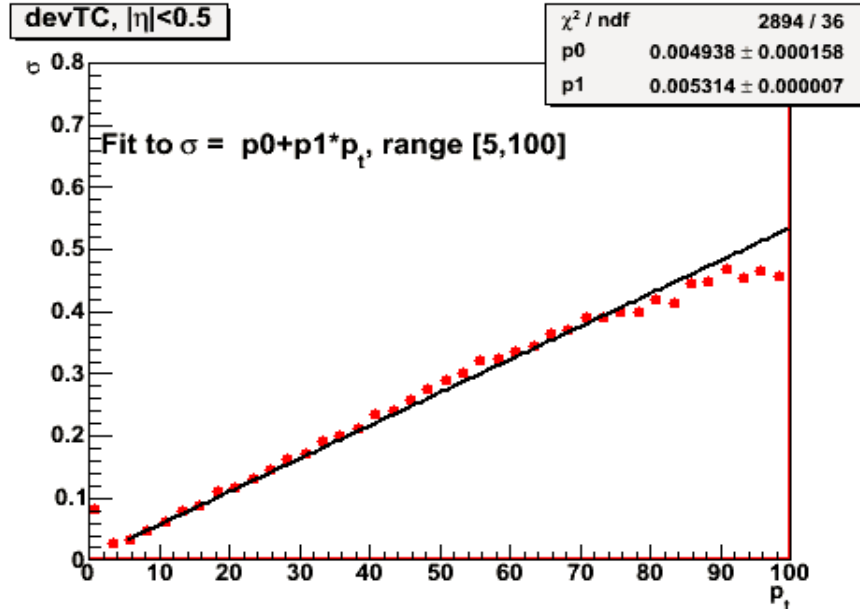


Figure 32: Momentum resolution as a function of the transverse momentum to extract the  $p_1$  value.

Figure 33 shows the momentum measurement resolution coefficient with for the track momentum reconstruction for several different padplane configurations. Note that the results are shown in three pseudorapidity regions (circles, triangle and squares). The figure illustrates that increasing the number of pads by about a factor of two results in a better resolution compared to the original TPC padplane geometry with 13 pad rows. The resolution improvement is especially noticeable in the pseudorapidity region  $1 < |\eta| < 1.5$ , where the resultant resolution is about a factor of two higher. The configurations with higher pad density of up to a factor of four increase in the number of pads, yield only slightly better results compared to the factor of two increase.

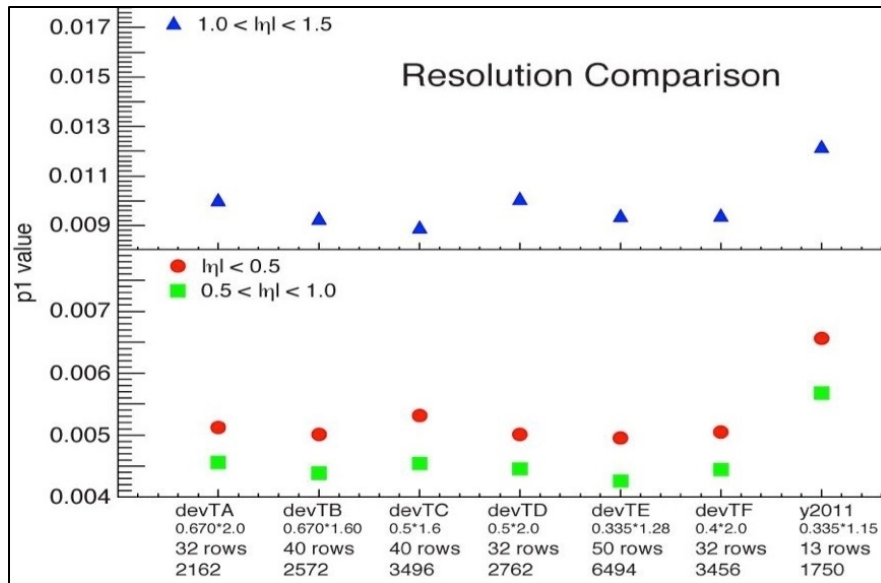


Figure 33: Track resolution (linear component) for different geometries of the inner part of the time projection chamber.

The efficiency for pion, kaon, and proton track reconstruction are shown in Figure 34. The blue curves show the results for the current geometry while the *devTC* geometry results are shown in red.

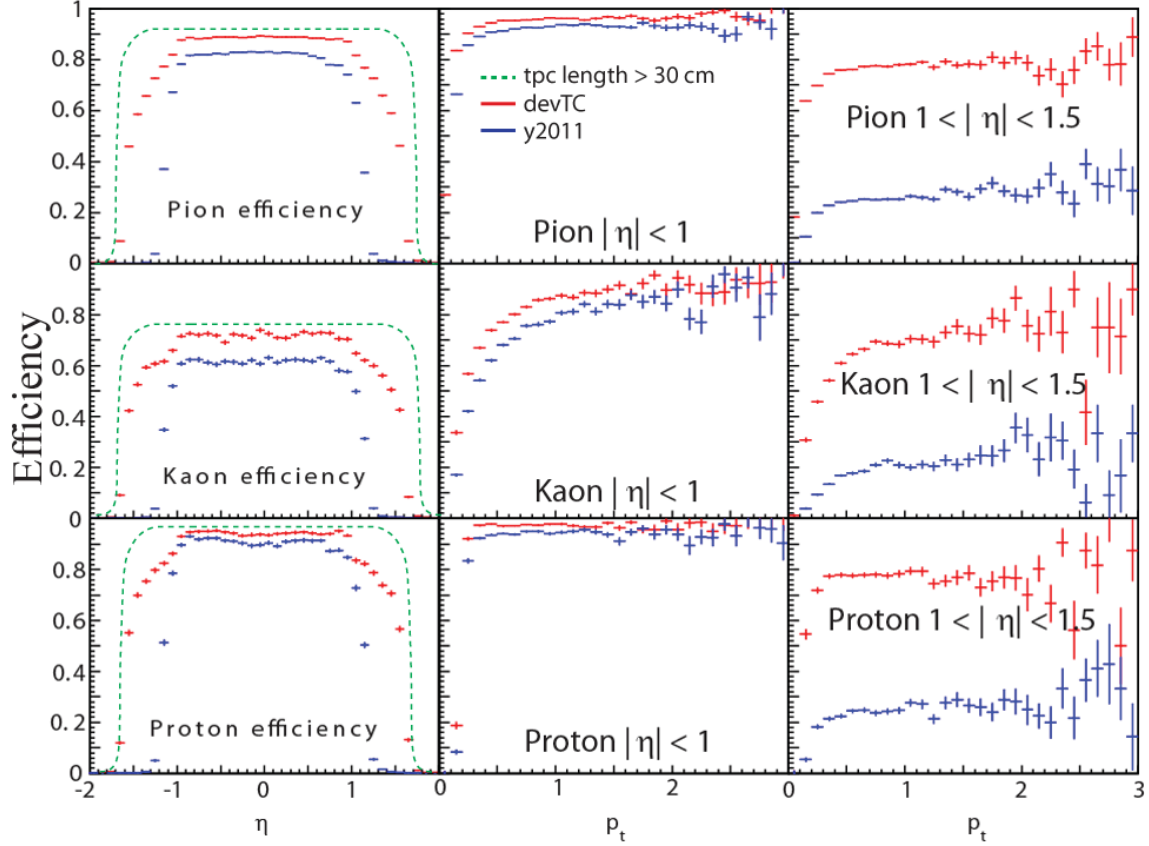


Figure 34: Efficiency of pion, kaon, and proton measurements as a function of pseudorapidity and transverse momentum (in GeV/c) for the current TPC design (blue) and for the *devTC* design (red). The theoretical curve for the efficiency for tracks longer than 30 cm is shown as a green dashed line.

The simulations show a dramatic increase in acceptance at high  $\eta$ , significant increase in  $dE/dx$  resolution and notable improvements in momentum resolution. For example, there is approximately a factor of 5 increase in acceptance at  $1 < |\eta| < 1.5$  and a factor of 2 increase for low  $p_T$  hadrons even at mid-rapidity.

The surprising result from Figure 33 is that improved momentum resolution does not depend on the width of the pads for the inner sector upgrade. The resolution only depends on sampled length of the track. The same conclusion is reached when looking at the  $dE/dx$  results presented in Figure 35.

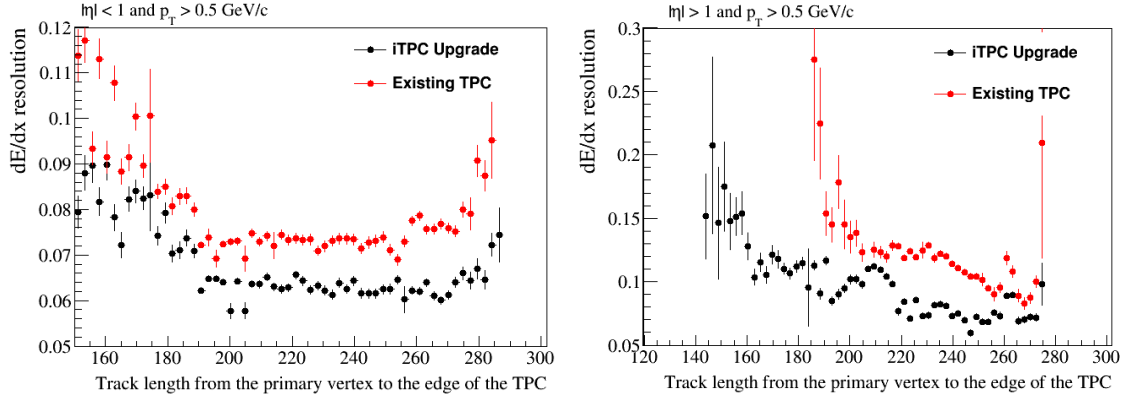


Figure 35:  $\frac{dE}{dx}$  resolution comparison for the existing and upgraded iTPC for two pseudorapidity regions.

The  $dE/dx$  resolution can be described roughly by a function of the form:  $(N_{dE/dx}^{0.5})^{-1}$ , where  $N_{dE/dx}$  is the number of sampled TPC hits used in calculating the  $dE/dx$  value. Thus, the  $dE/dx$  resolution depends only on the sampled track length. Figures 23 show the improvement in the  $dE/dx$  measurement due to the higher number of sampled track segments. The improvement in the forward direction ( $|\eta| > 1$ ) is even more dramatic, showing the  $dE/dx$  measurement at the track length which in the existing TPC are neglected due to insufficient number of the padrows. The improvement allows better  $dE/dx$  separation for pions, kaons, and protons at low momentum and enables better kaon and proton separations at high momentum as well as better electron identification.

## 4.2 Conclusions

In conclusion, the simulation studies confirm that additional pad rows on the inner sectors improve momentum resolution,  $dE/dx$  resolution and increases the acceptance of the detector. The results are not particularly sensitive to the choice of pad width or length. What is important is complete coverage of the inner sectors. So we have chosen configuration devTC for the iTPC upgrade; with a pad size of 4.5 mm x 15.5 mm (5 mm x 16 mm pitch). Using these larger pads, the inner sectors will have 40 pad rows (instead of existing 13) and a total of 3370 pads per sector. This is roughly double the number of pads in the existing inner TPC sectors.

## 4.3 References

- [1] Bichsel, H. (2006). A method to improve tracking and particle identification in TPCs and silicon detectors. *Nuclear Instruments and Methods in Physics Research Section A: Accelerators, Spectrometers, Detectors and Associated Equipment*, 562, 154 - 197.
- [2] Mathieson, E. (1991). *Induced Charge Distributions in Proportional Detectors*.
- [3] Wang, X.-N., & Gyulassy, M. (1991). HIJING: A Monte Carlo model for multiple jet production in p-p, p-Au and Au+Au collisions. *Phys.Rev.D.*, 3501-3516.



## 5 Padplane and MWPC Design

### 5.1 Introduction

In this section, we will discuss the padplane and MWPC chamber designs in more detail. The installation of the sectors (padplane + MWPC) into the STAR TPC using a sector insertion tool is a non-trivial operation that will be discussed in chapter 0.

The conceptual plan for the STAR TPC is shown in Figure 27 (see Section 3). The TPC, as actually built, is very similar to the conceptual plan and is shown in Figure 36. The photo was taken during construction at LBL. Note that the high voltage Central Membrane (CM) and the Outer Field Cage (OFC) are inside the TPC when the picture was taken but the Inner Field Cage (IFC) and MWPCs have not yet been installed.



Figure 36: The STAR TPC during construction at LBL. The tracking volume of the TPC is 4 meters in diameter and 4.2 meters long. The photo shows how each end of the TPC is divided into 12 super-sectors and each super-sector is divided into an inner and an outer readout sector.

As shown in the photo, each end of the TPC is divided into 12 super-sectors (one inner sector and one outer sector, each). A Multi-Wire Proportional Chamber (MWPC) was inserted into each sector-shaped hole in the end wheel, and electronics attached, after the picture was taken.

The goal of the iTPC upgrade project is to replace the existing inner sector MWPCs with new readout chambers and padplanes. The outer sectors do not need a performance upgrade nor have they experienced significant aging and so they will not be replaced, except perhaps to remove a sector and replace it with an existing spare if we suspect that it is necessary.

The physical parameters and dimensions for the TPC are shown in Table 4.

Item	Dimension	Comment
Length of the TPC	420 cm	Two halves, 210 cm long
Outer Diameter of the drift volume	400 cm	200 cm radius
Inner Diameter of the drift volume	100 cm	50 cm radius
Distance: cathode to ground plane	209.3 cm	Each side
Cathode	400 cm diameter	At the center of the TPC
Cathode potential	28 kV	typical
Drift gas	P10: 90% Ar, 10% CH <sub>4</sub>	He-Ethane as an option
Drift Velocity	5.45 cm/ $\mu$ sec	typical
Transverse diffusion ( $\sigma$ )	230 $\mu$ m/ $\sqrt$ cm	135 V/cm & 0.5 T
Longitudinal diffusion ( $\sigma$ )	360 $\mu$ m/ $\sqrt$ cm	135 V/cm & 0.5 T
Magnetic Field	0, $\pm$ 0.25 T, $\pm$ 0.5 T	Solenoidal

Table 4: Parameters and dimensions for the STAR TPC [1]

The design of the new inner sectors is related to the properties of the gas which fills the TPC tracking volume. The STAR TPC uses P10, a mixture of 90% argon and 10% methane. P10 is an excellent gas to use in a TPC because it is not difficult to manage and has a high drift velocity at a relatively low electric field setting. For example, the STAR TPC uses an electric field gradient of approximately 135 V/cm and achieves an electron drift velocity of 5.45 cm/ $\mu$ sec. See Table 4. The Argon is heavy (high Z) and allows for good  $dE/dx$  resolution by creating approximately 28 free electron-ion pairs per cm of track length. The methane, on the other hand, is a quench gas which soaks up UV photons that are created at the same time as the electron-ion pairs. The methane prevents the photons from creating additional secondary electrons via the photoelectric effect when they collide with the surfaces of the TPC.

One of the drawbacks to using P10, however, is that electrons suffer a relatively high rate of diffusion while drifting through the gas. Using the numbers in Table 4, it is easy to calculate that an electron cluster will spread to a width of 3.33 mm ( $\sigma$ ) due to transverse diffusion after drifting from the CM to the MWPC readout chambers. Similarly, the longitudinal diffusion will be 5.2 mm ( $\sigma$ ) or, equivalently, the cluster will be spread out in time with a FWHM of 225 nsec. Thus, the transverse diffusion sets the scale for the width of the readout pads on the MWPC padplanes while the longitudinal diffusion sets the time scale for the shaping parameters in the pre-amplifiers and sets the sampling fraction within the shaping time of the pre-amps.

In the original TPC design, the width of a pad was chosen to allow three or more pads to record a signal from a single electron cluster in the outer sector and four or more pads to record a signal in the inner sector. The inner sector pads were deliberately made narrower to allow for enhanced two-track resolution at small radii and in high multiplicity events. At the time, it was uncertain what the multiplicity of events would be in central Au+Au collisions at 200 GeV so a conservative design was implemented.



Also, since the pad width depends on the choice of the drift gas, the original TPC padplane was designed to be compatible with He-Ethane as well as P10. He-Ethane has a lower diffusion coefficient than P10 and potentially providing higher resolution. However, after 14 years of excellent performance with P10, He-Ethane is no longer under consideration. Thus, if we are going to replace the inner sectors of the TPC, it seems reasonable to re-optimize the width and length of the pads.

## 5.2 Padplane and MWPC Design Features

### 5.2.1 *Pad Size and Wire Spacing*

The STAR time projection chamber uses Multi-Wire Proportional Chambers with padplane readout to record tracks of ionizing particles. Figure 37 shows a photo of an outer sector MWPC and its associated padplane. The pads are 6.2 mm wide (6.7 mm pitch) and 19.5 mm long (20 mm pitch). Most importantly, the pads are contiguous and provide complete coverage of the readout plane under the anode wires. As discussed previously, and as shown in Figure 37, the inner sectors have smaller pads, which do not cover the entire area of the readout plane. A major goal for this upgrade project is to build new inner sectors that have the same hermetic coverage in the inner sectors as has already been achieved in the outer sectors.

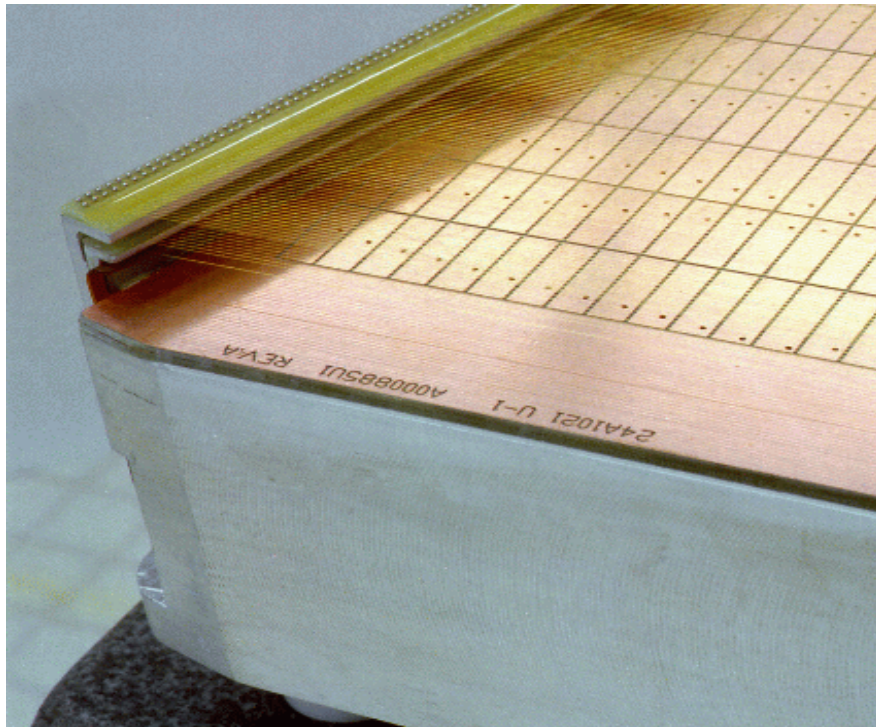


Figure 37: A photo of an outer sector padplane showing the MWPC, the padplane, and the Aluminum strongback that supports the padplane and wire grids. The MWPCs are really three grids of wires; the gated grid (top), the ground grid (middle, also known as the cathode grid), and the anode wires (bottom).

A side view of an inner sector padplane is shown in Figure 38. Note that the distance between the padplane and the anode wires, and also the distance between the anode wires

and the ground shield grid, is 2 mm, while in an outer sector, the padplane to anode wire separation is 4 mm. Otherwise, the structure of the inner and outer MWPCs is very similar. The anode wire plane in both the inner and outer sectors has one design feature that is different than in most other TPCs. It is a single plane of  $20\text{ }\mu\text{m}$  wires on a 4 mm pitch without intervening field wires. The elimination of the intervening field wires improves wire chamber stability and essentially eliminates the initial voltage conditioning requirement.

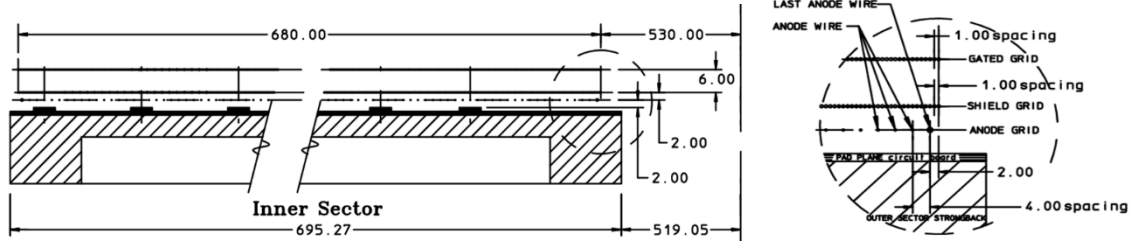


Figure 38: Side view of an inner sector adplane, strongback and wire grids. Dimensions are in mm.

The outermost wire plane on a sector is the gated grid (GG). It is located 6 mm from the ground shield grid in both the inner and outer sectors. The GG is a shutter to control the entry of electrons from the TPC drift volume into the MWPC. It also blocks positive ions produced in the MWPC from entering the drift volume where they could distort the drift field. The gated grid plane can have different voltages applied to the odd numbered and even numbered wires. The grid is ‘open’ when all of the wires are biased to the same potential (typically 115 V). The grid is ‘closed’ when the voltages alternate  $\pm 75\text{V}$  from the nominal value. During data taking in STAR, the gated grid is made transparent to the drift of electrons during an event and then closed the rest of the time. The positive ions are too slow to escape during the open period and normally are captured during the closed period.

The grid of ground shield wires is the middle grid in the MWPC. The ground shield is wound with  $75\text{ }\mu\text{m}$  wires. The primary purpose of the ground shield is to be the mirror image of the padplane on the other side of the anode wires. The grid can also be pulsed with a signal to calibrate the pad electronics. A resistive divider at the grid provides  $50\text{ }\Omega$  termination for the grid and  $50\text{ }\Omega$  termination for the pulser driver.

The gated grid and the ground shield establish the boundary conditions for the termination of the electric field in the TPC drift volume. For this reason, the gated grid and the ground shield wires in the inner and outer sectors are precisely aligned (i.e. the same distance from Central Membrane). This alignment preserves the uniform drift field in the TPC but it also creates a situation where the inner and outer anode wires and padplanes are not in the same position (i.e. different distances from the CM).

The effective spatial resolution for reading out isolated tracks on the padplane is given by a conceptually simple equation:

$$\sigma_{eff}^2 = \sigma_i^2 + \lambda \sigma_b^2 + \tan^2(\alpha) \sigma_c^2$$

Where  $\sigma_i$  is the intrinsic resolution of the padplane which depends on the pad response function,  $\sigma_b$  is a diffusion coefficient that must be multiplied by the distance,  $\lambda$ , that the electrons drift before reaching the padplane, and  $\sigma_c$  is a term proportional to the crossing angle of the track over the pad,  $\alpha$ .

Taking these terms in reverse order: the term proportional to the crossing angle is small and can be ignored for tracks which pass over the long axis of the pad (e.g.  $\alpha$  is small) [5]. The diffusion term is proportional to the distance over which the electrons drift, and it is not small. For example,  $\sigma_d = \lambda \cdot \sqrt{\sigma_b^2}$  is 3.3 mm for electrons that drift the full distance from the CM to the padplane in P10 gas. (See Table 4.) Finally, the intrinsic resolution of the pad is governed by the pad response function which depends on the width of the pads as well as the wire geometry over the pads.

The key to understanding the STAR geometry is to note that there are no field shaping wires in the anode plane. Therefore, the pad response function for pads of width  $w$ , and anode to padplane distance  $h$ , is easily calculated, in part because the anode wire spacing is larger than anode to padplane distance [2,3], (see Figure 39)

$$PRF(x) = \frac{1}{\pi} \left[ \tan^{-1}(\tanh(\frac{\pi}{2h}(x + \frac{w}{2}))) - \tan^{-1}(\tanh(\frac{\pi}{2h}(x - \frac{w}{2}))) \right]$$

The pad response function (PRF), is shown in Figure 39 for the old (blue) and new (red) padplane geometries.

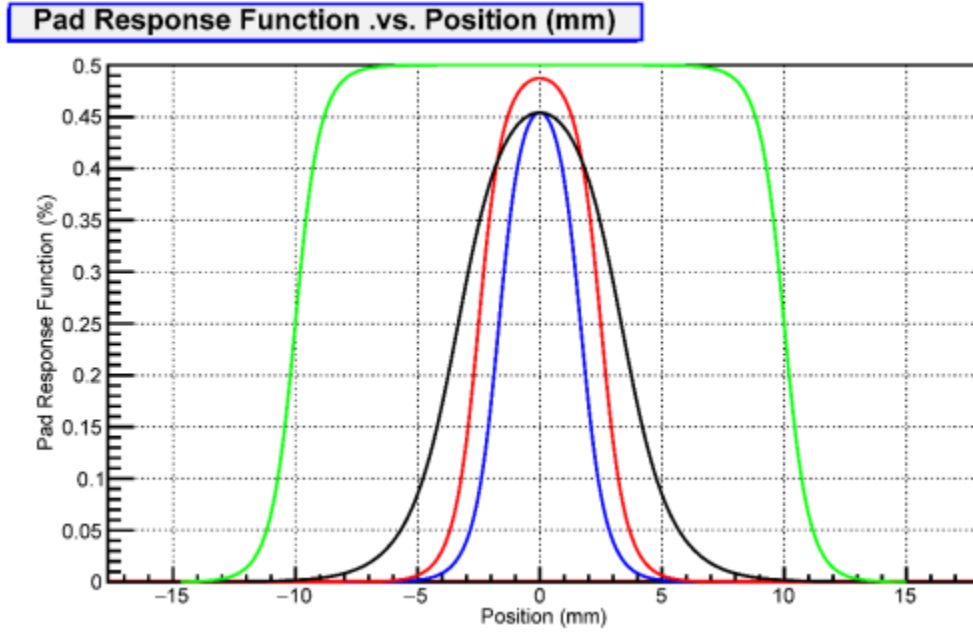


Figure 39: The pad response function for the outer sector is shown by the black line, the existing inner sector by the blue line, and the proposed inner sector by the red line. The pad spacing is 6.7 mm, 3.35 mm, and 5 mm respectively. The padplane to anode wire plane distance is 4 mm in the outer sector and 2 mm in the inner sector. The green line shows the PRF for a very wide pad, 20 mm, and it suggests that 50% of the signal goes to the padplane in the asymptotic limit. The diffusion width for an electron that drifts the full length of the TPC would be a curve that lies very close to the black line.

As expected, the PRF for new inner sector pads is wider than the PRF for the old pads but narrower than the PRF for the outer sector pads. As the width of the pad goes to infinity, the PRF goes to 50%, indicating that half the signal goes to the padplane and the other half to the ground grid. Note that the PRF for the outer sector (black line) is slightly wider but, overall, very similar to the width and shape for the diffusion term, 3.3 mm.

Figure 40 shows the effective pad response function,  $\sigma_{\text{eff}}$ , for the inner and outer pads in the TPC as a function of magnetic field. The pads are shown as rectangles while the circles define the  $3 \cdot \sigma_{\text{eff}}$  limit for the pad response function convoluted with the diffusion limit for electrons that drift the full length of the TPC. Circles are drawn for B field settings of 0 T, 0.25 T and 0.5 T. The  $3 \cdot \sigma$  limits at 0.5 T correspond to 4.5 pad widths in the outer sector, 6.7 pad widths in the inner sectors (and would be 4.9 pad widths if we also consider a new design with 5 mm pad spacing). As can be seen from Figure 40, the outer sector pads are very well matched to the diffusion width for clusters at full field and suitable for use in a fast, three-pad, online cluster finding algorithm. However, the inner sector pads are probably too small, and such fine sampling of the charge distribution is not necessary especially since we use an online cluster finding algorithm which uses three pads to define and locate a cluster. This intuitive conclusion is borne out by the padplane simulations presented in the Simulations chapter of this report.



Figure 40: Simulations of the effective pad response function for pads on the inner and outer TPC padplanes. The inner pads were assumed to be 3.35 mm wide and the outer pads 6.7 mm wide. The circles show the 3-sigma limit for the pad response function convoluted with the diffusion limit for particles that drift the full distance from the CM to the padplane. P10 gas is assumed. The different circles show the different response that is recorded when the B field is set to 0.0, 0.25 T, or 0.5 T. [4]

The simulations presented in the previous chapter suggest that the pad dimensions are not critical over a broad range due to the limits imposed by diffusion. In other words, the effective space point resolution does not change dramatically when the pad width is adjusted from 3.35 mm to 6.7 mm. This gives us the freedom to choose a new pad size that efficiently covers the full area of the inner sector while keeping the channel count within reasonable bounds.

Cost constraints, as well as limitations imposed by electronic packing density (e.g. connectors) suggests that it is reasonable to expand the number of electronic channels on the inner padplane by approximately a factor of 2. Another design constraint is that the inter-pad spacing should be chosen to be a multiple of the anode wire spacing (4 mm) because a group of anode wires (3, 4 or 5) must be precisely centered over a pad. This requirement forces the anode wires to be phase locked with the pads, and thus every pad row will have the same response to an incoming electron cluster.

There are three choices for the spacing of the pads in the long direction; the choices are 12, 16 or 20 mm. If we set a goal to double the number of channels on the inner sector then a satisfactory compromise can be achieved with pad pitch of 5 mm along the pad row and 16 mm perpendicular to the pad rows. This configuration creates 3440 channels in 40 rows. The 5 mm x 16 mm pad pitch will give a pad response function that is smaller than the diffusion width but otherwise is very satisfactory. (See Table 3 and Table 5.)

Item	Inner	Outer	iTPC	Comment
Pad Pitch (center to center)	3.35 x 12	6.70 x 20	5.0 x 16	mm
Isolation gap between pads	0.5	0.5	0.5	mm
Pad Size	2.85 x 11.5	6.20 x 19.5	4.5 x 15.5	mm
Number of Pads	1750	3940	3440	
Anode to padplane spacing	2	4	2	mm
Anode voltage	1170 V	1390 V	~ 1120 V	20:1 S/N
Anode Gas Gain	3770	1230	~ 2000	nominal
Anode Wire diameter	20 $\mu$ m	20 $\mu$ m	20 $\mu$ m	Au plated W
Anode Wire pitch	4	4	4	mm
Anode Wires phase locked to pad location	3 wires, #2 over center	5 wires, #3 over center	4 wires, centered	grp centered over the pad

Table 5: Parameters for the original and new STAR TPC padplanes [1]

The original MWPCs and electronics were designed to work with a 20:1 signal to noise ratio. So, what is the anode wire gain that will be required to produce a comparable signal over the new padplane geometry? We will study this question simply by scaling from the previous performance of the inner sectors. For example, the new pads are longer and more charge is deposited on the longer pad, but a wider pad also helps because it samples the pad response function convoluted with the transverse diffusion width of signals. Putting these factors together suggests that the new, larger, pads will collect nearly twice as much signal as the small pads on the inner sector. We will not attempt to do this calculation precisely here, except to point out that scaling by length and effective width suggests that a gain of 2000 is more than sufficient for reliable operation of the new inner padplane geometry. This is a significant reduction in gain compared to the old inner sector gain setting at 3770.

Lower gain on the inner anode wires suggests that the corresponding voltage can be lower. The voltage on the anode wires is easy to calculate because STAR has measured the gain on the anode wires using an  $^{55}\text{Fe}$  source in a prototype wire chamber and prototype TPC electronics [2, 6]. (Note that the voltage and gain characteristics of a wire chamber do not depend on the pad size as long as the padplane is fully covered with pads or equivalent ground plane.) Assuming a 200 ns FWHM pre-amplifier shaping circuit, then the gain on the inner sector is [7]:

$$G_{inner} = \exp(0.01267(V - 520)) \quad \text{where } V \text{ is given in volts.}$$

Thus, 1120 volts on the anode wires will yield a gain of 2000. This is a very reasonable number and should not be a problem to achieve with the upgraded MWPC design.

### 5.2.2 *Reduced Voltage on the Inner Anode Wires*

It is generally good news that a lower gain setting can be used on the inner anode wires because the STAR TPC has been suffering from breakdown (i.e. sparking) of the inner sector MWPCs at the highest beam luminosities (e.g. p-p collisions at 500 GeV).

There are three possible explanations for the breakdown: stray radiation from the accelerator, aging of the wires in P10 gas, and/or the Malter affect. Stray radiation may be present in the TPC due to background and parasitic beams of muons that created in the accelerator tunnel upstream of STAR. There is little that we can do about this except to ask for better beam tunes and to install more shielding in the tunnel (scale length  $\sim 1$  meter of steel).

Aging is caused by the build-up of hydrocarbons on the anode wires. Reactive hydrocarbons are most likely produced by cracking of the Methane in the P10 gas due to ionizing radiation and the subsequent avalanche near the anode wires. Unfortunately, the hydrocarbons stick to the anode wires and, as the layer gets thicker, it increases the radius of the wire and lowers the gain (even though the applied voltage is constant). When the carbon build up is large enough, it can lead to sparks due to the irregularities in the layer of crud on the wires. Aging affects the anode wires and is proportional to the amount of applied radiation and to the gain applied to the wires.

A less studied effect may also be contributing to the breakdown of the MWPCs. The Malter effect occurs when a thin insulating layer builds up on the cathode wires (i.e. Shield Grid). The insulating layer allows positive charge to build up on the cathode, without dissipating, and eventually leads to a spark through the insulating layer and perhaps elsewhere.

In recent years, the breakdown problem was solved by lowering the voltage and gain on the inner anode wires. We are currently running the inner sectors at 1100 volts and this reduces the gain to 40% of the nominal setting. (The gain drops from 3770 to 1550.) Fortunately, the TPC tracking algorithms still work, but this forces us to work with smaller signal to noise ratios in the inner sector data and thus it compromises the quality of the  $dE/dx$  information.

In the future, we will be replacing the inner sector wires at the same time that we introduce the new padplanes. Thus, aging will be reset to year-one conditions and we can probably expect many years of stable operations without adjusting the voltage on the anode wires. But even if we are forced to run the inner anodes at 1100 volts (instead of 1120), this means the S/N ratio for the new MWPCs will be a factor of two larger than the S/N ratio for the old MWPCs. This is good, and this will increase the quality of the  $dE/dx$  information from the inner sectors, even in the worst case that excess radiation is the dominant problem.

### 5.2.3 Pad Plane Geometry & Wires: Old compared to New

The Old and New inner pad plane geometries are shown in Figure 41 and Figure 42, respectively. The principal changes are

- Larger pads on the inner sector (5 x 16 mm pitch .vs. 3.35 x 12 mm pitch)
- More pad rows and complete coverage of the pad plane (40 rows .vs. 13 rows)
- Lower voltage on the anode wires (1120 V .vs. 1170 V)
- Lower gain on the anode wires (2000 .vs. 3770)
- Extra low-gain wires on the ends of the anode grids to help terminate the electric field lines emanating from the anode grid

In order to make space for the extra low-gain wires, the centerline for the 40<sup>th</sup> pad row will be moved away from the inner/outer gap by an additional 14 mm. This does not affect the tracking algorithms in any significant way because the shift is small and because the tracking is improved so much more by the addition of the extra pad rows.

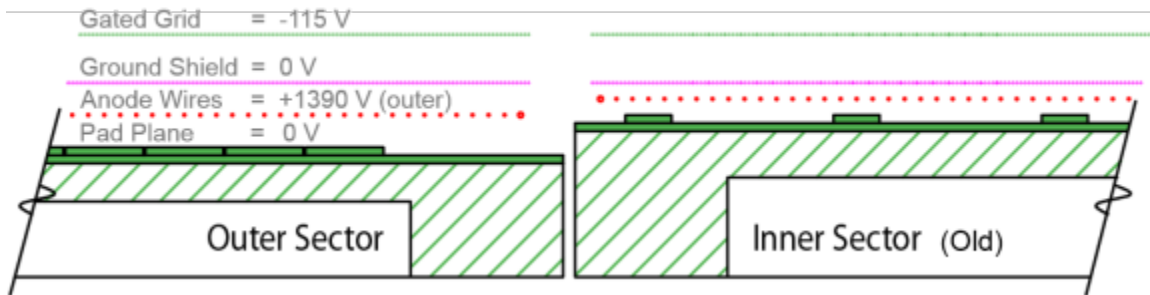


Figure 41: The original STAR pad plane geometry (side view). The outer sector pad rows covered the entire pad plane but the inner sector pad rows were widely spaced ( $> 5$  cm).

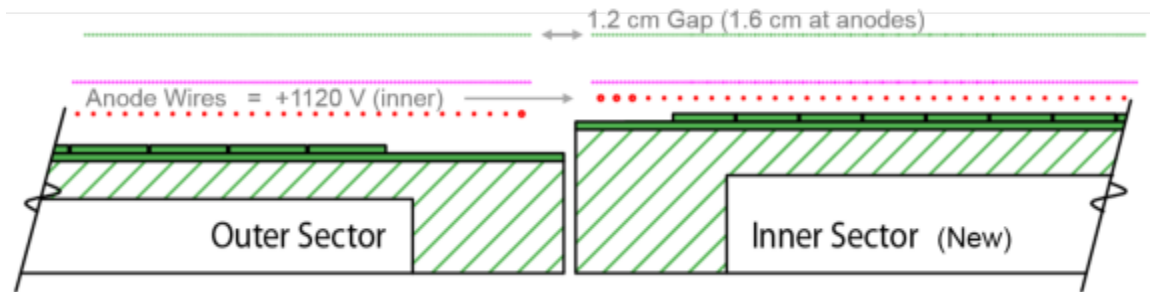


Figure 42: The new STAR pad plane geometry. The outer sector configuration remains the same, but the inner sector has more pad rows and there aren't any gaps between the pad rows.

It is not shown in the figures, but the bottom end of the anode wire grid (pad row 1) is a mirror image of the top end of the grid; in other words, there will be three low-gain wires on the bottom end of the grid, too, to help seal off any ion backflow in this area.



#### 5.2.4 Modifications to the Gated Grid

There is a 12 mm gap between the grids on the inner and outer sectors. Figure 43 shows a detailed view of the boundary region between the sectors. As can be seen in the figure, the grid of wires stops before the physical end of the strongback material. The open space is the result of mechanical constraints that occur near the sector edge; but the net result is that there is a 12 mm wide gap between the end of the gated grid on the inner sector and the start of the gated grid on the outer sector. (See Figure 42 but also note that the gap is 16 mm between the anode grids) The gap between the grids allows electric field lines to propagate directly from the Central Membrane (CM) and go all the way to the anode wires. And, conversely, positive ions created near the anode wires can leak out into the drift volume of the TPC where they create space-charge and the resulting cloud of positive charge distorts the trail of incoming secondary electron clusters.

The Grid Leak distortion is luminosity dependent; it depends on the number of incoming secondary electrons and the gain on the anode wires. Currently, we remove the distortion from the raw data by using a mathematical model but it would be better to eliminate the distortion, completely.

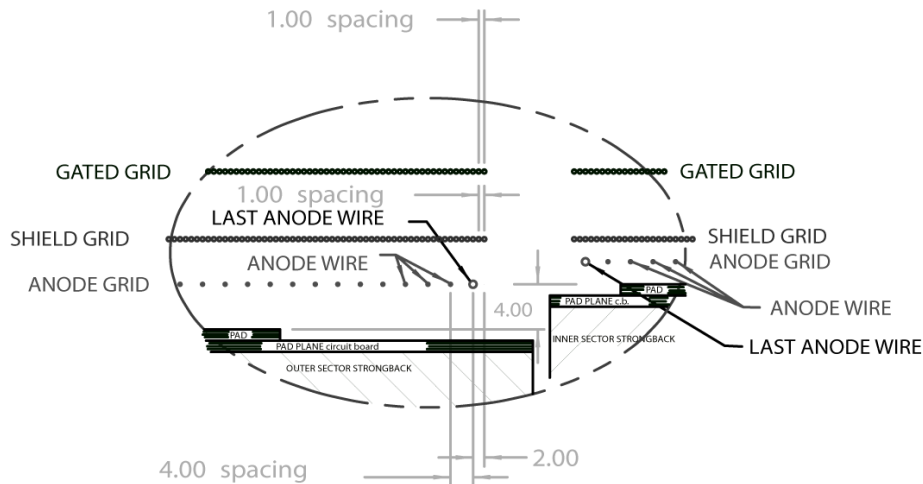


Figure 43: A detailed view of the gap between the inner and outer sectors. Note that there is a 12 mm gap between the end of the gated grid in the inner sector and the start of the gated grid in the outer sector and a 16 mm between inner and outer anode grids. Also, note that the last anode wire is larger in diameter (125  $\mu\text{m}$ ) than the rest of the anode wires (20  $\mu\text{m}$ ).

There are several solutions to the grid-leak problem which could be implemented during the iTPC upgrade. The easiest thing to do is to replace some of the small diameter anode wires with larger wires in order to reduce the gain of the grid wires near the gap. The last wire in the grid is already a large wire and it was placed there in order to minimize the gain near the gap; however, experimental evidence suggests that the one wire solution is not sufficient to plug the grid leak and additional low gain wires may be needed. As previously discussed, we propose to put 3 large diameter (low-gain) wires in this position. See Figure 44. However, this is only a partial solution to the grid leak problem because the low gain wires can only be replaced on the inner sector. More than half of the ions, in the grid leak region, come from the outer sector.



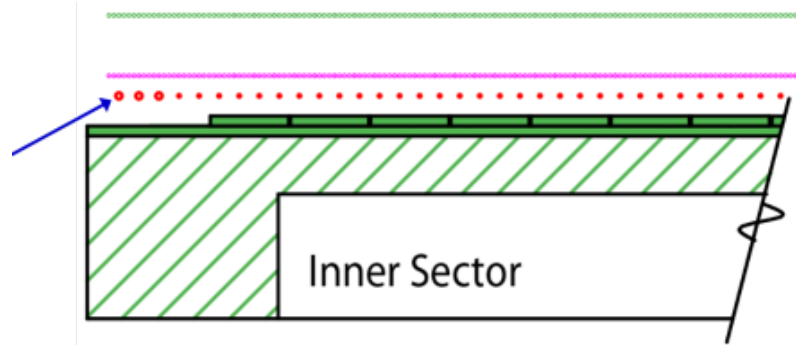


Figure 44: Three low gain wires (125  $\mu\text{m}$  diameter) will be placed on both ends of the anode wire grid. The low gain wires will reduce the production of ions in the region where they can leak into the drift-volume of the TPC. Another option is to ground the last wire so that the gain is zero on that wire.

Another solution to the grid-leak problem would be to terminate the electric field lines emanating from the anode wires so that ions cannot leak out of the gap. This is what was done for the ALICE TPC. Their inner readout chambers have a wall between the inner and outer sectors. The wall is made of G10, it has copper traces on both sides, and these strips are wired so they can be biased to appropriate potentials. (See Figure 45 and Figure 46.)

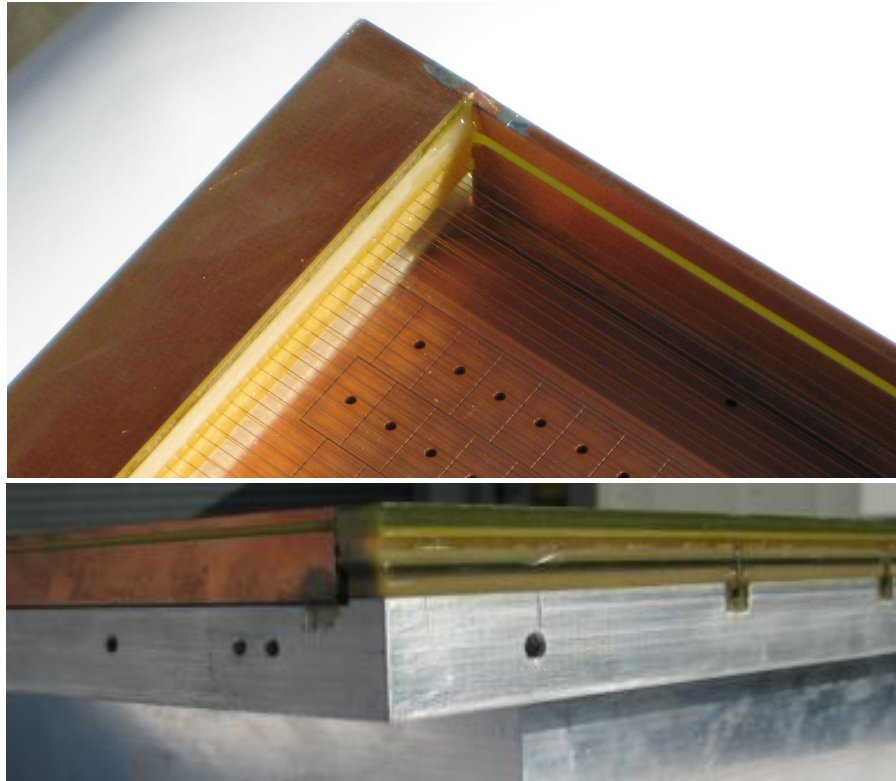


Figure 45: A top view and a side view of an ALICE inner readout chamber (iROC). The figures show a potential solution to the “grid leak” problem which is to terminate the plane of wires with a wall of G10. The wall has Cu traces that are biased appropriately to terminate the field lines coming from the anode wires and gated grid.

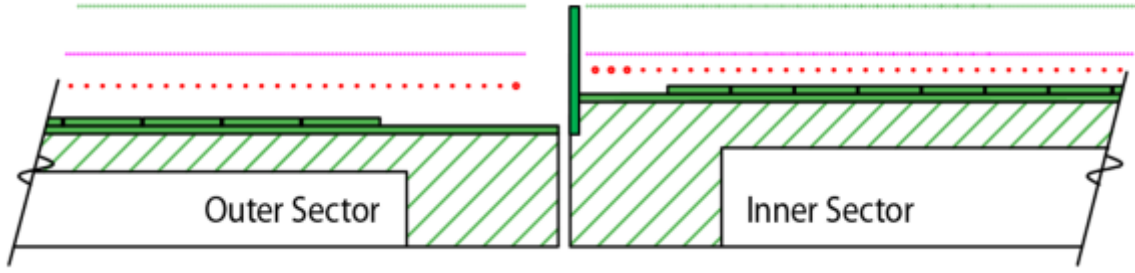


Figure 46: A side view showing how a biased wall might be implemented at STAR. The wall is designed so it can be biased to  $\sim 500$  Volts and will attract field lines coming from the anode wires. Thus, positive ions produced near the anode wires terminate on the wall and do not leak out into the gap between the inner and outer sectors.

We have performed realistic simulations of the ion flow in and around the boundary region between the inner and outer sectors using GARFIELD (with gas parameters from MAGBOLTZ). Two geometries were tested; a simple wall, discussed above, and an “L” shaped wall that rises vertically but bends over between the ground grid and the Gated Grids. See Figure 47.

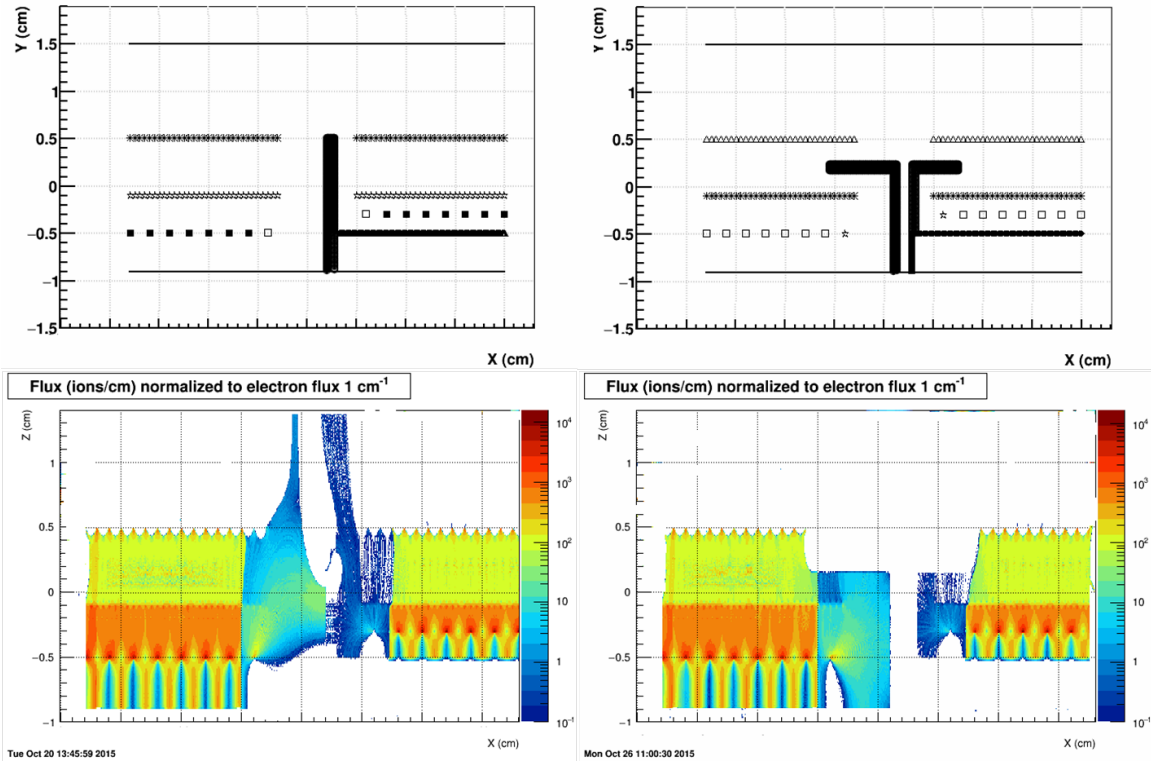


Figure 47: GARFIELD simulations of ions flowing away from the STAR TPC anode wires when the Gated Grid is closed. There is a 1.2 cm gap between the Inner and Outer sectors that is not covered by the Gated Grids. This gap allows ions to flow out of the MWPC region and into the tracking volume of the TPC. Putting a -690 volt bias (left panels) on the wall reduces the flow of ions, while the “L” shaped wall (right panels) completely stops the flow of ions. The “L” shaped wall was held at 0 volts in this simulation.

The panels in Figure 47 illustrate how ions flow away the anode wires and go up into the tracking volume of the TPC. The pad plane is at the bottom of the figure while the STAR Cathode is (artificially close) at the top of each figure. The anode wires are placed at -0.5 cm (Outer) and approximately -0.3 cm (Inner). The ground grid is near 0 cm while the gated grids are up at 0.5 cm. Note that the major tick marks on the vertical axis are 0.5 cm graduations on the vertical axis, but 1.0 cm graduations on the horizontal axis. If there were no walls in the simulation, then a vigorous flux of ions would flow upwards. If a simple wall is included in the simulation and biased to -690 volts, the flux of ions is reduced by a factor of 50. But if a pair of “L” shaped walls are used, then the flux drops to zero (lower than can be measured in this simulation). The L shaped walls were grounded for this simulation and so this is the preferred solution for stopping the leak of ions between the inner and outer sectors. The inner L shaped wall is easy to install because we are making new sectors and they can be installed as part of the manufacturing process; however, the outer L shaped wall is not so easy to install. The outer sectors will remain inside the TPC and will not be dismantled for the iTPC upgrade. Thus, we will have to work inside the TPC tracking volume in order to install the L shaped wall on the outer sectors. A team of engineers and scientists is working on a clever (and risk free) solution to this problem, however, the -690 volt wall is also a viable solution and will be our chosen solution if the installation of the L shaped walls is too complicated.

### 5.3 References

- [1] STAR TPC NIM, M. Anderson et al., Nucl. Instrum. Meth. A 499, 659 (2003).
- [2] Wayne Betts, “Studies of Several Wire and Pad Configurations for the STAR TPC”, Thesis UT Austin, STAR Note SN0263.
- [3] Blum, Riegler and Rolandi, “Particle Detection with Drift Chambers”, Springer, 2008.
- [4] Roy Bossingham, [http://www.star.bnl.gov/public/tpc/hard/signals/signal\\_division.html](http://www.star.bnl.gov/public/tpc/hard/signals/signal_division.html)
- [5] STAR Conceptual Design Report, STAR Note SN0499.
- [6] STAR CDR Update, <http://www.star.bnl.gov/public/tpc/notebooks/CDRUpdate.pdf>
- [7] STAR FEE NIM, M. Anderson et al., Nucl. Instrum. Meth. A 499, 679 (2003).

## 6 Padplane Design and Prototype Construction

The iTPC upgrade represents a significant increase in the number of necessary electronics channels. The precise count will depend on the final pad geometry and padplane layout chosen. All geometries under consideration suggest that this will be at least a factor of two increase in the number of channels.

The size and outer dimensions of the new padplane should be exactly the same as the original version. Also, the padplane PCB needs to be gas-tight and mechanically rigid as it is a crucial part of the overall inner sector support structure. We plan to closely imitate the old padplane in terms of thickness and PCB material.

Due to the complexity of the PCB and its higher density of channels we wanted to design and manufacture a first version prototype with as many of the required features as possible, but which also placed the electronics connectors at the very edges to try to lessen the amount of mass in the central region. Figure 48 shows an early prototype.

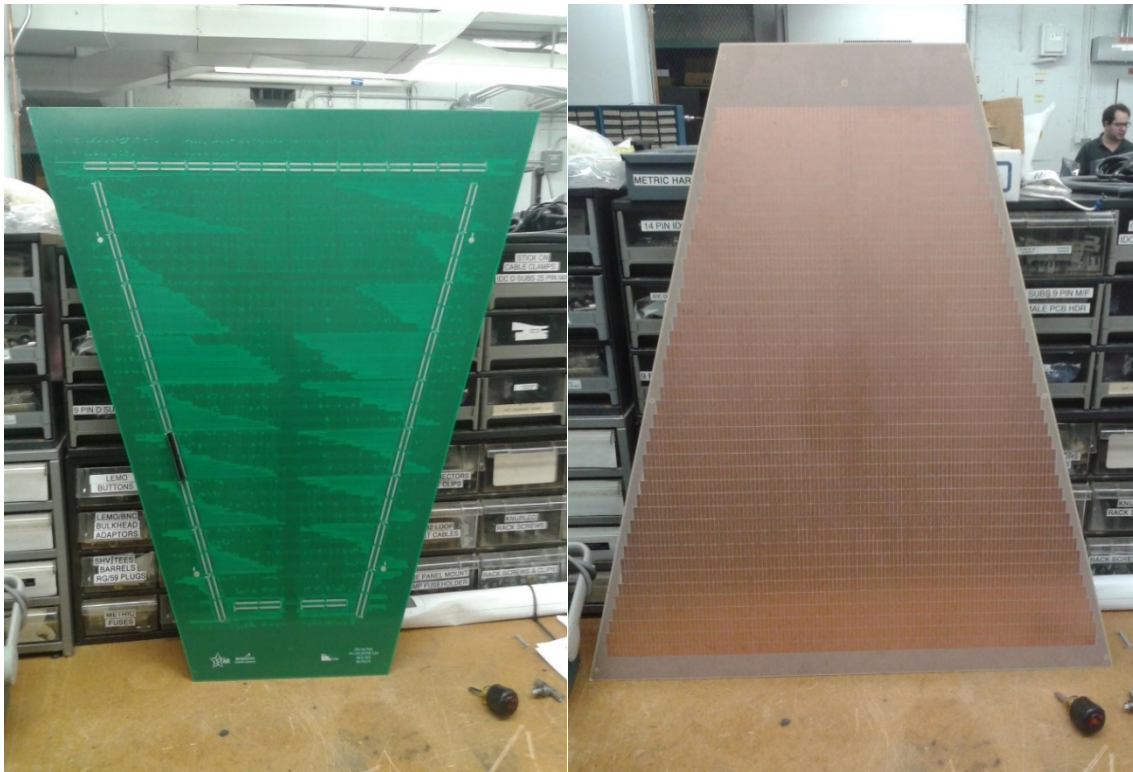


Figure 48: The first padplane prototype. Left, connector side. Right, pad side.

We evaluated the prototype padplane and measured the per-channel noise due to the capacitance of the PCB copper traces connecting the pad area to the connector and found that there is a limit to the length of the trace that we can tolerate. The measurements (see Figure 49) show that the geometry with the connectors along the padplane edge does not meet our current signal to noise requirements.

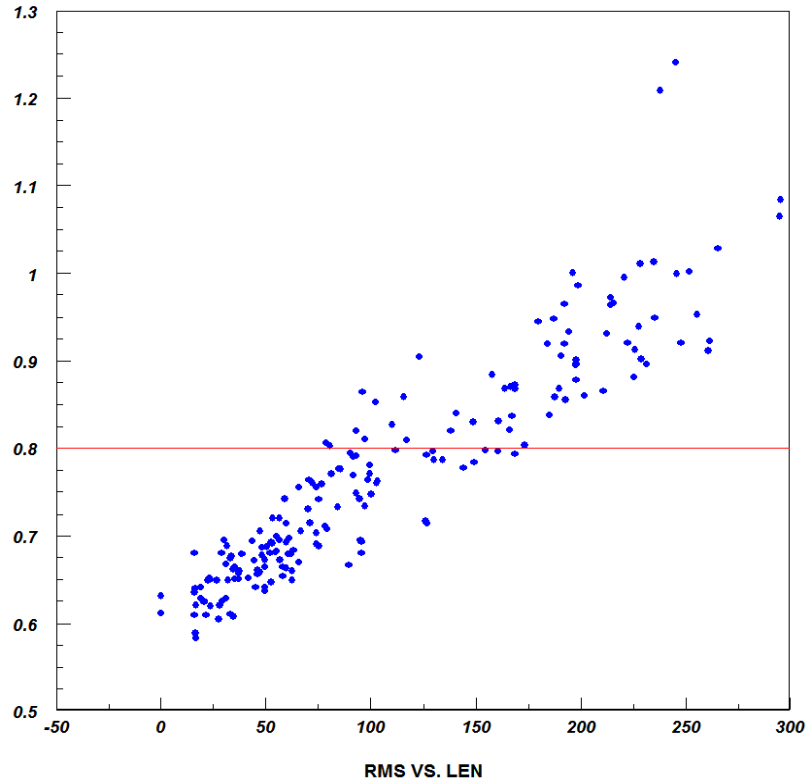


Figure 49: Electronic noise as function of trace length. The noise is measured in ADC counts and trace length is in mm. The red line represents the maximum allowable noise based on the current TPC's electronics.

Additionally, the geometry with connectors along the edge would need a complete redesign of other mechanical components such as the strongback and various mounting and cooling manifolds; even requiring a change in the MWPC wire termination scheme. Thus we felt that we should go back to the existing TPC design where the padplane connectors are distributed along the full surface of the padplane. This “standard” geometry is known to work well in the STAR TPC and so this is where we are concentrating our efforts.

The design of current version of the padplane is shown in Figure 50. The number between the right edge of the padplane and the pad row number is the number of pads read out in each row. There are a total of 3520 electronic channels but only 3440 pads. So 80 channels are not used in this configuration. The black bars indicate the location of the 55 iFEE readout boards.

Figure 51 shows a summary table giving the location of the first and last pad rows on the new padplane. The padrows repeat every 16 mm, the anode wires repeat every 4 mm, the Gated Grid wires every 1 mm, and the ground grid (not shown) every 1 mm. The location of the primary and secondary fiducial marks, for survey purposes, are also shown.



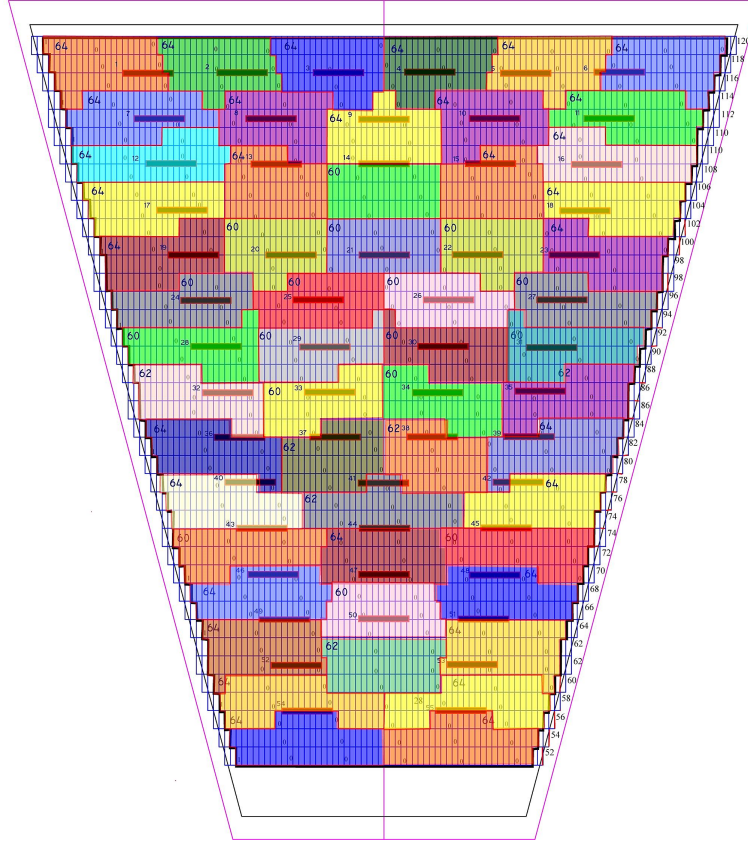


Figure 50: The new padplane design for the iTPC. The black bars are the locations for the iFEE connectors and the colored zones map out the pads that communicate with each iFEE card. The grey trapezoid outlines the dimensions of the aluminum strongback that lies under the padplane, while the red trapezoid shows the original PC board dimensions prior to trimming to size and shape.

Radius (Y)	local X	Pads	Description
0.00	0.00		Center of STAR Detector (vtx)
498.80	0.00		Bottom of Full size PC Board
512.70	+/-129.97		Bottom Row Tertiary Fiducial L&R
519.05	0.00		Strongback Bottom Edge
530.00	0.00		Gated Grid Wire 1
531.00	0.00		Gated Grid Wire 2
532.00	0.00		Anode Wire 1 & GG W-3
536.00	0.00		Anode Wire 2 & GG W-7
540.00	0.00		Anode Wire 3 & GG W-11
540.25	0.00		Secondary Fiducial
544.00	0.00		Anode Wire 4 & GG W-15
548.00	0.00		Anode Wire 5 & GG W-19
558.00	0.00	52	Pad Row 1 - Center
574.00	0.00	54	Pad Row 2 - Center

1166.00	0.00	118	Pad Row 39 - Center
1179.45	0.00		Primary Fiducial
1182.00	0.00	120	Pad Row 40 - Center
1192.00	0.00		Anode Wire 166 & GG W-663
1196.00	0.00		Anode Wire 167 & GG W-667
1200.00	0.00		Anode Wire 168 & GG W-671
1204.00	0.00		Anode Wire 169 & GG W-675
1204.85	0.00		Alternate Primary Fiducial
1208.00	0.00		Anode Wire 170 & GG W-679
1209.00	0.00		Gated Grid Wire 680
1210.00	0.00		Gated Grid Wire 681
1214.32	0.00		Strongback Top Edge
1220.67	+/-319.68		Top Row Tertiary Fiducial L&R
1235.42	0.00		Top of Full size PC Board

Figure 51: The location of first and last pad rows on the iTPC padplane. Other significant landmarks are included in the table.

We selected an 80 pin dual-row 1.0 mm pitch connector for the iFEE connection to the padplane (Samtec MEC1-80, see Figure 52). Once a new prototype padplane is produced

we will repeat all the necessary noise and crosstalk measurements. This work is in progress. When the new padplane prototype is done, we will present it to the mechanical and MWPC groups for their comments and final signoff.

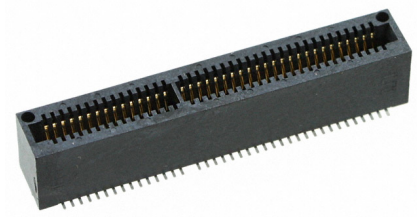


Figure 52: Samtec MEC1-80 series connector for the pad-to-iFEE connection

## 7 Strongback Engineering and Construction

### 7.1 Overview

The strongback is the largest mechanical element required for the iTPC upgrade. It is a high precision platform for mounting the padplanes and wire chambers inside the TPC and, simultaneously, the base for mounting the front end electronics and cooling manifolds on the outside of the TPC. It fits snugly into the endwheel of the TPC; twelve on each end of the TPC.

In this chapter, we will discuss the original strongback design (circa 1995) and the rather small number of changes that are required to make that design useful in the iTPC era.

Re-learning the techniques that were used to build the original strongbacks and wire chambers is a critical task because we do not have a present day work force who are familiar with the design and construction of the STAR TPC. Most of the people who built the TPC have retired and no one else has worked on the internal structures of the TPC since it was built. We do have a large number of mechanical and electrical drawings, as well as the original quality control documents that are suitable for fabrication of a new generation of components. See Table 6. However, the drawings for several small components and some of the fabrication tooling never made it into the official archives. We are recovering the missing information by interviewing the responsible technicians, collecting their personal archives, or learning enough about the missing items to be able to design modern components based upon oral specifications.

<b>Drawing #</b>	<b>Description</b>
24A054	Inner/Outer Wire Mount Taper Pin
24A055B	Inner/Outer Sector Wire Grid Configuration
24A368D	Inner Sector Strongback
24A374	Inner Sector Pad Plane Assembly
24A381	Inner Sector O Ring Groove Machining
24A382	Inner Sector Strongback Mounting Hole Pattern
24A410	Outer Sector Assembly Drawing Tree (QA Document)
24A424A	Inner/Outer Sector Wire Mount Thread Support, 10-32
24A425A	Inner/Outer Sector Wire Mount Thread Support, .25-20
24A428	Outer Sector Strongback Spot Inspection (QA Document)
24A494	Inner/Outer Sector Quality Assurance Plan (QA Document)

Table 6: A brief list of the important mechanical drawings, and QA documents, from the original STAR TPC design project (circa 1995). Drawing 24A368D is the key design drawing for the iTPC project. All of these drawings, and many more, are available in 2D format from the LBL/STAR archives.

Thus, an important task associated with the re-learning phase of the project is to collect all of the available information regarding the construction of the STAR TPC sectors and then to update and extend this information based upon modern goals and specifications. We also plan to redraw the relevant 2D drawings using modern 3D engineering tools;



filling in the gaps in our knowledge, where necessary, with modern engineering analyses. The reason for making the transition to 3D is to allow for sophisticated engineering analysis, at low cost, and to facilitate the fabrication of the parts in today's software based machine shop environment. See Figure 53.

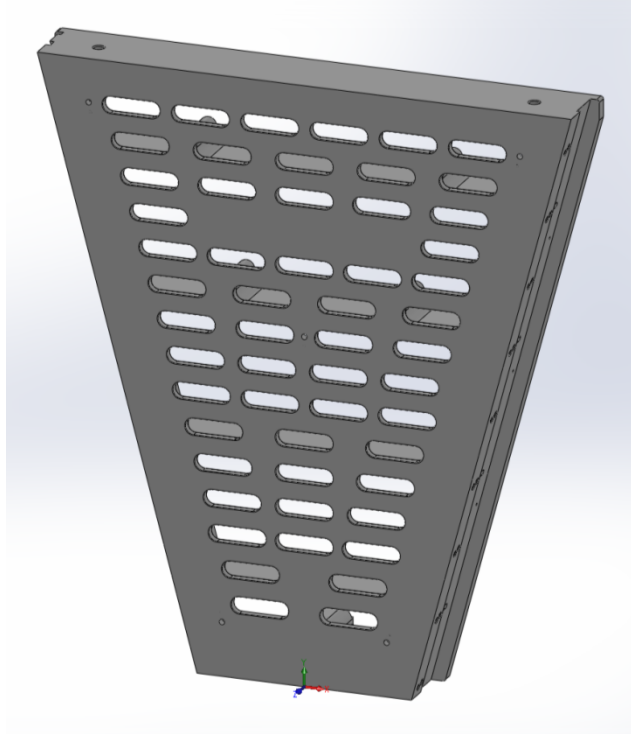


Figure 53: The STAR Inner Sector Strongback (24A368D) rendered in CREO Elements Direct (circa 2015)

## 7.2 Strongback

The strongback is a rigid aluminium base to support the padplane, anode wires, ground plane and gated grid. The wire planes face towards the inside of the TPC. The front end electronics and cooling manifolds are also supported by the strongback but these elements are mounted on the other side (the outside).

We recently fabricated two prototype inner sector strongbacks in the machine shop at the University of Texas at Austin (see Figure 54). This was an exercise in using the original 2D drawings to learn more about the mechanical properties of the strongback. It was also an exercise to estimate the cost and schedule for fabricating 24 (+spares) of the strongbacks. It took about two months to make the first strongback. The second strongback was made in one month. The photograph on the left hand side of Figure 54 shows the backside (outside) of a strongback during fabrication. The backside carries the electronics and water manifolds for cooling the electronics. The space between the ribs, shown in the figure, will be filled with electronics (preamplifiers and readout boards) and the electronics will be attached to the padplane through clearance holes which have not yet been cut into the prototype. The old clearance hole pattern, a series of slots, can be seen in the mechanical drawing on the right hand side of Figure 54.

The right hand side of Figure 54 shows one of the many mechanical drawings that are available to the iTPC project. These drawings include fabrication notes and other details about materials and techniques.

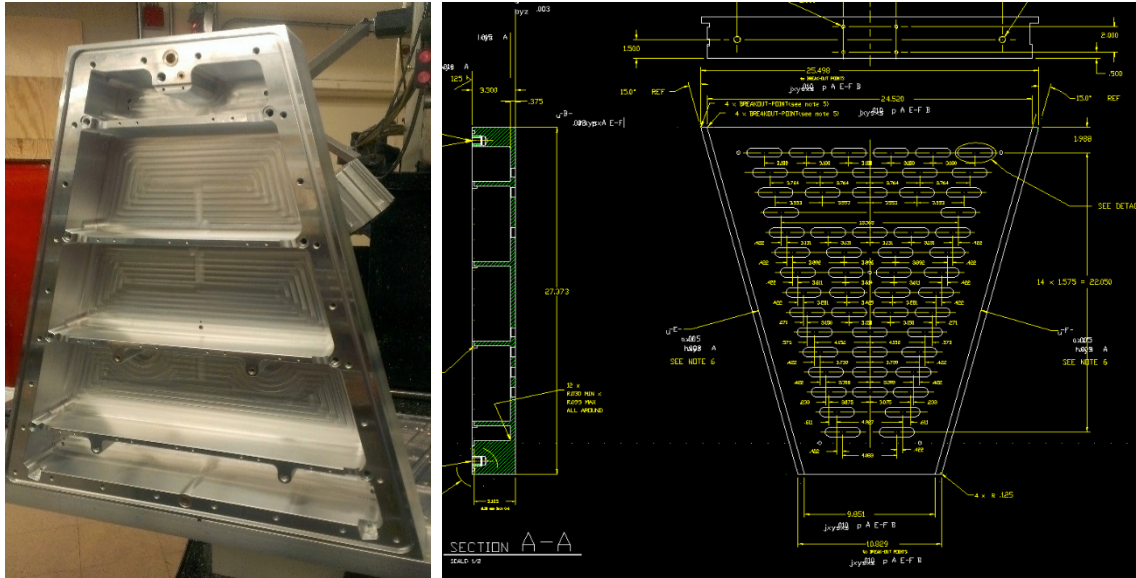


Figure 54: A prototype inner sector strongback is shown during fabrication at the University of Texas (circa 2013). The sector was machined out of a single piece of aluminum. Dimensions are: ~27 inches tall, ~25 inches wide and weight ~70 lbs. The sector is viewed from the backside.

A new padplane and the MWPCs will be attached to the front face of the sector (see Section 6 and Section 0 ). The requirements for the strongback are quite stringent. For example, after gluing the padplane to the strongback, the padplane must be flat to better than  $\pm 0.0005$  inches (10-15 microns) in order to ensure uniform gain ( $\pm 1\%$ ) in the MWPCs. This will be achieved by gluing the padplane to the strongback on a Grade A granite table (see Section 9).

The front face of a spare inner sector (circa 1995) is shown in Figure 55. The padplane and MWPC grids are installed and visible in the figure. The strongback is not visible but the overall shape, width and depth of the sector can be estimated from the size of the hands and tools shown in the figure. The old padplane is shown in the figure; the new padplane will include more pad rows but the wire grids and electronics on the sides will look the same.

### 7.3 Changes to the Strongback

There are two important changes to the strongback that will be required for the iTPC project. First, the new front end electronics cards (iFEE) have a slightly different connector than the previous generations of electronics cards. Thus, all of the electronics mounting holes shown in Figure 53 will be lowered by 5.6 mm (0.221”).

Second, we would like to implement one, or more, of the solutions to the grid leak problem that were described in Section 5.2.4



Figure 55: Experts examining a spare inner sector for the TPC. Note the old style padplane with electronics cards (ABDB boards) mounted along the edge of the sector. Normally the spare sectors (STAR has two spare sectors) are sealed in a storage box and kept under dry nitrogen.

The common theme for all of the grid leak solutions is to have the ability to mount a wall between the inner and outer sectors. This is easy to do and the strongback design can be modified to allow for a PCB wall (0.062" thick) to be mounted on the top and bottom ends of the sector. All that is required is a notch for the PCB board and if, for some reason we don't want to use it, we can always fill it with a smaller PCB board. An additional channel will be needed to allow wires to run under the wall. See Figure 56.

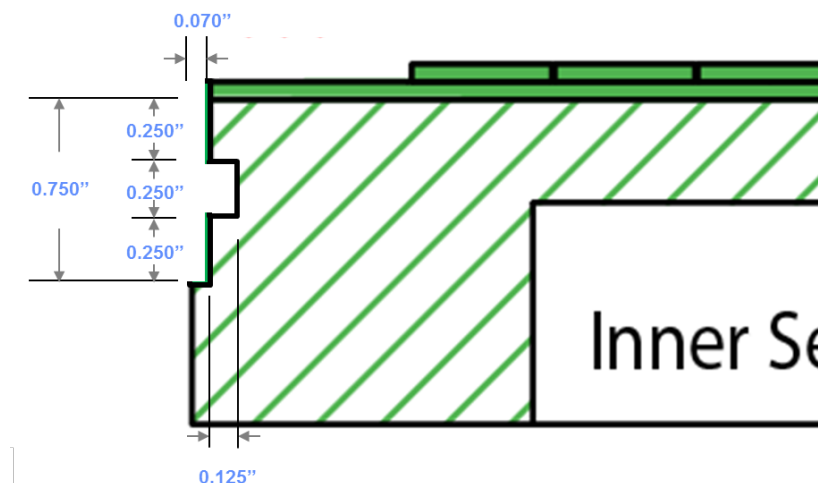


Figure 56: The inner sector strongback will be modified to include a 0.070" deep notch on the top and bottom ends of the sector. The notch will be used to mount a wall between the inner and outer sectors.

No other changes are contemplated for the basic design of the inner sector strongback.

#### 7.4 Quality Control

Quality Control is a topic that was taken seriously by the 1995 TPC project and which will be taken seriously by the iTPC project. We are fortunate to be able to follow in the footsteps of the previous project because most aspects of the original QA plan were archived and have been preserved.

For example, LBL Drawing 24A410 is the Outer Sector Drawing Tree. It is a compact, visual, representation of all the components that must be fabricated in order to complete the project. See Figure 57. 24A428 is the Outer Sector strongback spot inspection plan and document. A corresponding inner sector spot inspection document does not exist but we can use the outer sector documents because the QA plan for the inner and outer sectors is so similar.

Each new drawing will be prepared to the ASME Y14.5 standard and the final strongbacks will be surveyed and inspected according to that standard. We are hopeful that the inspections will be done by the vendor, but we also have the capabilities at LBL if they are needed.

After gluing the padplanes to the strongbacks, the padplanes will be surveyed in the LBL shops to a relative accuracy of  $\pm 5 \mu\text{m}$ . The survey will be conducted for flatness and position of the pads.

The MWPC's will be fabricated at Shandong University (see Section 9) where we have facilities to survey the wires for tension and location to a relative accuracy of  $\pm 5 \mu\text{m}$ .

We are fortunate that the previous TPC project created a long list of QA inspection travelers for use during the fabrication of the original sectors. We will use this traveler system and extend it where required. See Table 7 and Figure 58.



Traveler #	Description	Refers to ...
S-00	ABDB Burn-In & Electronics inspection	..
S-01	Padplane PC board visual inspection	ANSI/IPC-A-600D
S-02	Padplane PC board leak check	..
S-03	Padplane PC Board Dimensional Check	24A446
S-04	Padplane PC board Resistance and Continuity	..
S-05	Strongback Machining Dimensional Check	24A428, 24A392
S-06	Padplane / Strongback Dimensional Check (after bonding)	24A381
S-10	Shield Wire Mount, Right - QA check	24A397, 24A387
S-11	Shield Wire Mount, Left - QA check	24A398, 24A388
S-12	Gated Grid Wire Mount, Right - QA check	24A400, 24A391
S-14	Shield Wire Mount PC Board, Right - QA check	24A450, 24A109
S-15	Shield Wire Mount Insulator Board, Left - QA check	24A403, 24A383
S-16	Gated Grid Wire Mount PC Board, Right, Dimension, Resistance and Bromine check	24A450, 24A353
S-17	Gated Grid Wire Mount PC Board, Left, Dimension, Resistance and Bromine check	24A403, 24A383
S-18	Shield Wire Mount PC Board, Right, Dimension, Continuity and Resistance check	24A455, 24A449
S-19	Shield Wire Mount Assembly, Left, Dimensional check	24A456, 24A448
S-20	Gated Grid Wire Mount, Right , Dimension, Continuity and Resistance check	24A457, 24A461
S-21	Gated Grid Wire Mount, Left, Dimensional Check	24A458, 24A460
S-22	Shield and Gated Grid Pinning, Marking and Dimensional Check	24A453, 24A454
S-25	Anode Wire Frame Visual Inspection and Tension Test	..
S-26	Anode Wire Frame, Prior to use check and visual inspection	..
S-27	Anode wires check	..
S-29	Shield Wire and Gated Grid Wire Frame visual inspection and tension test	..
S-30	Shield Wire and Gated Grid Wire Frame prior to use visual inspection check	..
S-34A	Bromine Check, ABDB, LOAB-OSOR, LOAB-OSIR	meet IPC_A_600D and ANSI/IPC-A-610A
S-34B	ABDB, LOAB-OSOR & LOAB-OSIR Burn-in	Refers to Traveler 08
S-35	Shield Wire Termination Board - Bromine check and Continuity test	24A106, also test with Canary chamber
S-35A	Shield Wire Termination Board - Bromine check	meet IPC_A_600D and ANSI/IPC-A-610A
S-35B	Shield Wire Termination Board - Resistance and Continuity test	24A354
S-36A	Gated Grid Connection Board - Bromine check	meet IPC_A_600D and ANSI/IPC-A-610A
S-36B	Gated Grid Connection Board - Visual inspection and Continuity test	24A4521 L-1

Table 7: A list of QA travelers for the original TPC Project. The documents refer to the design drawings as well as to various ANSI specifications, and these references are indicated in the right hand column.

## TRAVELER S-12

NOTE: This is a Batch traveler

注意：这是一个批处理检验文档。

### GATED GRID WIRE MOUNT, RIGHT – Q.A. CHECK

#### 右侧门丝落丝件，Q.A.检验

GATED GRID WIRE MOUNT RIGHT, INNER SECTOR, dwg # 24A4004

右侧门丝落丝件，内扇区， dwg # 24A4004

总计：\_\_\_\_/每个

GATED GRID WIRE MOUNT RIGHT, OUTER SECTOR, dwg # 24A3914

右侧门丝落丝件，外扇区， dwg # 24A3914

总计：\_\_\_\_/每个

J.O.#: \_\_\_\_\_

J.O.date: \_\_\_\_/\_\_\_\_/201\_\_

After answering each of the following questions please initial your name.

完成下列检查后请签名。

### CERTIFICATION CONFIRMATION

#### 认证确认

5. Dose each part in this batch conform to the dimensions and tolerances of it's drawing, as verified by the LBL inspection department?

是否这个综合检验的每个部分都经过 LBL 检验部门的确认，符合各自的尺度及公差要求？

Yes\_\_\_\_, No\_\_\_\_

IF THE ANSWER TO QUESTION 1 ABOVE IS NO BAG AND TAG BOARDS with "NO CERTIFICATION" AND NOTIFY COGNIZANT ENGINEER

如果上述问题 1 的答案是 NO 收起并把板打上“未通过检验”的标签，同时通知相关的工程师

### VISUAL INSPECTION

Sep.2015

CHI YANG

TRAVELER S-10~S-36

Figure 58: A sample page for one of the translated traveler documents.

## 7.5 The radiation length budget for the iTPC strongback

Figure 59 shows a GEANT based analysis of the original inner sector design. The figure shows the material budget as seen by a particle which starts at the interaction point and leaves the TPC by passing out through one of the inner sectors (i.e.  $1.3 < |\eta| < 2.0$ ). The material budget ranges from a few percent of a radiation length to 35% of a radiation length. The highest peaks in the figure are due to the ribs on the backside of the strongback. The valleys are the cutouts in the face of the Al sector for the electronics. The most commonly occurring value in the fiducial volume is  $\sim 13\%$  radiation length. This number is the sum of the thickness of the Al on the front face of the strongback ( $\sim 10.5\%$ ) plus the G10 backplane ( $\sim 0.5\%$ ) plus a small trajectory angle (i.e. not perpendicular incidence). Note, however, that the electronics, cables and cooling manifolds are not included in these simulations and so, for example, the minimum radiation length holes in Figure 59 will be filled with FEE card electronics which are as thick as the aluminum that they displace.

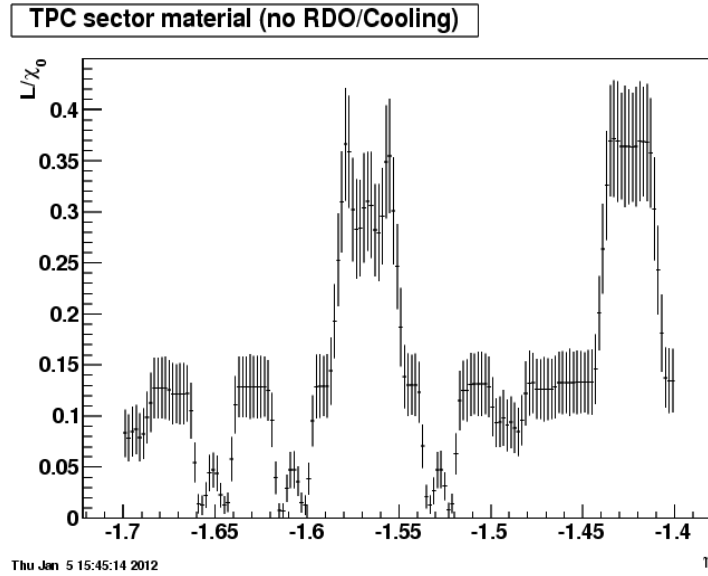


Figure 59: Radiation length vs. pseudorapidity for the original strongback. Electronics, cables and cooling manifolds are not included in these calculations. The lowest points are the cutouts for the electronics and so these numbers are not representative of the final assembly because this is where the FEE cards will sit and their *average* thickness is greater than 7%.

A different perspective on the radiation length budget can be seen by looking at the *average* radiation lengths (not the lumpy distribution) over the fiducial area of the inner sector. Table 8 shows the radiation length budget for the mechanical and electrical components on an inner sector but averaged over the range from  $1.5 < |\eta| < 2.0$  and  $-10 < \phi < 10$  degrees. Note that the average thickness of the Al on the front face of the sector drops from 10.5% to 3.2% due to the large number of holes in the Al face for the electronics feedthroughs.



FEE	3.60 %
FEE mounting bracket	3.45 %
FEE rib	0.45 %
FEE socket	0.15 %
Cooling manifold	3.25 %
RDO card	0.90 %
Ribs	2.70 %
Sector G10	0.45 %
Sector Aluminum	3.20 %
Cables	~1% (estimate)
<b>FEE sub Total</b>	<b>7.65%</b>
<b>Total</b>	<b>19.15%</b>

Table 8: The *average* radiation length budget for the components associated with a TPC inner sector (circa 1993) averaged over the fiducial volume of the sector. The average takes out the lumps in the mass distribution, but also illustrates how the budget for the aluminum on the front face compares to the electronics and cooling budget. The sector data have been averaged over a range from  $1.5 < |\eta| < 2.0$  and  $-10 < \phi < 10$  degrees. Geant simulations courtesy of Irakli Chakaberia.

## 8 MWPC Engineering and Construction

### 8.1 Granite tables & combs to align the wires

The strongbacks will be bonded to the padplanes on a flat granite table. Grade “A” inspection plates are commonly available and flat to within 10  $\mu\text{m}$ . See Figure 60. The bonding procedure is to lay the padplane on the granite table face down, suck it flat with a vacuum source and apply glue to the backside. Finally, the strongback is laid on top of the padplane and the whole assembly allowed to cure, in place, for 48 hours. Once the glue has dried, the strongback is flipped over and the padplane trimmed to match the dimensions of the Al strongback.

The most difficult part of the operation is to align the pads on the padplane with the central axes of the sector to better than 100  $\mu\text{m}$  (50  $\mu\text{m}$  desired). This will be accomplished by using special tools and precision alignment holes and targets on the padplane.



Figure 60: A typical Grade A inspection plate (otherwise known as a granite table). Typical dimensions are 6 feet by 4 feet by 8 inches, although the tables are available in many different sizes.

The granite tables have two high precision tooling balls drilled and mounted on the top surface. The locations of the tooling balls are shown in Figure 61. One tooling ball is located top dead-center and the other tooling ball lies between the photographers toes. The tooling balls are used to locate a set of precision tools that help align the padplane with the strongback while the gluing the two pieces together.

When the glue is dry the strongback is turned over, laid face-up on the table, the PCB is trimmed to size as mentioned previously, and the MWPC wires strung over the padplane. When the strongback is turned over, the brass bushings on the backside will fit snugly over the tooling balls. The fit is designed to be accurate and reproducible so the wires lie in the same location, with respect to the pads, on every sector.

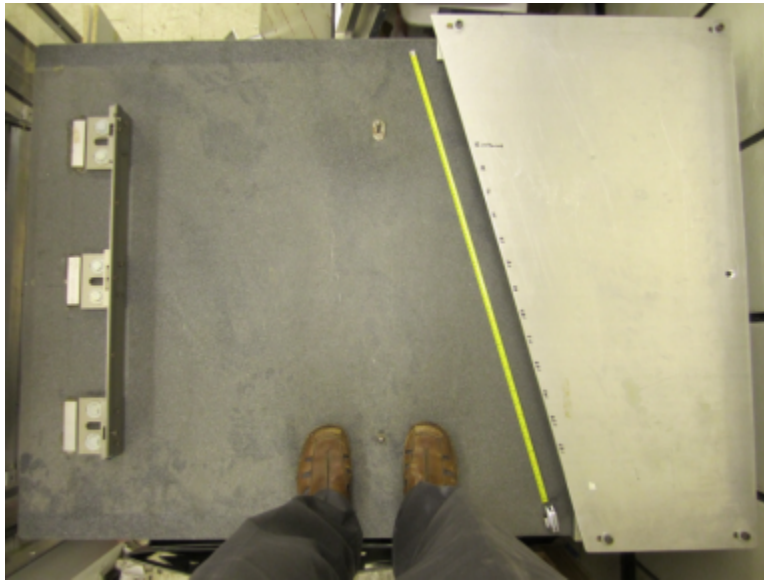


Figure 61: Top view of a granite table with one of the wire alignment combs exposed. The second comb lies under the aluminum shield on the right. Scale: the yellow portion of the tape is 1 meter long.

The alignment of the wires is ensured by the use of a precision set of wire combs which have a fixed location with respect to the tooling balls; see Figure 62. The teeth on the comb are designed to receive one wire, each. Every tooth in the comb is used to hold a wire for the Gated Grid or ground planes, while every fourth tooth is used to align the wires on the anode plane.

The combs are mounted directly on the granite table in a parallel plate assembly which places the comb next to a straight edge. The straight edge is horizontal, flat, and sits at an elevation that is about half way up the height of the combs. The wires that are laid between the combs teeth lie on the straight edge and do not touch the bottom of the comb. Thus, it is the height of the straight edge (not the comb) that determines the elevation of the wires over the padplane. Furthermore, it is possible to shift the wires with a gentle brush stroke so that they lie in the square corners defined by the straight edge and the vertical edge of the teeth. This is a simple and reliable way to align the wires with extremely good precision. It is also a mechanism that is easy to keep clean.

If only one granite table is used during the fabrication of the wires planes, then the height of the straight edge will have to be adjusted for each grid layer (anode, ground and gated grid). Alternatively, three granite tables can be set up with one table devoted to the fabrication of the anode grids, another for the ground plane, and the last table for the Gated Grid.

Once the wire grids have been assembled on the strongbacks, then the sectors are ready for QA, testing and installation in the TPC.

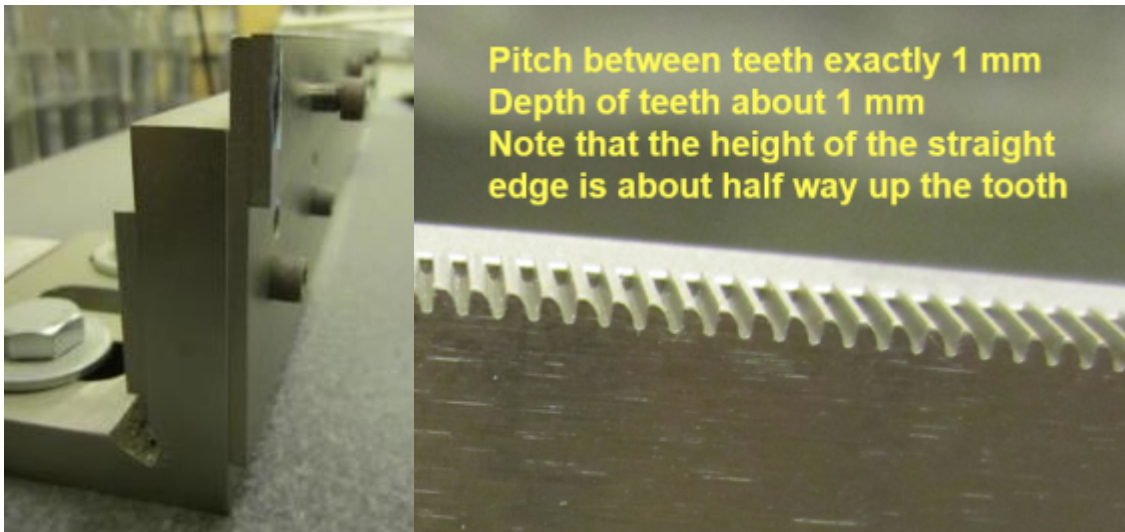


Figure 62: A wire comb mounted on the granite table in shown in the left hand figure. The “comb” is actually composed of two pieces; the comb and a straight edge. The figure on the right shows a close-up photo of the comb. The straight edge lies behind the comb and is located about half way up the teeth. The wires are aligned by being pushed into the corner defined by the intersection of the straightedge with the vertical sides of the comb.

## 8.2 A small factory will be required

Fabricating the new MWPCs will be a substantial task, and a small factory will be required. For example, when the MWPCs were originally built in Berkeley (circa 1995) we had 6 granite tables working in two separate production lines to produce all of the necessary chambers. (See Figure 63.) Three granite tables are required to produce one MWPC. One table for each wire grid layer and there are three layers (anode wires, cathode (or shield) wires, and the gated grid). Multiple tables are necessary in order to speed up the assembly line. For example, while the epoxy is drying on the anode wire plane for the first chamber, the technical team can go to the next table and start stringing the cathode wires on a second chamber which has previously been prepared with anode wires. In Berkeley, there were two teams working simultaneously (6 tables) because we had to produce both the inner and outer sectors (48 total). The new MWPC construction task will be somewhat reduced in scope because now we will only be fabricating the inner sectors (24+spares) and so a 3 table assembly line should be sufficient. We propose to do this work, and to test the MWPCs, at Shandong University in China.



Figure 63: Outer sector MWPCs under construction in Berkeley (circa 1995).



## 9 Facilities at Shandong University

A Detector Laboratory especially for TGC (Thin Gap Chamber) detector construction was built at Shandong University in 1999. Ten percent of the TGC detectors (400 in total) in the MUON End-Cap Trigger for the ATLAS experiment were constructed in this lab. The high-energy physics group of Shandong University also participated in the test and installation of the TGC at ATLAS, and the success rate for the detectors constructed at Shandong University was very high. Failures were negligible after more than three years of running. Each TGC detector contains pads, wires and strip readout, and the structure and technology for these detectors is quite similar to the MWPCs for the STAR TPC. After the TGC construction was completed, the group has continued with research on how to upgrade the TGCs in ATLAS while maintaining the techniques and training for the engineers. Now most of the equipment in the lab is available and in good condition. The entire space in the laboratory (450 feet<sup>2</sup>) is available for the iTPC project. In addition, we have a new laboratory of about 220 feet<sup>2</sup> which was made available after the SDU Physics Department moved into a new building. A new clean room of about 33 feet<sup>2</sup> was built last year specifically for the STAR iTPC project (see Figure 64). It was designed and built especially for work on gas detectors.



Figure 64: Experimental hall with two granite tables (left) and clean room with crane and granite table (right) for MWPC production at SDU.

A wire-winding machine was recently imported from Israel (see Figure 65, left), and the control system was updated last year. The wires for a STAR TPC prototype chamber were wound on this machine. The wire tension was verified using an optical system which measures the resonance frequency of the wire (see Figure 65, right). A similar technique was used in the original STAR MWPC construction project. At Shandong, we also designed an automated system for making tension measurements on a large grid of wires. The system is able to scan the whole wire frame wire by wire automatically and to determine the tension on each wire with a gas jet within 1~2 minutes for each wire.



Figure 65: The wire winding machine at SDU (left) and the optical system for making wire tension measurements (right).

### 9.1 Prototyping capabilities

A small size MWPC prototype chamber (50 x 50 x 10 cm) was built in the laboratory at SDU in the early part of 2014 (see Figure 66). The padplane (12 cm x 12 cm) has 8 rows of pads (22 pads per row) and the pad size is the same as the one designed for the iTPC (5 mm x 16 mm). There are three layers of wires above the padplane; the anode wires (20  $\mu\text{m}$  Au wire), the shield wires (75  $\mu\text{m}$  BeCu wire), and the gated grid (75  $\mu\text{m}$  BeCu wire). The wire properties are summarized in Table 9. The distances between the padplane, anode wires, shield wires and gated grid are 2 mm, 2 mm, and 6 mm respectively. These dimensions are the same as the current inner TPC sector. The pitch for the anode wires is 4 mm but 1 mm for the shield and gated grid wires. The drift length is limited to 5 cm in this prototype.

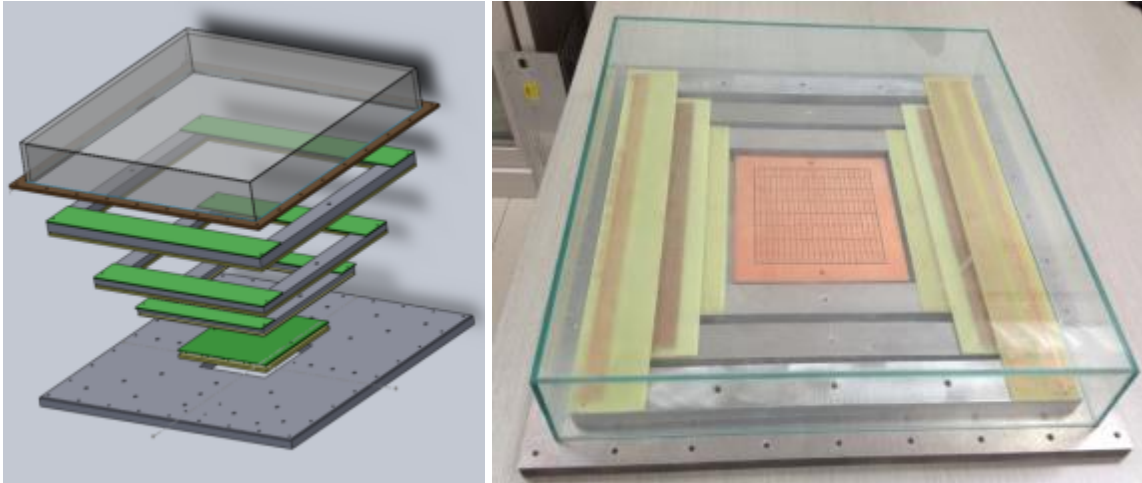


Figure 66: Exploded view and setup for the small scale MWPC prototype.

Wire	Diam. ( $\mu\text{m}$ )	Pitch (mm)	Composition	Tension (N)
Anodes	20	4	Au-plated W	0.50
Anodes— last wire	125	4	Au-plated Be-Cu	0.50
Ground plane	75	1	Au-plated Be-Cu	1.20
Gating grid	75	1	Au-plated Be-Cu	1.20

Table 9: Table of wire properties and tension on each wire for the prototype chamber. These specifications match the parameters used in the original STAR TPC.

### 9.1.1 Test system

The MWPC prototype chamber was studied with cosmic rays (see Figure 67). The cosmic ray test stand used two layers of scintillators as a trigger system and two layers of TGC (Thin Gap Chambers) to determine the position of the incoming muon. The size of the system is 150 x 150 x 380 cm. Since the prototype is small (12 x 12 cm area covered with pads), the effective trigger area is only  $\sim 1\%$  of the total system, but acceptable for our preliminary tests.

For the readout, we used readily available electronics, one V550A plus two GassiPlex07 cards as readout. Currently there is no time information, so we only measured the charge signal from the pads. We plan to use the same DAQ electronics as the STAR TPC in a later stage of the tests.



Figure 67: The cosmic ray test stand at SDU and associated test equipment.

The measurements were done using P10 gas (90% Argon + 10% Methane) in the chamber. The leakage current was monitored during the measurement and the noise and sparks were well under control. The charge signals were read out from 4 rows, 88 pads in total, and the pad numbering is as shown in Figure 68. The pedestal and signal were



measured for each pad (see Figure 69). On these plots, 3 ADC counts corresponds to 1 fC. The voltage was 1350 V for these tests and no drift field was applied. The signal was defined to be  $5\sigma$  away from the pedestal. We then summed all the signals from the pads, after subtracting the pedestal, to yield a rough estimate for the gain. The right panel in Figure 69 clearly shows the signal with a Gaussian peak around 394 ADC counts, or about  $6.6 \times 10^6$  electrons.

Since there was no drift field applied across the chamber, it is difficult to calculate the gain but we can estimate that the effective length of a track collected by one wire is 4 mm. We estimate that the gain is  $\sim 3.7 \times 10^4$  at 1350V. Of course, a detailed study of the effects from noise should be performed to get a more reasonable value. The gain value with this setup measured with  $\text{Fe}^{55}$  mentioned in Ref. [1, 2] is  $\sim 4 \times 10^4$ , but is 20-30% below the actual value due to a relatively short peaking time. So, our rough gain before removing noise is consistent with the value in Ref. [1, 2]. We are planning to do a better measurement on the gain and also with timing information.

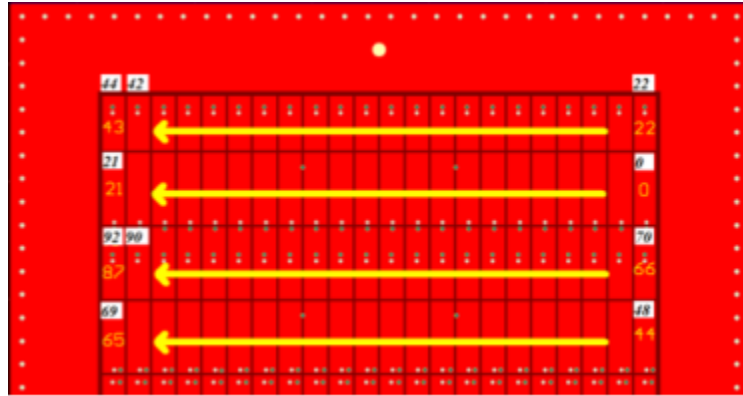


Figure 68: Pad numbering scheme for the small MWPC prototype.

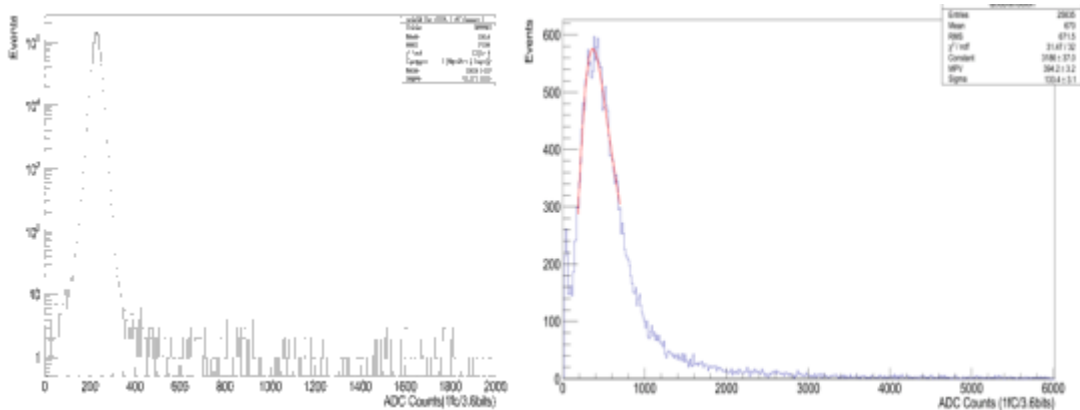


Figure 69: The pedestal measured on one pad at 1350 V (left) and the summed signal from all pads after pedestal subtraction (right).

### 9.1.2 New test system with STAR DAQ system

In early 2015, some elements of the STAR TPC DAQ system were shipped to SDU. Based on these DAQ elements and local equipment, a DAQ system with the same elements that STAR is using currently has been set up. This system is intended for the local detector test after each iTPC MWPC module is produced. Now this system is used to test the small MWPC prototype mentioned above. A layout of the test system is shown in Figure 70.

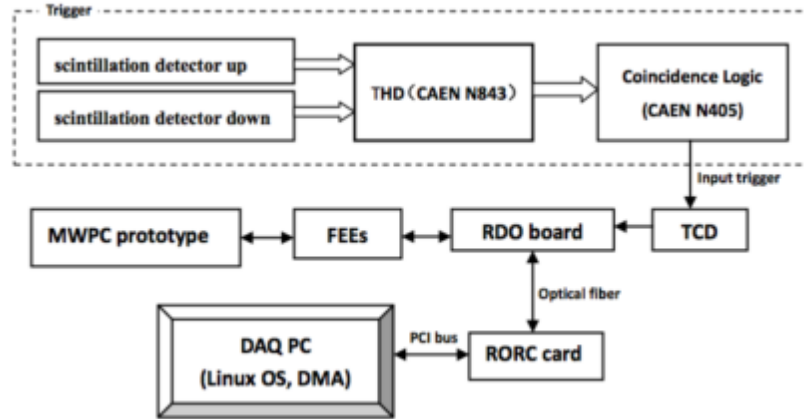


Figure 70: Layout of the MWPC prototype test system.

The coincidence between two layers of scintillator-detectors (scintillator+PMT) is used as a trigger signal when cosmic-rays pass through. The calibrations of these scintillator+PMT detectors have been done. Figure 71 shows their SPE spectra while Figure 72 shows the anode output charge as a function of high voltage of PMT. To meet the gain  $1.0 \times 10^6$ , two PMTs are operated in -1108V and -1073V, respectively.

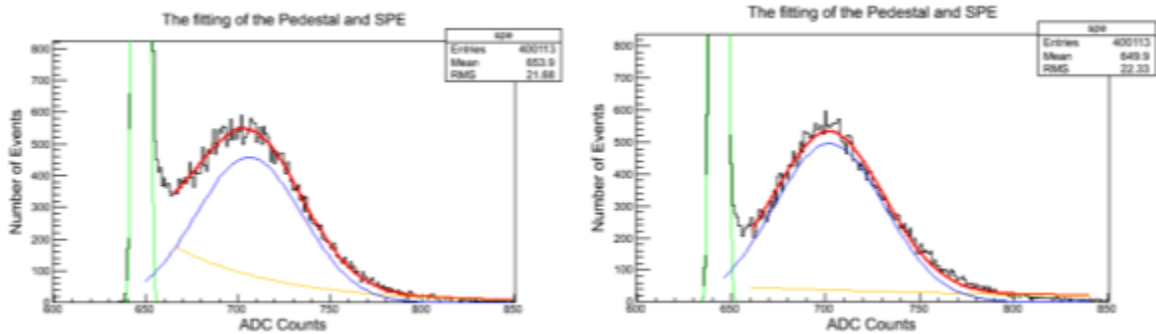


Figure 71: the SPE spectrum of Hamamatsu R11102-A52468(left) and R11102-A52723(right)

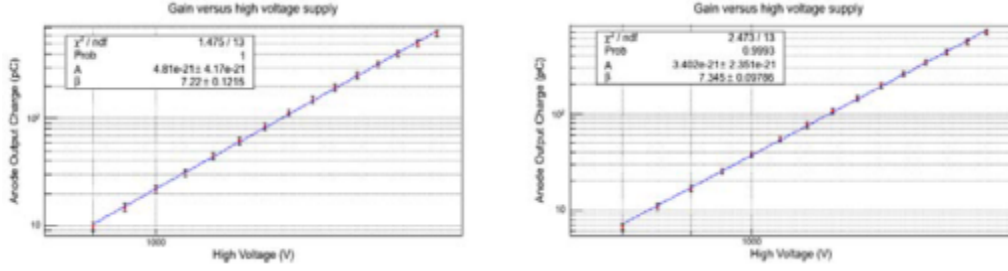


Figure 72: the anode output charge versus high voltage supply of Hamamatsu R11102-A52468 (left) and R11102-A52723 (right).

To debug this DAQ system, a pedestal run was taken with a random trigger. Figure 73 (left panel) shows the connection between small prototype and DAQ elements while Figure 73 (right panel) shows the ADC value versus the time-bin number. The full system, which includes prototype, trigger system, DAQ system and supporting structure, are being assembled.

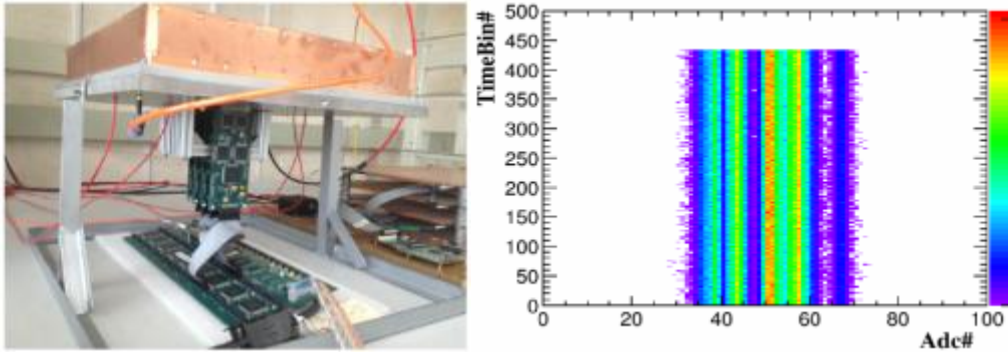


Figure 73: (Left): the connection between small prototype, FEEs and RDO board. (Right): the ADC value versus the time bin number

## 9.2 MWPC production capabilities

The wires for the 24 inner TPC sectors will be wound on temporary wire-transfer frames. The winding machine will control the wire pitch and tension. The transfer frame itself is a welded aluminum box, as can be seen from the design drawing in Figure 74 and Figure 75. Solid aluminum bars are bolted onto the ends and these bars are used to establish the straight edges that form the wire plane. The bars will be anodized to harden the surface so that epoxy can be removed without damaging the surface. The bars are positioned to hold the wires above the surface of the box beam frame and parallel to the surface that the frame is resting on. Wires will only be glued on one side of the frame, so two frames can be wound at the same time on the winding machine (one on either side of the rotating table). Twelve wire frames will be used to carry the wires so that a set of transfer frames will only need to be wound for every four sectors. Ten such frames have been made. A gluing robot (see Figure 76) was also been designed to dispense epoxy on the edge (3mm wide) of holding wire on wire frames and also later on side wire mounts.



Figure 74: A sketch of the temporary wire transfer frame. The inner size for the box is 76.2 x 90.0 cm and the size of the material is 3.0 x 6.0 x 0.3 cm.

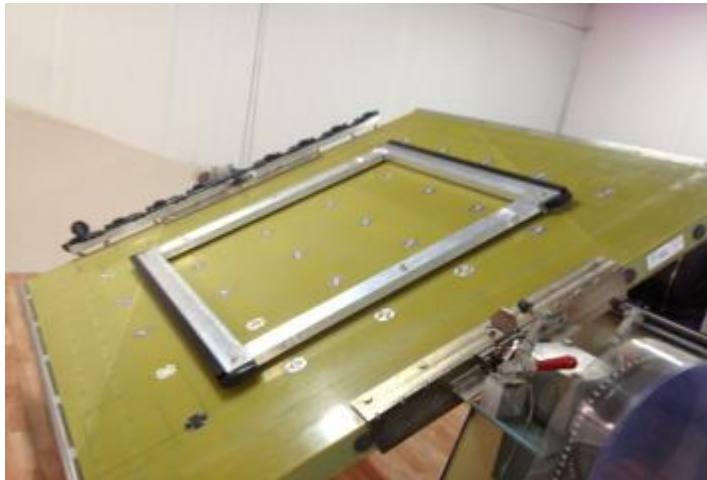


Figure 75: Wire winding on the first two wire planes with 20um W-wire.

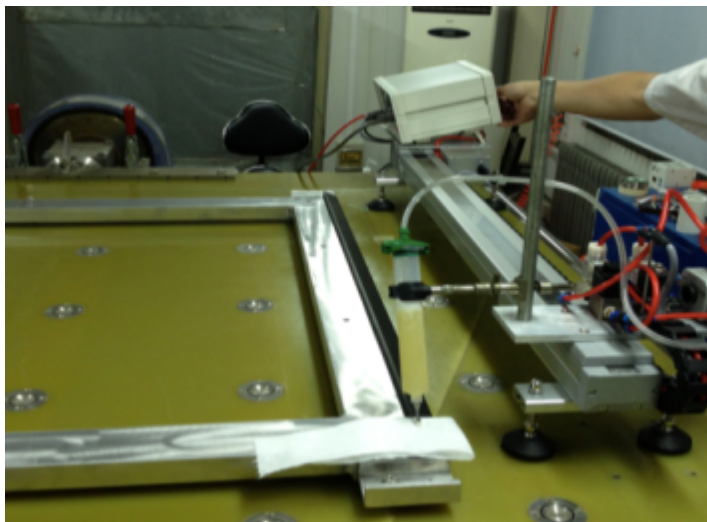


Figure 76: Gluing robot for dispensing epoxy on thin edges

The assembly of the MWPCs will be done at SDU using strongbacks produced by the University of Texas at Austin and padplanes produced by BNL. Additional small components will be fabricated at SDU. An initial round of QA and testing will be conducted at SDU before shipping the chambers to BNL for final test and installation. For example, the whole sector will be tested with P10 gas, HV and readout electronics to see an  $\text{Fe}^{55}$  signal on all pads and to verify uniformity across all channels.

The full size MWPCs will be produced using techniques that are similar to those used during the construction of the original TPC. There are several steps to make the MWPC's.

A brief list is given here:

- i) Epoxy the padplane to the strongback, using Epoxy made of Epon 826 and Versamid 140 in a ratio of 60/40. The epoxy will be supplied by E.V. Roberts. That is the same glue that was used in original TPC construction.
- ii) Use a special PPPCB trimming router to ensure that the padplane PCB edges are flush with the strongback. Then the sector goes to the Machine Shop for cutting the O-ring groove and machining the sector to the finished height.
- iii) Epoxy the anode wire mounts to the strongback. Then pot the anode signal feed-through boards.
- iv) Use the wire combs on the granite table to lay down the wire plane onto the wire mounts to get the right pitch for each layer of wire, and then epoxy and solder the anode wires.
- v) Attach the shield and gated grid wire mounts to the strongback.
- vi) Epoxy and solder the shield wires using wires from the previously produced wire-transfer frames.
- vii) Epoxy and solder the gated wires using wires from the previously produced wire-transfer frames.
- viii) QA, test & inspection
- ix) After the tests are complete, the sector will be transferred to a hermetic box with constant  $\text{N}_2$  flowing until shipment to BNL for final test and installation.

#### *9.2.1 Progress on a full size prototype at SDU (since late 2014):*

We started to work with a full size iTPC prototype at SDU in November 2014. A set of PCB pad planes plus anode, shield, and gated wire mounts based on previous STAR drawings was produced by a factory in China. For the purpose of practicing a complete

procedure of MWPC prototyping and assembly at SDU, an Aluminum strongback produced by U. Texas was sent to SDU in Oct. 2014 for the prototyping studies.

#### 1) Gluing pad plane to the strongback

The same epoxy recipe, as compared to the 1995 work, was used: 60% Epon 826 + 40% Versamid 140 by weight, purchased from EV. Robert. The size of the pad plane was made 0.1mm smaller than those of the strongback, so the trimming of pad plane was not done for this prototype. This is a minor variation on the procedures originally used in 1995. See Figure 77 and Figure 78.



Figure 77: Padplane on granite table held flat by the suction of a vacuum system.

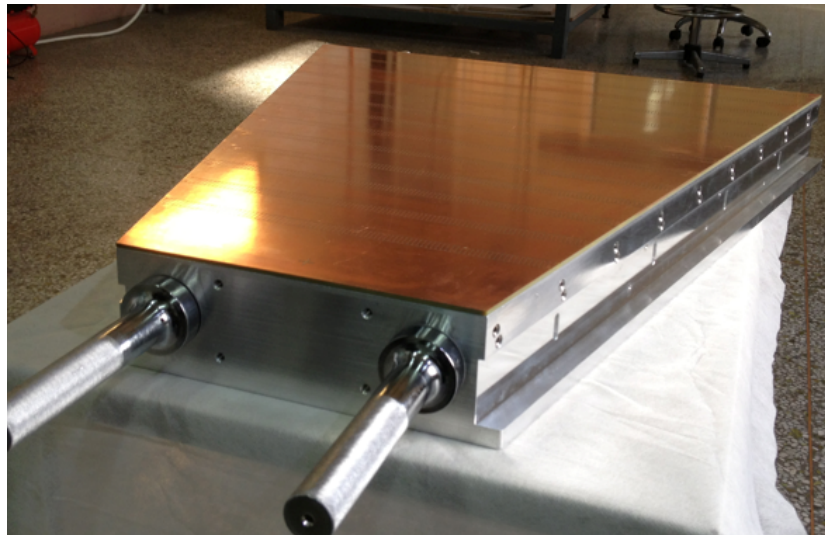


Figure 78: The strongback with the pad plane glued in place.



## 2) Epoxying the anode wire mounts

A gluing stand was made for the purpose of gluing the anode wire mounts to the strongback. After dispensing epoxy to the wire mounts and along the side edge of the strongback, the wire mounts were attached to the strongback with bolts and clamps. Next, the strongback was put on 1.85mm spacers on the granite table with the pad plane side down. The gap between the wire mounts and the table was kept smaller than 0.05 mm while tightening the bolts. See Figure 79 and Figure 80.



Figure 79: Gluing stand for anode wire mount and granite table.



Figure 80: The anode wire mounts were glued to the strongback with epoxy..

## 3) Attaching the shield and gated wire mounts:

The shield and gated wire mounts were attached by putting the strongback pad-side down using spacers with a standard height over the granite table of 3.85mm for the shield wire

mount and 9.85mm for the gated wire mounts. The bolts were tightened while keeping the wire mounts resting on the granite table with a gap smaller than 0.05 mm. See Figure 81 and Figure 82.



Figure 81: Attaching shield & gated wire mounts to strongback

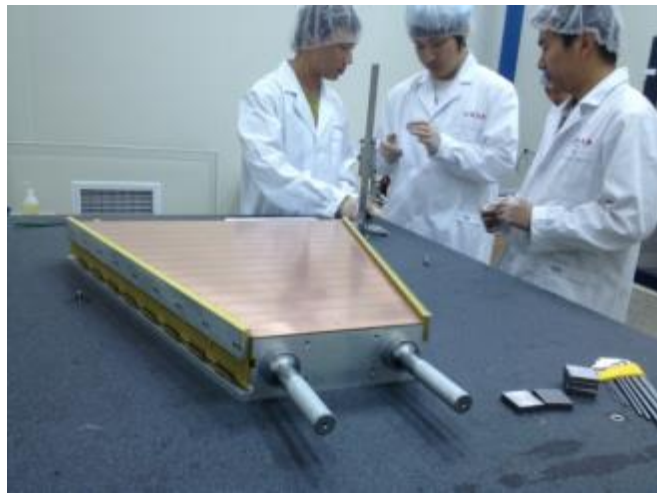


Figure 82: Strongback with all three side wire mounts attached before drilling/pinning.

#### 4) Drill/pinning fixture

A drill fixture was constructed to drill three alignment holes in the wire mount and attach them using a tapered pin. A #5 American standard tapered pin was used and we practiced drilling and pinning the wiremount to the strongback. See Figure 83 and Figure 84.





Figure 83: The drill/pinning fixture designed at SDU



Figure 84: Drilling & pinning the side wire mounts

## 5) Mounting the wire combs

We reproduced a set of wire combs, locally, and checked the pitch using a laser system. It was found that the precision of the pitch is about 14 $\mu$ m, which is not good enough. We received the original set of combs from Berkeley lab in early August. Checking with view machine and laser system, the precision of the wire pitch is about 5 $\mu$ m, which was very good. The flatness of the straight edge on which the wire will rest on, needs to be less than 10 $\mu$ m and we confirmed this with deliberate measurements. See Figure 85. While installing the straight edge, a set of height standards with a precision of 10  $\mu$ m were used to make sure the height of the straight edge is 2 mm higher than that of the pad plane.

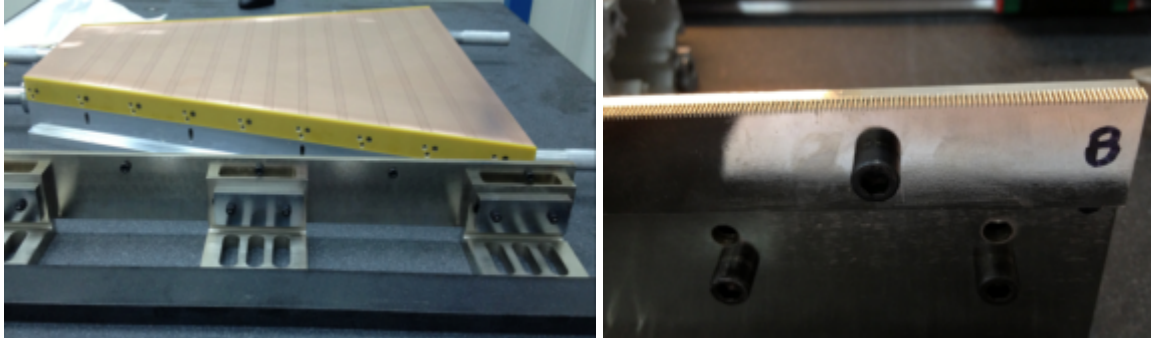


Figure 85: One side the wire combs installed including angle plates, straight edge and combs (left), and a zoomed view for the combs and straight edge..

#### 6) Epoxying the anode wires to the wire mounts

The wire frame was mounted on four height-adjustable spacers with a precision about 20  $\mu\text{m}$ . The spacers were put on two parallel rails, so the wire frame can be shifted in the direction vertical to the wire direction, as shown in Figure 86. The wires were allowed to touch the straight edge slightly and rest on the vertical edge of the combs. Then epoxy was dispensed along the top edge of the anode wire mounts using a glue robot. After curing for 40 hours, the wires were cut but leaving an additional 3 cm tail after the glue points. See Figure 87.

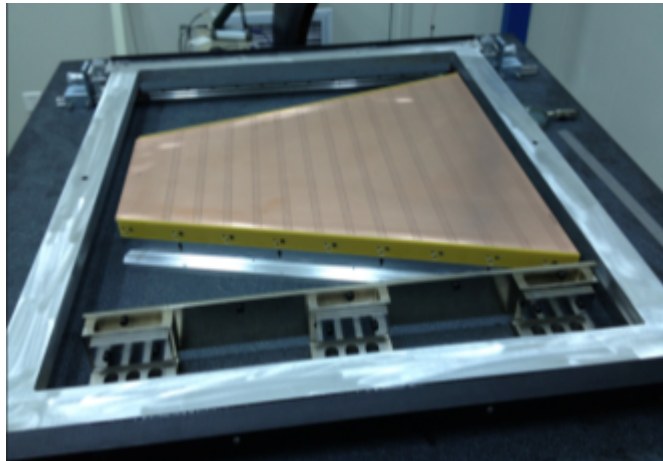


Figure 86: Putting the wire frame on the wire combs

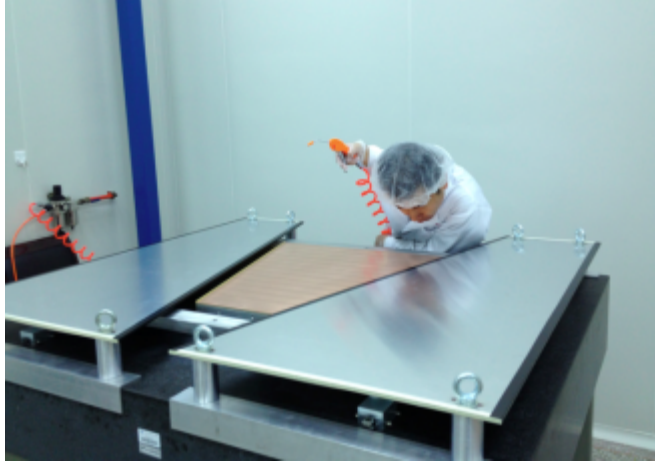


Figure 87: Epoxying the anode wires on the wire mounts with protecting covers in place.

#### 7) Soldering anode wires

Each anode wire was carefully soldered on the corresponding copper line. The soldering time should be short to prevent removing the gold plating on the wire. This operation needs practice and an experienced technician. Two rounds of quality control checks were made to ensure that each wire was properly soldered. Then we checked the continuity for each wire. We are designing a more convenient soldering stand for this operation for the production run.

#### 8) Plan for next steps: epoxy and solder shield & gated grid wire plane on wire mounts

We are preparing to wind the shield & gated grid wire planes. We have received four sets of wire combs from LBL, which will be used for putting wire planes on each the respective wire mounts.

### 9.3 QA plan and Travelers

The original QA plan, with detailed flow chart and most of the related travelers (90%), have been found. In the previous TPC MWPC fabrication, every step corresponds to a QA traveler. Each traveler consists of a detailed check list. Most of these travelers related to MWPC production have been recovered. They have also been translated into Chinese with English version comparison bullet by bullet. After a bit more review, these QA travelers will be used in MWPC fabrication and test processes at Shandong.

### 9.4 References

- [1] STAR TPC NIM, M. Anderson et al., Nucl. Instrum. Meth. A 499, 659 (2003).
- [2] Wayne Betts, "Studies of Several Wire and Pad Configurations for the STAR TPC", Thesis UT Austin, STAR Note SN0263.

## 10 Electronics and Data Acquisition for the iTPC

The iTPC upgrade represents a significant increase in the number of necessary electronics channels. The precise count will depend on the final pad and padplane geometry chosen. All geometries under consideration suggest that this will be at least a factor of two increase in the number of channels. In view of this increase we need to redesign the iTPC electronics as well as increase the capacity of the TPC data acquisition system (DAQ).

The electronic components addressed in this chapter are: preamplifier and digitizer ASIC (“SAMPA”), front end electronics cards (“iFEE”), readout boards (“iRDO”), ancillary components, power distribution and the DAQ Upgrade. Many of these components are already undergoing various levels of R&D within the STAR Electronics Group at BNL.

### 10.1 Preamplifier and Digitizer ASIC -- “SAMPA”

The preamplifiers and digitizer ASIC is the most crucial component of the electronics upgrade. The current TPC electronics uses a combination of two ASICs: the PASA (preamplifier/shaper) and the ALTRO (digitizer/storage). Both of these ASICs were developed at CERN for the ALICE TPC and have been successfully used for the STAR “DAQ1000” upgrade for a number of years. However, both of these ASICs are no longer available and thus can no longer be used in the iTPC upgrade.

At this time the ALICE Collaboration is also planning to upgrade the electronics for their experiment. They have started a design effort at Sao Paulo University, Brazil with the goal of designing and subsequently producing a new ASIC. This new ASIC, called “SAMPA”, is already under development and the BNL/STAR Electronics Group has been involved in its design, participating in discussions regarding requirements and necessary features of the SAMPA chip. It is worth noting that many of its general features and the programming/setup scheme are very similar to the previous ALTRO chip, thus making its integration into STAR easier since STAR (and the BNL/STAR Electronics Group in particular) has significant experience with the previous electronics.

The SAMPA chip is a 32 channel combination of analog preamplifiers and shapers with the digitalization and storage all in a single silicon die and packaged chip. It represents an integration and modernization of the previous generation PASA+ALTRO with many new and better features:

- 32 channels on a single chip
- smaller overall size
- lower power dissipation
- programmable input polarity, gain and shaping time suitable for both wire and GEM detectors
- fast serial data output

SAMPA will be designed, tested and produced in 2 or 3 stages. The first stage has already been accomplished; it is the so-called “Multi Wafer Prototype 1” (MWP1) where the designers produced 3 silicon dies of the 3 major subcomponents of the final ASIC. 1.) the analog preamplifier/shaper (so called “chip 1”), 2.) just the ADC (so called “chip 2”) and 3.) a 3-channel version of the preamplifier+shaper+ADC+digital manipulation (“chip 3”). These 3 chips have been received from the foundry and are currently undergoing testing. Figure 88 and Figure 89 show the photographs of the MWP1 chips 1 and 3. Note that the packaging is preliminary for these prototypes and does not represent the final choice.

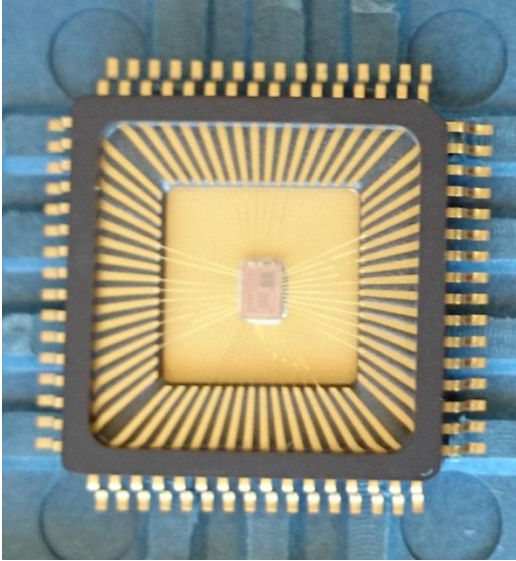


Figure 88: SAMPA MWP1 “chip 1”



Figure 89: SAMPA MWP1 "chip 3"

The critical preamplifier/shaper shows excellent preliminary results while the other 2 chips are still under evaluation by groups in Brazil and other CERN-associated institutions. Figure 90 shows the output signal of the prototype preamplifier/shaper. The shaping time of  $\sim 160$  ns meets our TPC requirement. This very early prototype testing and it is meant mostly for the chip designers so we felt that it would not be necessary for the BNL Group to participate in this early effort.

The next stage, called MWP2 will integrate all the required features and is planned to be a full-scale prototype of the final design. It is hoped that the MWP2 version will be very close in functionality to the required design so that it might even be the final chip. However, enough time and resources were allocated in the design schedule to allow for another version, called MWP3, which would then be the final design.

The BNL/STAR group has an agreement with the chip designers where we will obtain a number of MWP2 samples once they are available (assumed to be June 2016) with which we will commence our own testing in the realistic STAR TPC environment.



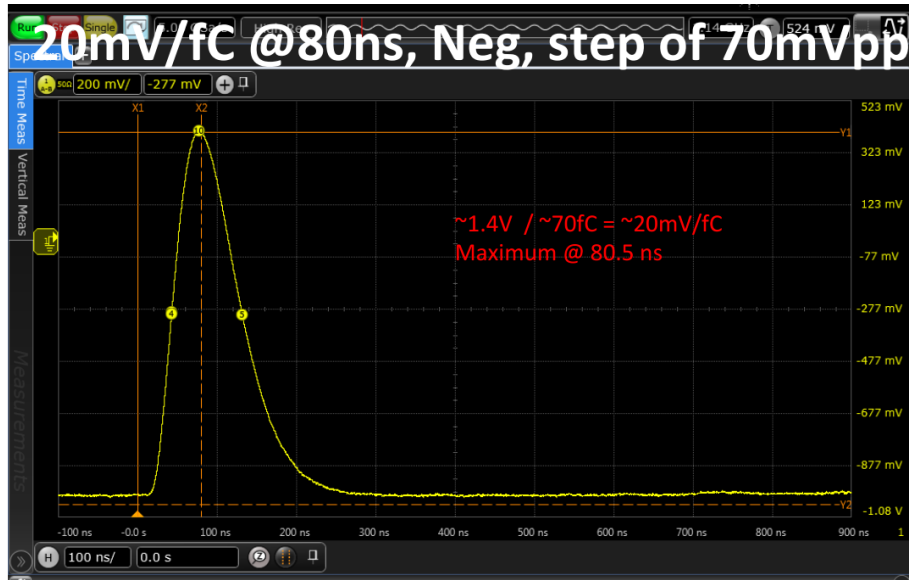


Figure 90: Output signal of the SAMPA preamplifier/shaper. These are preliminary results from the MWP1 "chip 1" evaluation.

## 10.2 Front-end Electronics Cards ("iFEE")

The iFEEs are small printed circuit boards, which connect directly to the pads via the padplane connectors (see Figure 52) and will house the SAMPA ASICs. The iFEE also contains an FPGA, which is the controller that will set various SAMPA operating parameters during the configuration phase. During the data-taking phase, the FPGA will multiplex the data onto a fast serial link towards the Readout Board (see next section). It will also supply the correct regulated voltages to the SAMPA chips as well as the necessary reference voltages for SAMPA's ADC. The power to the FEE is provided via links from the RDO board. The FPGA will be configured over the cable links from the RDO.

We don't yet have the 32-channel SAMPA prototypes so we chose to design and produce a pre-prototype FEE ("ppFEE") card, which has all the other necessary features apart from the actual SAMPA chips. Since we know the major features and protocols of the SAMPA chip this pre-prototype card will serve as an early development platform for most of the VHDL firmware and also includes a simple SAMPA-chip emulator in firmware and parts of the hardware.

The pre-prototype has been produced and the most important features of the card have been evaluated and confirmed: fast serial protocol to the iRDO, remote FPGA configuration, power distribution. The ppFEE is shown in Figure 91. Further firmware development is ongoing.

Once the MWP2 SAMPA chips become available we plan to modify or add the necessary parts to the ppFEE which relate to the actual SAMPA. All other components should stay intact, thus we expect a quick redesign with minimal effort.

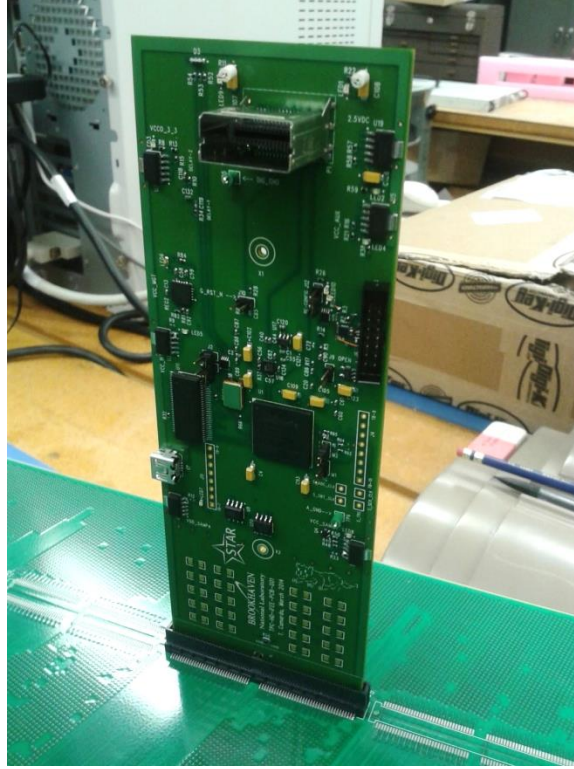


Figure 91: Pre-prototype iFEE (ppFEE) electronic card shown plugged into the padplane

The iFEEs need to be mounted on the TPC Sector in a secure fashion. The mounting structure will also serve as an excellent electronics signal ground and will provide the iFEE electronics with water cooling. To minimize this effort we are currently designing the iFEE to match the existing TPC's cooling and mounting manifolds since we will reuse the actual existing manifolds once we dismount the old TPC sectors during the de-installation phase.

### 10.3 Readout Boards (“iRDO”)

The iRDO is an electronics board, which serves a number of purposes within the electronics chain of the iTPC upgrade. It acts as the multiplexer for the SAMPA data coming from the iFEEs onto the STAR-standard fiber links which connect to the DAQ Sector PCs. It also serves as the STAR trigger and clock interface/control to the iFEE and SAMPA. Finally, it provides power regulation and fan-out from the remote power supplies down to the iFEEs and provides the necessary PROMs for the iFEE FPGA remote configuration.

Similar to the current RDO, these functions will be combined in a single PCB with a larger FPGA. The iRDO will also house commercially available fiber optical interface cards (SIU, Cerntech Ltd). We plan to use fast serial links for the transfer of data from the iFEE to the iRDO thus eliminating the current wide flat cables. This should also lower the overall mass of the new electronics system.

Based upon these requirements as well as the FEE design we designed and produced an iRDO prototype card, which can control 8 iFEEs and has all the other necessary features (see Figure 92). This prototype board is undergoing testing at this time.

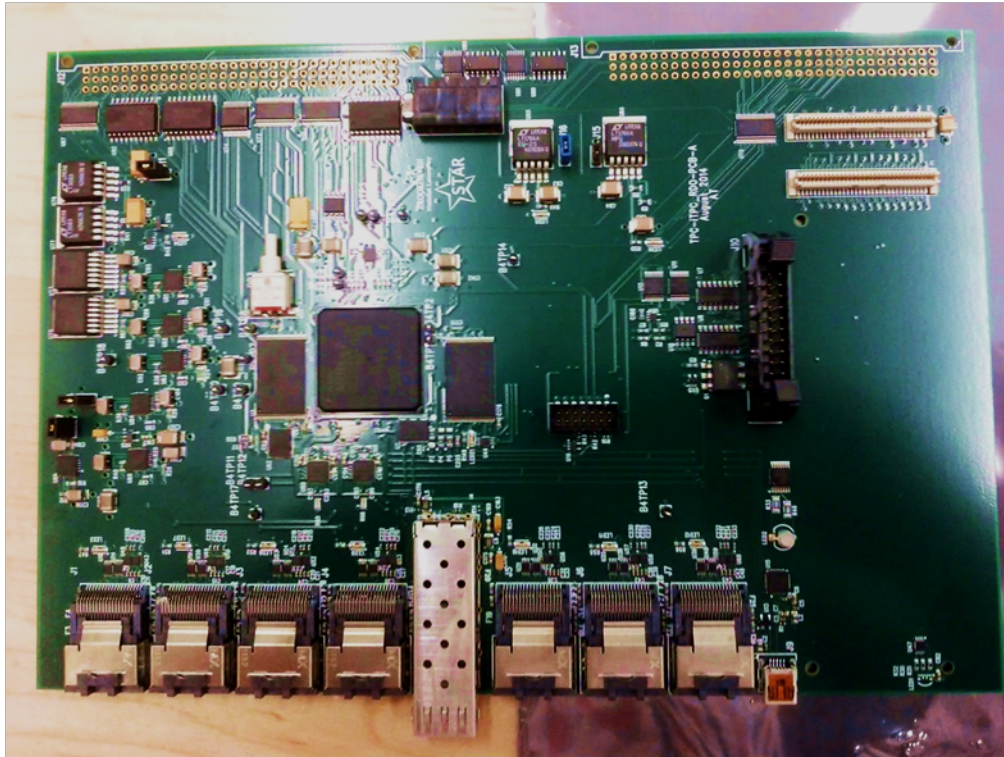


Figure 92: iRDO prototype.

### *10.3.1 Ancillary Connections & Components*

Part of the electronics upgrade for the iTPC will be various small electronics boards and electrical connections, which exist on the strongback and frames of the inner sector. The design of all of these boards is driven by either the MWPC or the mechanical groups. However, the BNL/STAR Electronics Group will provide expertise and will be responsible for the production and testing of these boards.

The anode high voltage wires connect to the MWPC wires via standard HV-type connectors. There are 4 independent connectors per inner sector. Additionally, each wire of the MWPC needs to be grounded via a 50 MOhm resistor. This will be accomplished through a series of small PCB cards mounted on the strongback itself, similar to the current design. The placement of the HV connectors, the routing of the high voltage to the amplification wires as well as the grounding cards is expected to closely mimic the current design.

The “Ground Plane Pulser” is a gain and timing calibration component, which represents a single BNC-type connector connecting the ground wires of the MWPC to an external



pulse generator. We plan to closely mimic the current successful design. There is one such connection per inner sector.

The Gated Grid wires need a connection to the external Gated Grid pulse generators. The connections are accomplished using a connector, which provides the feedthrough from the gated grid wires, via BNC-type connectors to external GG generators. We plan to closely mimic the current design. There is one such connection per inner sector.

#### 10.4 Power Distribution and Power Supplies

In the current TPC power distribution scheme, each RDO (and associated FEE cards) is powered by one dedicated dual-voltage power supply (for analog and digital subsystems of the electronics) located in the TPC Power Supply Racks on the STAR South Platform.

The existing cables (and connectors) with their current and voltage rating are deemed to be sufficient for the new electronics so we plan to reuse them. However, the current power supplies can't provide sufficient power for the new electronics and will need to be either replaced or supplemented. We are investigating two possible approaches:

- *Option A*: replace the current power supplies using a higher power rating
- *Option B*: add 48 additional power supplies

The preferred option is A because we would not need additional space and we could also keep our remote control system intact. We will continue to investigate these options as we gain more experience with the new SAMPA ASIC's power consumption.

#### 10.5 DAQ Backend

To match the increased number of channels we also need to add additional components to the TPC's STAR DAQ system for the twofold increase in data volume from the inner sectors.

We plan to add 2 additional bidirectional fiber links per inner sector for a total of 48 new bidirectional fiber links. There are no particular space constraints but the fibers need to be purchased and installed.

We also need to add 24 more dual-channel Optical Receiver Cards (RORCs) to our current DAQ system. These cards were developed for the ALICE experiment at CERN and are currently in use everywhere in the STAR DAQ system. Each RORC controls 2 bidirectional fiber links. The new RORC cards use the newer PCIe bus interface (as opposed to the older PCI-X interface) but we have already developed the necessary device driver software and these newer boards are already in use in STAR. We plan to procure those cards from the manufacturer (Cerntech Ltd) in this newer PCIe format.

The Processing Units, which hold the RORC cards are standard 3U rack mountable PCs with 8 CPU cores, 4 GB or RAM and small disks with 2 free PCIe slots, which will hold 2 dual-channel RORC cards (for a total of 4 fiber links per PC). The PCs will be

configured in exactly the same way as the current DAQ PCs. The PCs are available off-the-shelf and we need to purchase 12 such devices. We plan to install them next to the current PCs in racks in the STAR “DAQ Room” where there is enough space available.

Since we are increasing the overall TPC data volume by about 30% we will need to purchase and install 2-3 additional DAQ Event Builder PCs. This does not present any issues.

## 11 Sector insertion tool

The inner and outer TPC sectors weigh about 70 and 100 pounds, respectively, are isosceles trapezoids in shape and are fragile. The clearance between sectors is tight ( $< 3$  mm) and the final placement of the sector should be accurate to about  $50\text{ }\mu\text{m}$ . So a dedicated tool is required to install the sectors inside the TPC, *i.e.*, the installation cannot be done by hand.

The original sector-mounting tool shown in Figure 93 was built at LBNL. It has many degrees of freedom and works quite well. However, it was designed to work when the TPC was on the floor and not inside the STAR magnet. Because it is not practical to remove the TPC from the magnet solely for the purpose of the iTPC upgrade, a different approach is required.



Figure 93: The original sector-mounting tool. The sector must fit through the opening in the end-wheel, rotate, and finally pull back into place over a pair of alignment pins (tooling balls) that are located inside the TPC.

Various options for replacing new inner and outer sectors were studied, including a scheme to reuse the old insertion tool. However, we have concluded that the constraints imposed by working with the TPC inside the magnet are so severe that the old tooling cannot be used. For example, when the TPC sits inside the STAR magnet, there is a

recess of 52 inches from the magnet face to the end-wheel, and cable trays etc. add another 14 inches of offset. This creates an issue because the crane which was used to support the original insertion tool cannot access the face of the TPC. Furthermore, if we tried to use the existing tool then it would require nearly 2.5 times its own weight in counterweight to compensate for the load. The TPC end-wheel does not have enough strength (plus safety factor) to handle that load.

A conceptual design for a different TPC sector insertion tool is shown in Figure 94. The design does not rely upon an overhead crane, nor does it place any significant load on the TPC end-wheel. Instead, it will be supported by a platform that will be mounted to the face of the magnet for the duration of the installation procedure, *i.e.*, the platform allows access to all possible sector locations on the end-wheel from its fixed position.

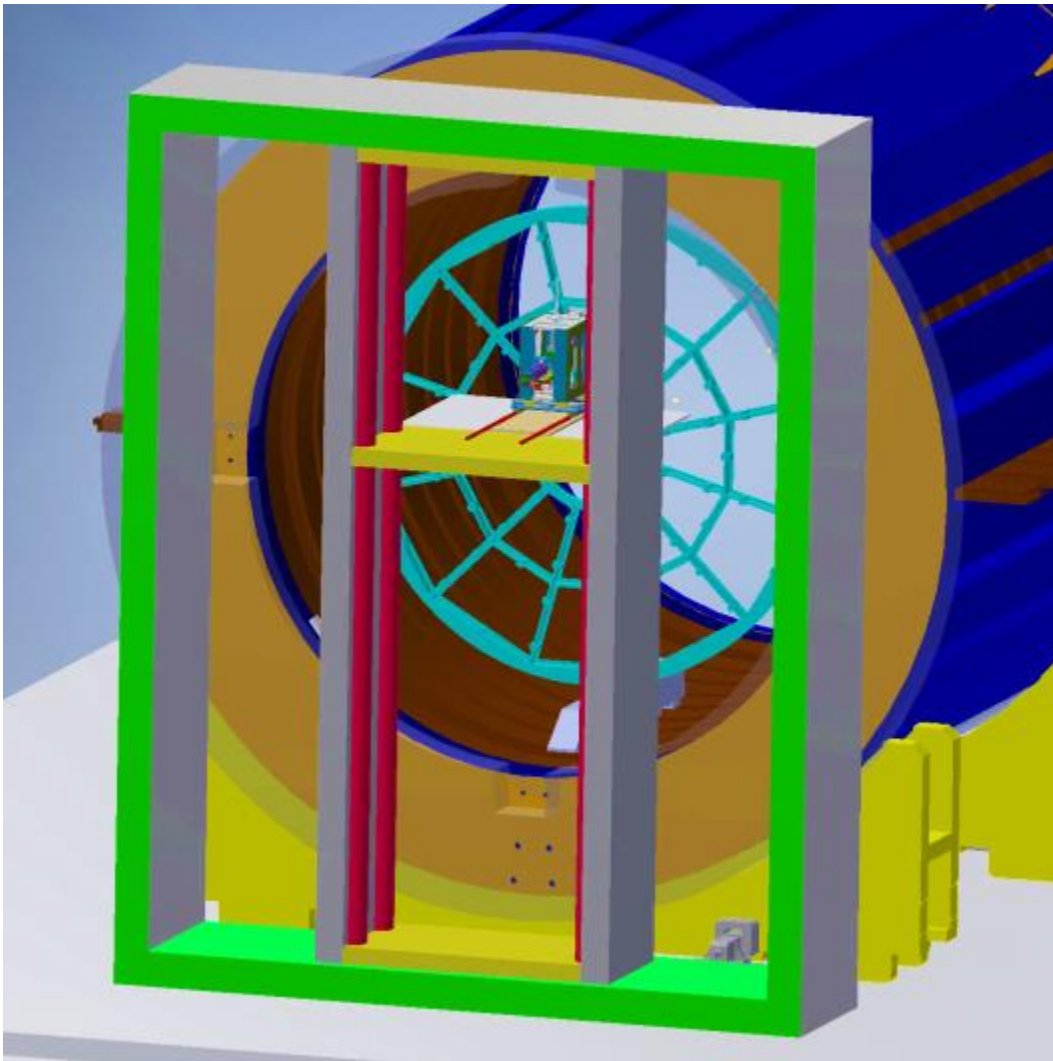


Figure 94: Schematic diagram of the proposed new sector-mounting tool. The green walls are fixed to the magnet face and define the limits of motion in the plane parallel to the TPC end-wheel. The red support columns move horizontally within the green walls and the lift that supports the sector manipulation tool moves vertically on red columns.

The two major components of the sector insertion tool are as follows:

- i) Sector installation platform – It is a movable support structure consisting of a sliding extensions that bring the sector manipulation tool into position for the sector to be installed in the TPC end-wheel.
- ii) Sector manipulation tool – Once in position, the sector manipulation tool will have to do rotations about two axes and translation along one axis in order to install a sector on the TPC end-wheel. The sector manipulation tool will have the required degrees of freedom built-in to achieve the full range of motion required by the installation sequence.

The sector installation platform will be fabricated under contract with Bastian Solutions. An example of an existing platform from the company is shown in Figure 95.



Figure 95: Photograph of an existing platform from Bastian Solutions. The lift in our particular application will not need the scissor extension in the horizontal direction.

The sector manipulation tool sits on the lift as show in the cross sectional diagram in Figure 96. The lift has a section which folds out into the recess between the magnet face and the TPC end-wheel. Once the sector manipulation tool is brought into position at a particular sector location, a rail system on the extended lift allows the tool to translate toward (away from) the TPC end-wheel for insertion (removal) of sector assemblies. Straps (not shown) attached to the large eye bolts provide additional support to anchor the extended tool in position, when it cantilevers toward the end-wheel.



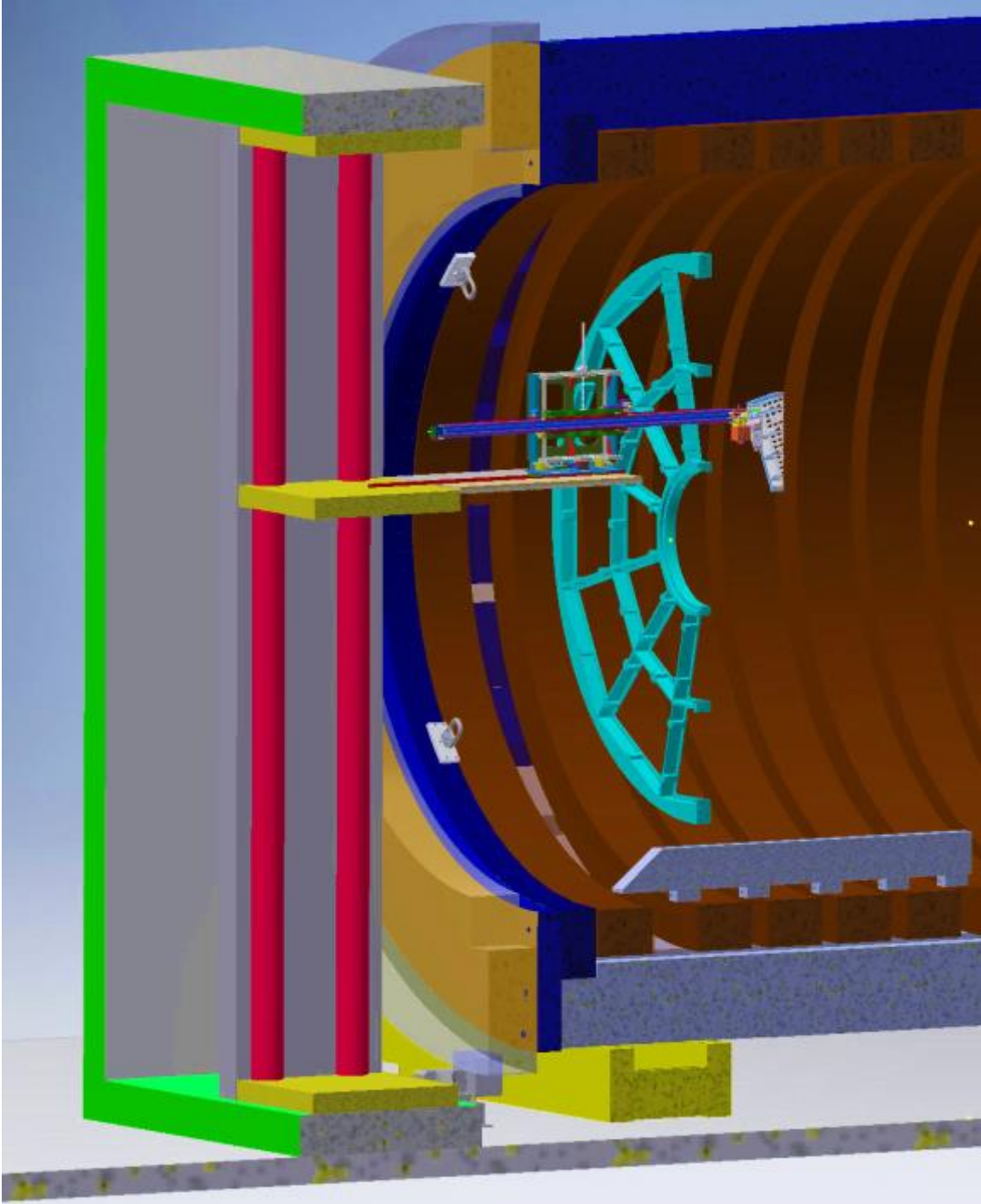


Figure 96: Cross sectional schematic view of the platform to show how the sector manipulation tool sits on the lift.

The top panel of Figure 97 focuses on the gearbox of the sector manipulation tool, while the bottom panel shows how the sector manipulation tool attaches onto the strongback of the inner TPC sector assembly. The tool shown has capability to do rotations about two axes and translation along one axis in order to install a sector on the TPC end-wheel.

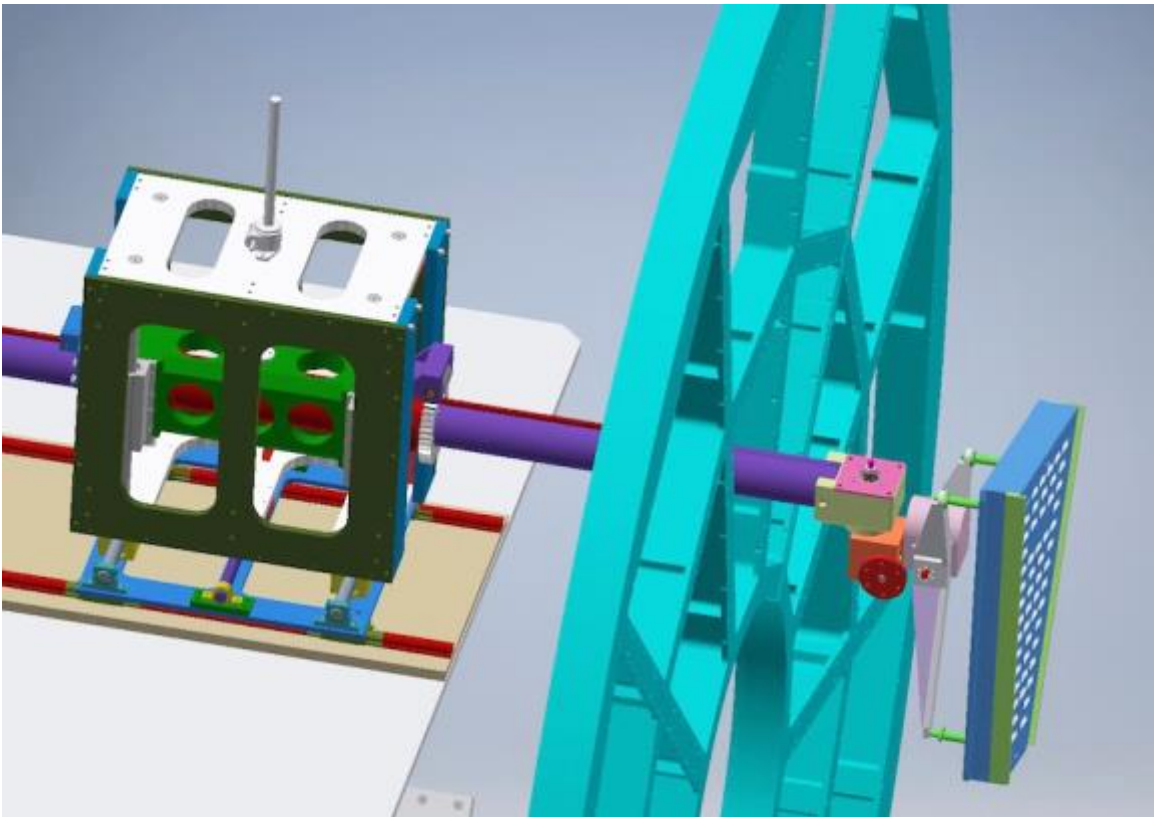
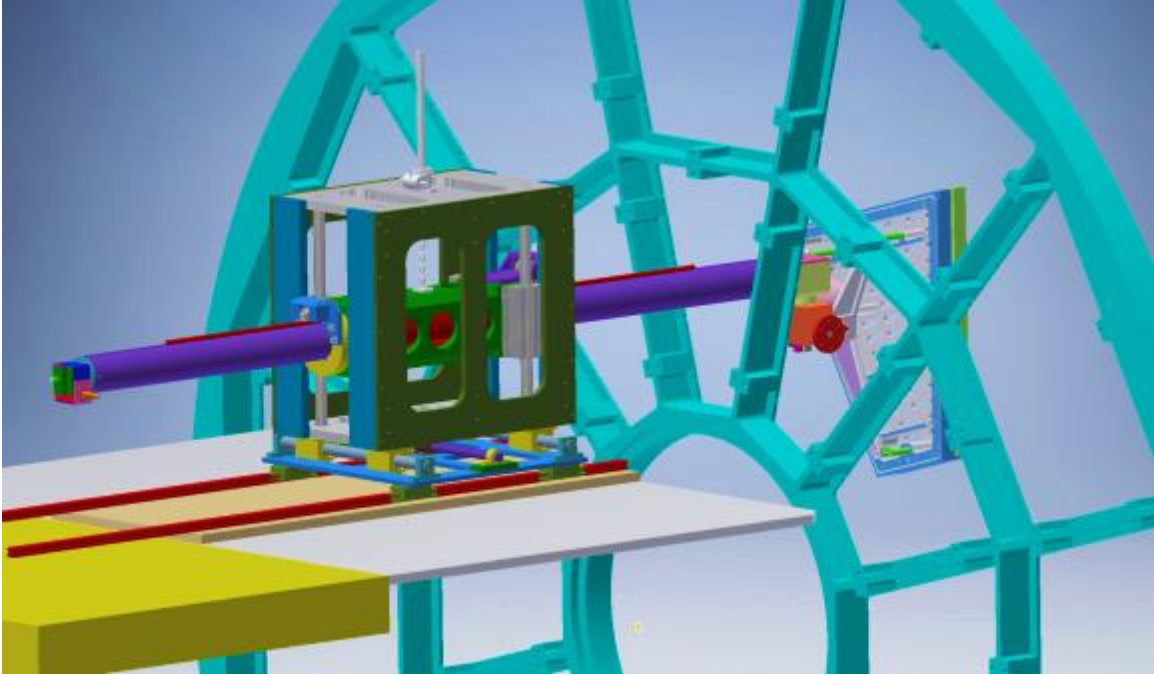


Figure 97: Schematic views of the sector manipulation tool placing an inner sector assembly through the opening at the 12 o'clock position of the TPC end-wheel.

The gearbox of the sector manipulation tool was designed at BNL using concepts borrowed from the tool for sector insertion in the ALICE TPC at the LHC. Photographs of the ALICE insertion tool taken during a visit to CERN by STAR mechanical engineer

are shown Figure 98. As shown in the photographs the ALICE TPC was also outside the magnet during sector installation, which gave the technicians full access to the TPC face using a hydraulic platform. Sector manipulation was done using the six degrees of freedom that the manipulation tool provides, and after the platform was moved in the desired location to install a particular sector.

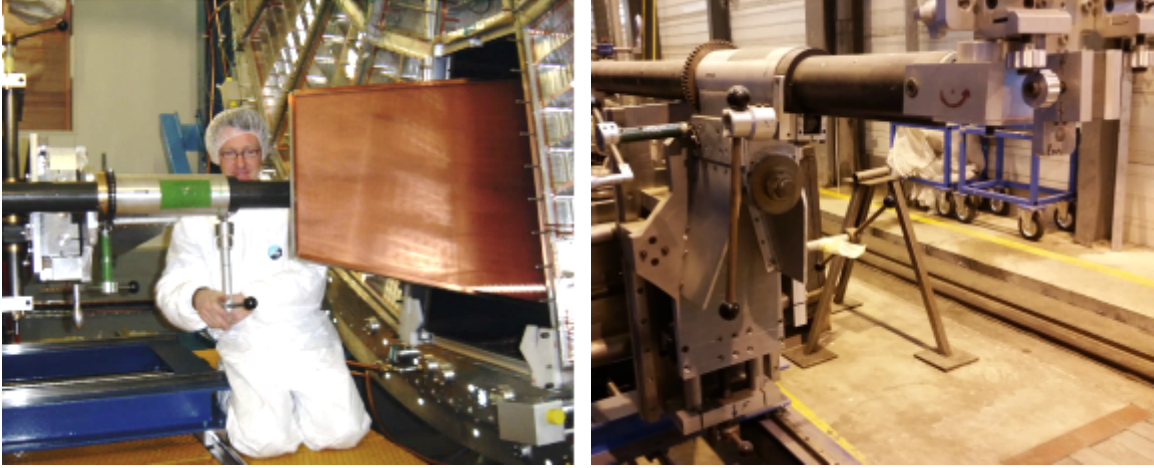


Figure 98: Photographs of the TPC sector manipulation tool used in assembly of the ALICE TPC at LHC.

In conclusion, the design of a new insertion tool for the STAR iTPC project is well advanced and is based on previous experience of the assembly scheme for TPC sector insertion at STAR and ALICE experiments. A vendor for the movable support platform has already been identified. We are planning to thoroughly test the manipulation tool prior to a sector replacement test in which the whole setup is built after the magnet containing the TPC is rolled out into the STAR assembly hall.



## **12 Participating Institutions**

Brookhaven National Laboratory  
Czech Technical University in Prague  
Kent State University  
Lawrence Berkeley National Laboratory  
Nuclear Physics Institute, Academy of Sciences  
Shandong University  
Shanghai Institute of Nuclear and Applied Physics  
University of California at Davis  
University of Texas  
University of Science and Technology of China

This page intentionally left blank

This page intentionally left blank

Back Cover